Scientific report ; WR 2008 - 02

On the upgrading of the modified Carbon Bond Mechanism IV for use in global Chemistry Transport Models

Jason E. Williams and Twan P.C. van Noije

De Bilt, 2008

KNMI scientific report = wetenschappelijk rapport; WR 2008 - 02

De Bilt, 2008

PO Box 201
3730 AE De Bilt
Wilhelminalaan 10
De Bilt
The Netherlands
http://www.knmi.nl
Telephone +31(0)30-220 69 11
Telefax +31(0)30-221 04 07

Authors: Williams, J.E.
Noije, T.P.C. van

Scientific report ; WR 2008 - 02

On the upgrading of the modified Carbon Bond Mechanism IV for use in global Chemistry Transport Models

Jason E. Williams and Twan P.C. van Noije

De Bilt, 2008

Contents

Abstract

The modified Carbon Bond Mechanism 4 (Houweling et al., 1998) has been updated to include the most recent recommendations concerning both the input parameters used for calculation of both photolysis rates (*J* values) and the chemical reaction rates (Sander et al., 2006; Atkinson et al., 2006). First we present the results of a box model study that investigates the differences between the chemistry of TM4 and TM5. An inconsistency is introduced as a result of differences in the definition of the photolysis rate of methylglyoxal ($CH_3C(O)CHO$). The most significant effects were found to occur for urban (polluted) scenarios throughout all seasons. In summary, the most important updates were: (i) a retuning of the photolysis rate for $CH_3C(O)CHO$, (ii) the 30% increase in the photo-dissociation rate of formaldehyde (HCHO), (iii) changes to the reaction rates involving organic peroxy-radicals and (iv) an enhanced formation of ORGNTR. Applying these updates resulted in a decrease in the availability of reactive nitrogen which influences the production efficiency of ozone. When incorporating an operational set of these updates into the 3D global CTM TM4 it was found that both increasing the J_{MGLY} value and introducing tracer transport for $CH_3C(O)CHO$ significantly reduced the surface concentrations over industrial regions by up to 80%.

For the other trace gases there were generally decreases in tropospheric [OH], [HO_2], [O_3], [PAN], [HNO_3] and [HCHO], with associated increases in [ORGNTR] and [CO]. In general, the oxidising capacity in the model atmosphere decreases as a result of the lower global production rate of OH. Comparisons made against selected ozonesonde profiles shows that TM4 generally over predicts surface ozone in the tropics whilst underestimating surface ozone in remote locations. For the upper troposphere TM4 generally under predicts tropospheric ozone indicating that the transport and/or release of reactive nitrogen is insufficient. For surface CO there are generally improvements in the correlation between values simulated in TM4 and a host of CMDL measurement sites. The atmospheric lifetimes of both CH4 and O3 become ~9.3 years and 23.6 days, respectively, where both these values are in the 1-σ variability of the multi-model ensemble mean given in Stevenson et al (2006) for the IPCC 2000 simulations.

1. Introduction

In order to be able to investigate the effects that increasing anthropogenic gaseous and particulate emissions have on the composition of the lower atmosphere requires the use of complex computational tools such as state-of-the-art 3D global Chemistry Transport Models (CTM's). Such CTM's are typically driven by meteorological data meaning that they account for the wide ranges in air pressure, temperature, relative humidity and radiation on the rate of chemical removal of greenhouse gases (*e.g.* CH_4). Moreover, by accounting for the subsequent dilution of chemical precursors by convection, advection and associated mixing processes, such models have the ability to be able to simulate the long-range horizontal and vertical transport of trace gas species away from their source regions, which has been found to be important for regional air quality and processes that occur in the upper troposphere.

An important requirement of such large-scale models is the ability to perform simulations with acceptable run-times for any given simulation period, which typically range from between months to decades. Therefore computational efficiency, parallelisation of the code over multiple processors and strict optimization procedures are necessary to avoid excessive load on shared computing facilities and achieve satisfactory runtimes. For this reason parameterisations are commonly used for the concise description of the processes that occur in the atmosphere. For example, rather than including an explicit description of the hundreds of chemical species which are thought to occur in the troposphere, lumped chemical mechanisms have been developed (e.g. CBM4 (Gery et al., 1989); RACM (Stockwell et al., 1997)) which have the ability to accurately capture the chemical evolution of the most abundant trace gas species found in aged air-masses. Moreover, by coupling such mechanisms to efficient chemical solvers significant savings can be made when performing expensive simulations compared with using fully explicit schemes (e.g. Liang and Jacobson, 2000).

One such CTM is the "TM" model, which has been developed for more than a decade by a consortium of European partners, in collaboration with leading Dutch research institutes including KNMI. Although the model is used for a wide range of studies, one use is for performing tropospheric chemical studies on a global scale. The most recent version of the model is TM5 (Krol et al., 2005) which has a novel zooming feature to allow regional studies to be performed using boundary conditions taken from a global domain. Both TM5, and it's immediate predecessor TM4, have been used for a host of scientific studies including IPCC comparisons (e.g. van Noije et al., 2006; Stevenson et al., 2006), retrieval of satellite products for the derivation of emission trends (e.g. van der A et al., 2006; van der A et al 2008) and comparisons with ground-based measurements (e.g. de Meij et al., 2006). For the chemical component the TM model uses the modified CBM4 chemical mechanism developed by Houweling et al. (1998), which has a reduced number of tracer species, whilst describing the most important background reactions more explicitly as compared to the original CBM4 mechanism developed by Gery et al. (1989). This was deemed necessary in order to improve the accuracy and performance of the mechanism in global CTM's, where a wide range of NO_x (a composite of NO and NO_2) and Non-Methane Hydrocarbon (NMHC) regimes can be found. In TM further parameterisations are used for the calculation of photolysis rates (Landgraf and Crutzen, 1998; Krol and van Weele, 1997), aerosols (Jeuken et al., 2001) and for dry/wet deposition (Ganzeveld et al., 1998; Roelofs and Lelieveld, 1995; Guelle et al., 1998). The resulting reaction rates, emission fluxes, deposition velocities and photo-dissociation rates (hereafter referred to as *J* values) are subsequently integrated over time by coupling the chemical system to the Eulerian backward iterative method (EBI) developed by Hertel et al. (1993). This chemical solver has been shown to be an efficient and accurate chemical solver for atmospheric applications when using the technique of operator splitting (Huang and Chang, 2001).

Although the modified CBM4 mechanism has been shown to perform well over a range of conditions in the context of a global CTM (Houweling et al., 1998) it utilises laboratory data from a wide variety of literature sources, some of which have been superseded by more recent laboratory measurements and updated with respect to their dependencies on temperature and/or pressure. This has provided the necessary motivation for further modifications to be made to the original CBM4 mechanism by various research groups in order to incorporate the latest recommendations from both the Jet Propulsion Laboratory (JPL) and the International Union of Pure and Applied Chemistry (IUPAC) data assessment panels (e.g. Sander et al., 2002; Atkinson et al., 2004). For instance, Jeffries et al. (2002) have re-evaluated the original CBM mechanism against smog chamber data to produce the CB2002 mechanism, which has since been further updated to produce the CB4xi mechanism (Yarwood et al., 2005a). Moreover, they incorporate the development made by Tanaka et al. (2003) regarding the inclusion of chlorine chemistry into the carbon bond mechanism, which was performed in order to evaluate the effect of reactive chlorine emissions on tropospheric ozone formation. The most recent version of the mechanism is CB05 (Yarwood et al., 2005b) which makes significant improvements to the mechanism as compared with smog chamber experiments. These improvements include increasing the complexity regarding isoprene degradation,

differentiating between acetaldehyde (CH_3CHO) and the higher aldehydes, introducing a new formation route for ORGNTR in polluted atmospheres and also the introduction of a lumped species to represent terpenes. Thus CB05 could act as a template for future versions of the CBM mechanism adapted for global models, as CBM4 did for the mechanism discussed here. However, the full CB05 scheme was developed for use in regional air quality models meaning that the number of species needed to describe regional NMHC chemistry is rather extensive which makes the full mechanism too large for inclusion into a CTM considering that CPU power must be partitioned between different computational tasks. Therefore, a reduction of the mechanism is necessary before it can be applied in large-scale models.

In this scientific report we investigate the differences between the performance of the chemical mechanisms currently used inTM4 and TM5, and then homogenise the reaction mechanism to remove these differences. For this purpose we identify the reaction rate parameters that have become outdated with respect to the recommendations available in the latest assessments (e.g. Sander et al., 2006), and subsequently update ~60% of the rate constants whilst maintaining the original number of tracer species and reactions included in the modified CBM4 scheme. Moreover, the online calculation of photolysis rates is included in order to investigate the influence of new product channels, absorption co-efficients (σ) and quantum yields (ϕ) on the lifetimes and evolution of important trace gas species. In order to differentiate between the various chemical effects introduced by these updates we perform box model simulations for a range of atmospheric scenarios. In Section 2 we provide details of the box model used for this assessment. In Section 3 we investigate the consequences of homogenising the photolysis of methylglyoxal ($CH_3C(O)CHO$) (hereafter referred to as J_{MGLY}) in the current versions of TM4 and TM5. We also conduct a set of sensitivity studies to examine the changes introduced by updating the σ and ϕ values used for calculating selected photolysis frequencies in order to prioritise the most important photolysis rates. In Section 4 we provide details of the cumulative effects introduced when updating the modified CBM4 mechanism and discuss the main differences between the current performance of both TM4 and TM5. In Section 5 we perform re-runs of both the IPCC and Royal Society simulations to determine the resulting changes in important tracer fields when adopting the updates to the reaction data in the operational version of TM4. Finally in section 6 we summarise our conclusions and give recommendations regarding the further development of the CBM mechanism for use in global chemistry transport models.

2. The Chemical Box Model

2.1 A Description of the 0-D Model

The 0-D box model used for this study can be viewed as a simplified version of the TM 3D-CTM, where only the chemical processing, emissions and depositions are included (i.e all transport processes are ignored). It includes a total of 39 chemical species, 67 reaction rates and 16 photolysis rates. These details are identical to those included in the TM model except for the removal of O3s, SO4_a and NO3_a, which represent a tagged tracer to determine the amount of O_3 transported downward from the stratosphere into the troposphere, sulphate aerosol and nitrate aerosol, respectively. For further details concerning the chemical species, reaction rates and photolysis rates the reader is referred to the Appendices A, B and C, respectively. For simplicity all box model simulations were performed for the gas-phase only under clear sky conditions, meaning no heterogeneous loss of species occurs on either clouds or aerosols and, therefore, no wet deposition. Simulations are performed for a period of 4 days for the lowest kilometre of the atmosphere only.

The chemical mechanism used is the modified CBM4 scheme developed by Houweling et al. (1998), where the differential equations used to describe the chemical evolution of the system are solved using the EBI chemical solver of Hertel et al. (1993) using a time-step of 15 minutes. Photolysis rates are calculated online for each time-step using a reduced version of the online scheme outlined in Williams et al. (2006), where the actinic fluxes ($F_{act.}$) are calculated explicitly. The parameterisation currently used in the TM model (Landgraf and Crutzen, 1998) was not implemented into the box model, as this would require the production of a new set of look-up tables for the inclusion of the updated photolysis data. This step was considered to be unfeasible considering the additional work involved. The solar zenith angle (SZA) is calculated using the latitudinal position of the box, along with the time of year and time of day, for a longitude of 0°. For SZA > 85°, photolysis of chemical species for the lower few kilometres of the atmosphere is assumed to be unimportant. Moreover, calculations are performed using only 7 of the 8 available bands, where photons for λ<202nm are screened out by the overhead O_2 column above the tropopause. The SZA limit which is imposed on the calculation of photolysis rates means that the pseudo-spherical correction and highest SZA band settings (Grid B in Williams et al., 2006) are also not applied for these simulations. The atmospheric column extends up to 120km, segregated into 49 distinct atmospheric layers, where the overhead pressure, temperature and ozone density is taken from the widely used AFGL atmospheres (Anderson et al., 1986) on the vertical grid provided. The information for all layers is used to calculate the differential slant columns for both O_2 and O_3, which are subsequently needed to calculate the optical depth of the overhead column for the 7 scaling wavelengths. Scattering and absorption by atmospheric aerosol is included according to Shettle and Fenn (1979), where details of the prescribed aerosol types for each scenario are given in Section 2.2. In order to attain similar photolysis frequencies as those calculated in the TM model the recommendations from Demore et al. (1997) have been used, where the exceptions are outlined in Appendix C (M. Krol, personal communication, 2007). It should be noted that some of these recommendations remained valid up until 2000-2002, as shown in Appendix B. A total of 22 deposition rates are included in the model. This is similar to the TM model with the exceptions of $CH_3C(O)O_2$ and $CH_3C(O)CHO$. The values adopted for these deposition fluxes are given in Appendix D. Moreover, the resistance parameterization of Ganzeveld et al. (1998) is replaced by a simple first-order loss rate (i.e.) the land surface has no impact on the deposition rates, and the emission fluxes are fixed throughout the year with no seasonal dependency.

2.2 Scenarios, Emissions and Model Atmospheres

During the development of the modified CBM4 mechanism the scheme was tested over a range of NMHC/NO_x ratios and selected species compared against those simulated using the more extensive RACM mechanism of Stockwell et al. (1997). Subsequent comparisons of the resulting global tracer fields have been made with a host of measurements and have shown that the scheme performs relatively well when used in the context of a 3D CTM (Houewling et al, 1998). Here we do not perform further comparisons against RACM as there are no additional species or reactions being added to the mechanism for the updates being discussed here. Therefore it is assumed that the performance of the modified CBM4 mechanism using updated rate co-efficients remains relatively robust in low NO_x environments. Moreover, a number of the rate co-efficients have already been updated in the working version of the TM model (see Appendix B), and the gas-phase chemistry of both SO_2 and NH_3 has also been added. It should also be noted that even the original CBM4 mechanism of Gery et al. (1989), which includes many more reactions and organic species, has difficulty in simulating HO_x precursors such as [HCHO] and [H_2O_2] as compared to smog chamber data (Liang and Jacobson, 2000) and,

therefore, should not be viewed as the 'ideal' mechanism even for the highly polluted scenarios it was originally designed to simulate.

AFGL atms.[1]	Marine	Rural	Urban	Tropical	Temp (°K)
High-lat Winter	MAA	-	-	-	257
Mid-lat Summer	MAS	RLS	URS	-	294
Mid-lat Winter	MAW	RLW	URW	-	272
Tropical	MAT	-	-	TR	299

Table 1: Definitions for the acronyms used to identify the combination of AFGL atmospheres and modelling scenarios. [1] All atmospheres are taken from Anderson et al. (1986). The pressure adopted is 1013hPa apart from the mid-lat winter case where the pressure is 1018hPa.

In order to test the effects of the proposed updates we define four different atmospheric scenarios, namely 'marine', 'rural', 'urban' and 'tropical'. Each scenario has a unique set of emission fluxes and initial conditions, which are aimed at providing a wide range of NO_x and NMHC ratios. Detailed information regarding the individual scenarios is given in Appendices D and E, respectively. For the lumped organic species (e.g. OLE) and the sulphur compounds (e.g. DMS, MSA) initial conditions are taken directly from the IPCC version of the TM5 model (available on the CVS server hosted at KNMI). Four regions are defined for this purpose, one for each scenario: Marine (Lat: 60°S → 5°S, Lon: 180°W → 120°W), Rural (Lat: 40°N → 60°N, Lon: 90°E → 132°E), Urban (Lat: 36°N → 52°N, Lon: 6°W → 18°E) and Tropical (Lat: 8°S → 8°N, Lon: 12°E → 18°E). The land/sea mask used in TM is applied during the averaging to ensure that the Marine values are selected from grid cells containing no appreciable land masses and the Rural/Urban/Tropical values selected from grid cells which are not influenced by coastal regions.

In order to vary both the temperature and pressure of the system, values are taken from both the winter and summer mid-latitude AFGL atmospheres (Anderson et al., 1986) except for the tropical scenario, where the tropical AFGL atmosphere is adopted. The winter high latitude AFGL atmosphere is also used in conjunction with the marine scenario to investigate very cold conditions near the poles. The acronyms used to distinguish the combination of AFGL atmospheres and scenarios throughout this report are provided in Table 1, along with the respective air temperature. Moreover, the atmospheric parameters used for the calculation of the photolysis rates in each of the different scenarios are given in Table 2.

Scenario	Latitude of box	Ground albedo	Aerosol type[3]	Date
MAA	75°S	0.09 – 0.03 [1]	Marine	15th Sept
MAW/MAS	25°S	0.09 – 0.03 [1]	Marine	1st Jan/21st June
RLW/RLS	50°N	0.07 – 0.184 [1]	Rural	1st Jan/21st June
URW/URS	44°N	0.1 [2]	Urban	1st Jan/21st June
MAT	0°N	0.09 – 0.03 [1]	Marine	21st June
TR	0°N	0.08 – 0.25 [1]	Rural	21st June

Table 2: The details of the input parameters chosen for the calculation of photolysis rates for the various scenarios as defined in Table 1. Additional information: [1] interpolated values from Koelemeijer et al. (2003), [2] estimated average, [3] optical properties and number densities are taken from Shettle and Fenn (1979) with scaling of 0.3835 (which gives an AOD=0.32 at 550nm).

3. The Effect of Updating Tropospheric Photolysis Rates on Atmospheric Composition

3.1 The Explicit Calculation of the Photolysis of $CH_3C(O)CHO$

In Houweling et al. (1998) the photolysis of methylgloxal (hereafter denoted as J_{MGLY}) is calculated as in the original CBM4 mechanism of Gery et al. (1989), who made an estimate for this photo-dissociation rate using smog chamber data (i.e.) not from a precision laboratory measurement. This was derived at a time when laboratory measurements of σ and ϕ values for exotic organic species were scarce; therefore in order to gain an approximate value for J_{MGLY} assumptions were usually made using compounds containing similar functional groups. Since then a wealth of data has become available in the literature allowing the explicit calculation of photolysis frequencies for the higher organics. In the current version of the TM model J_{MGLY} is scaled to J_{bCH2O} using a scaling factor of either unity (TM4) or 50.0 (TM5) (see Appendix C). In both instances the photolysis parameters for HCHO originate from DeMore et al. (1997) as used in Stockwell et al. (1997). This means that there is an inconsistency between the most commonly used versions of the TM model. Moreover, it also shows that an update to the modified CBM4 mechanism has already been made concerning J_{MGLY} as compared to the value given in Houweling et al. (1998). In order to address this inconsistency we show comparisons between the results obtained for TM4, TM5 and the changes introduced as a result of upgrading the input parameters.

Although $CH_3C(O)CHO$ is commonly associated with the oxidation of isoprene, the modified CBM4 mechanism also uses it as a surrogate for complex aromatic species such as xylene in order to account for the missing reactions in the modified CBM4 mechanism (Houweling et al., 1998). The other chemical surrogate used is PAR, which is defined as being photochemically inert. Therefore, the maximum concentrations of both $CH_3C(O)CHO$ and PAR are often found in regions influenced by strong anthropogenic emission sources (see Section 5.1). For this reason we choose the URW scenario to discuss the effects of this update, where the surface pressure is somewhat higher than during summer (see table 1) which also influences the value of $\phi_{CH_3C(O)CHO}$.

The $\phi_{CH_3C(O)CHO}$ recommendations have recently been updated (Sander et al., 2006), which lead to differences of ±5% in the absolute values compared to the previous set of recommendations (Sander et al., 2002). Moreover, the value of $\phi_{CH_3C(O)CHO}$ is equal to unity over the spectral range λ = 320-380nm, but exhibits a pressure dependency for λ > 380nm (Koch and Moortgat, 1988). Although the recent recommendations adopt $\phi_{CH_3C(O)CHO}$ values from Koch and Moortgat (1988) over the spectral range λ = 250-420nm, those for λ > 420nm are now replaced by the values derived by Chen and Zhu (2000), resulting in $\phi_{CH_3C(O)CHO}$ which is four times higher in this spectral region.

Figure 1a shows a comparison of the resulting J_{MGLY} values for the URW scenario as calculated using the scaling ratios adopted in both TM4 and TM5, the data recommended in Atkinson et al. (1997) and the data recommended in Sander et al. (2006). The motivation for showing calculations which use old recommendations is to highlight the fact that the current scaling ratios applied in the different versions of the TM model are not tuned to values which were available at the time of the last upgrade. It can be clearly seen that there is an increase (decrease) of ~80-90% in the magnitude of J_{MGLY} at the zenith for TM4 (TM5) when calculating the value explicitly using the recommendations. Moreover, the J_{MGLY} calculated using the Atkinson et al. (1997) recommendations is also quite different from the J_{MGLY} in the current versions of both TM4 and TM5. The corresponding difference in the resident [$CH_3C(O)CHO$] is shown in Figure 1b. The resulting daytime concentrations decrease (increase) by ~50% (~1000%) for TM4 (TM5). This shows that the value of J_{MGLY} applied in TM is either too low or too high depending on the version of the model.

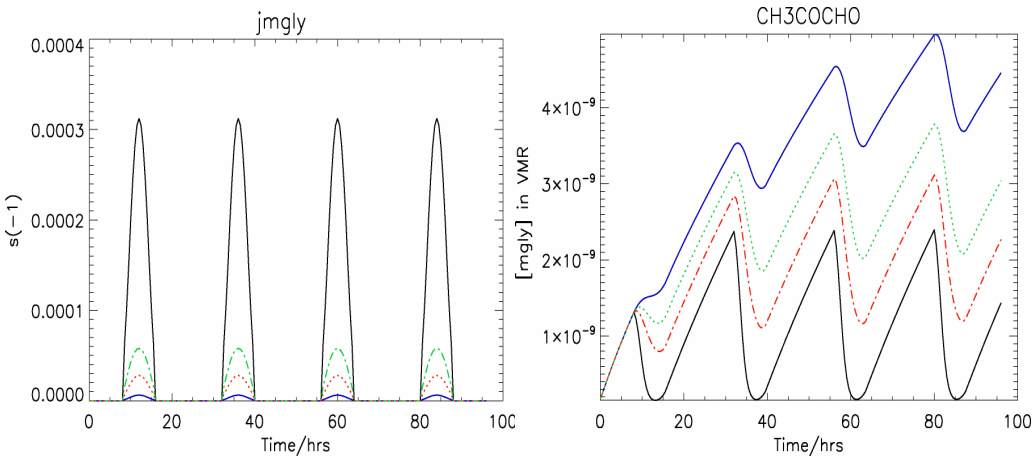

Figure 1: Comparisons of (a) J_{MGLY} and (b) [$CH_3C(O)CHO$] for the scenario URW using the scaling assumption for J_{MGLY} adopted in TM4 (—) and TM5 (—) versus the explicit J_{MGLY} calculated using recommendations made in 1997 (red) and 2006 (green).

In the modified CBM4 mechanism the photolysis of $CH_3C(O)CHO$ acts as an important source of both HO_2 and the acetyl peroxy radical ($CH_3C(O)O_2$) when applied to urban scenarios *vis* reaction (1):

$$CH_3C(O)CHO + h\nu \rightarrow CH_3C(O)O_2 + HO_2 + CO \qquad (1)$$

Figure 2 shows the effect of applying an explicit calculation for J_{MGLY} on (a) HO_2, (b) $CH_3C(O)O_2$, (c) NO_x and (d) O_3. It can be seen that for both [HO_2] and [$CH_3C(O)O_2$] there are significant differences in the maximal daytime concentrations between TM4 and TM5 as a result of the application of a different scaling ratio. Neither model is able to capture the correct production rate for these radicals compared with those when J_{MGLY} is calculated explicitly. This also has repercussions for HO_x reservoirs such as H_2O_2 and CH_3OOH (not shown).

The significant differences shown for these important free-radical species affects the entire radical budget by the fast reactions KMO2HO2, KHO2NO, KMO2NO and KC46 (see Appendix B). Moreover, the efficiency of [PAN] formation is governed by the availability of both $CH_3C(O)O_2$ and NO_2 (via KC47) meaning that amount of reactive nitrogen held in such reservoir species differs markedly between TM4 and TM5 (see Section 3.5). This also has implications for other important nitrogen reservoirs such as HNO_3 (not shown). For TM4 chemical production of ozone is hindered by the additional [NO] in the system, which titrates O_3 via reaction KNOO3. For both TM4 and TM5 the lower [NO_2] hinders [O_3] formation with respect to simulation time as compared with the explicit calculation. Here we limit further analysis to Section 3.6, where all of the important updates made to the photolysis parameters are implemented simultaneously, as this particular effect is moderated under such circumstances.

In order to address this under estimation (over estimation) of J_{MGLY} in TM4 (TM5) we use the box-model to re-tune the scaling ratio which should be applied to improve the agreement between the scaled J_{MGLY} value and that calculated explicitly using the updated photolysis parameters for $CH_3C(O)CHO$ taken from the new recommendations (Sander et al., 2006). For this purpose we place more emphasis on the diurnal variation of J_{MGLY} during the summertime, where the *J* values are greatest. This procedure indicates that the scaling ratio used for J_{bCH2O} should be increased from unity to 5.5 in TM4 (and reduced from 50 to 5.5 in TM5). Figures 3a and b show the resulting agreement between this scaled J_{MGLY} and that calculated explicitly by the online photolysis code for scenarios RLW and RLS, respectively. It can be seen that although the agreement is good for summertime scenarios, there is an under-estimation in the scaled J_{MGLY} value during wintertime resulting in *J* values which are ~50% smaller than those calculated explicitly. This is due a re-distribution of the band contributions to the final *J* value for scenarios that have higher SZA (meaning longer slant columns and thus more O_3 absorption). This shows that, although the application of this new scaling ratio improves on that used in the current TM model, it is still beneficial to implement the explicit calculation in the TM model when feasible.

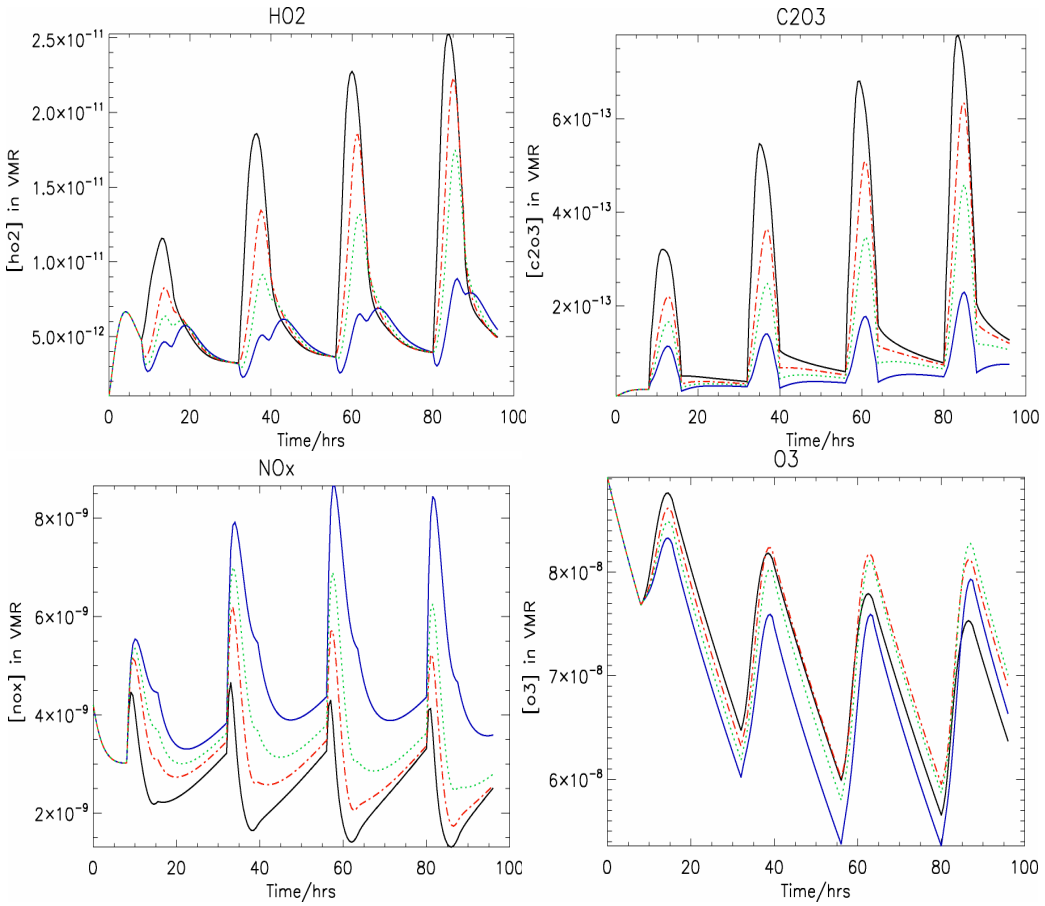

Figure 2: Comparisons of (a) HO_2, (b) $CH_3C(O)O_2$, (c) NO_x and (d) O_3 for the scenario URW. For the definition of the various runs the reader is referred to the figure legend provided for Fig. 1.

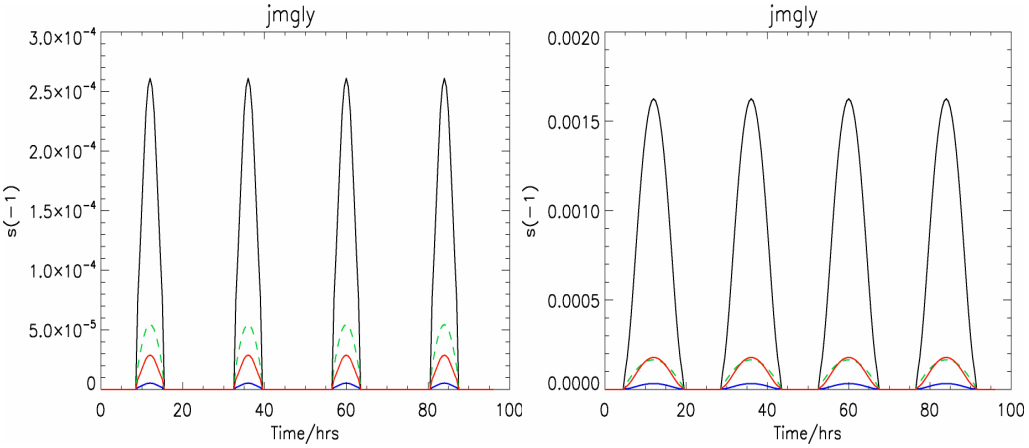

Figure 3: Comparisons of J_{MGLY} for the scenario (a) RLW and (b) RLS using the scaling ratios adopted by both TM4 (—) and TM5 (—) for J_{MGLY} versus that calculated explicitly using the latest recommendations (- - -) and that calculated when adopting a scaling ratio = 5.5 (—).

3.2 The Quantum Yield of $O_3 + h\nu \rightarrow O^1D$

During the photolysis of O_3, the partitioning between $O(^1D)$ and $O(^3P)$ production is governed by the quantum yield (ϕ) of each reaction channel adopted in the chemical reaction scheme. In the current version of the TM model the quantum yield originates from derivations made using measurements of $O(^1D)$ taken at Mauna Lao Observatory (Shetter et al., 1996). The resulting ϕ_{O^1D} is temperature dependent between λ = 307-321 nm. There are also temperature independent values between λ = 280-306nm, which vary between 0.895 - 0.95 and diminish to zero between 321-350nm. Since the publication of these values a critical analysis of all available laboratory measurements has been made by Matsumi et al. (2002) which has resulted in the recommendation of an updated temperature dependency between λ = 306-328nm (the most important spectral region for tropospheric O_3 photo-dissociation). For λ = 290-305nm a value of ϕ_{O^1D} = 0.9 is recommended. Moreover, an extended tail exists in that ϕ_{O^1D} = 0.08 is recommended between 329-340nm, although the associated values of σ_{O_3} mean that the contribution to the final J_{O3d} is rather small from this spectral region.

Figures 4a-h show the resulting profiles for O_3 and OH for both TM4 and TM5, along with the effect of updating J_{O3d} for scenarios URW, URS, RLS and TR, respectively. With the exception of the urban scenario the evolution of O_3 is nearly identical between TM4 and TM5 runs due to the low [$CH_3C(O)CHO$] which is present. For the urban scenario differences are introduced as a result of differences in the availability of reactive nitrogen (see Figure 2) which subsequently introduces differences in [O_3] ([OH]) via J_{NO2} (J_{O3d}). This causes [OH] to be higher in TM5 than TM4 for polluted cases. As would be expected, the overall effect of updating the ϕ_{O^1D} values is governed by the magnitude of J_{O3d}, thus the effects are maximal during summertime when there are longer days. This is in spite of the differences in J_{O3d} introduced by updating ϕ_{O^1D} being larger for the wintertime scenarios (not shown) (i.e.) the ϕ_{O^1D} decreases with temperature. Generally it can be seen that the loss of O_3 via photolysis decreases for all summertime scenarios with the effect being nearly identical for TM4 and TM5. This is accompanied by a small decrease in [OH] which, for the wintertime urban scenario, ranges between 10-40% depending on the day of simulation. This maybe explained by considering the decrease in ϕ_{O^1D} as a result of the new recommendations especially at low temperatures. Further analysis is conducted in Section 4 where all updates are introduced simultaneously.

3.3 The Update of the Photolysis Rate of HCHO

The photolysis of HCHO proceeds via two separate channels, as described below in reactions (2) and (3):

$$HCHO + h\nu \rightarrow CO + H_2 \quad (2)$$

$$HCHO + h\nu\,(+ O_2) \rightarrow HO_2 + HCO \quad (3)$$

The branching ratio between both reactions is determined by the respective values of ϕ_2 and ϕ_3. The intermediate HCO formed in reaction (3) decomposes almost instantaneously in the presence of oxygen to form HO_2 and CO. Significant extensions to the λ range over which the recommended values of σ_{HCHO} and ϕ_{HCHO} apply result in an increase in the contributions to both *J* values for this spectral region, where the effect of the σ_{HCHO} values dominates. Moreover, due to the formulation of the modified CBM4 mechanism any resulting change in the photolysis frequency of reaction (3) also affects the photolysis of $CH_3C(O)CHO$ due to a scaling procedure that is used (see Section 3.1).

Figure 5 shows the resulting differences for both J_{aCH2O} and J_{bCH2O} calculated using the old and new recommendations for scenarios URW and URS. Comparing these figures shows that there is an increase in both J values of ~30% independent of the season. This also has implications for J_{MGLY} due to the scaling approach described in section 3.1 (i.e.) the differences between J_{MGLY} in TM4 and TM5 become larger (not shown). In order to investigate the resulting differences of this effect between wintertime and summertime we show results for both URW and URS.

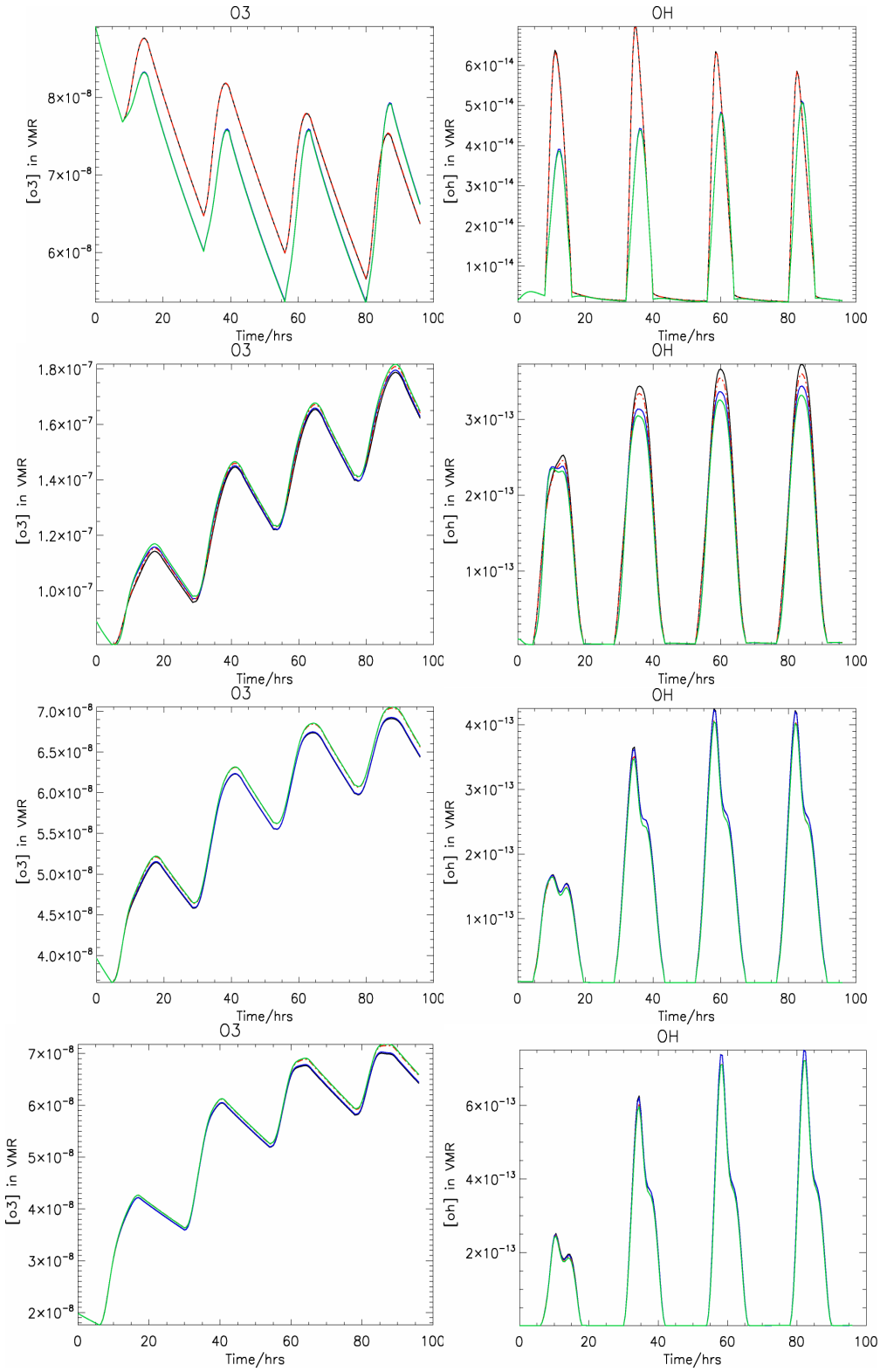

Figure 4: The effect of using updated ϕ_{O^1D} values on tropospheric [O_3] and [OH] for scenarios (from top to bottom) (a) URW, (b) URS, (c) RLS and (d) TR. Profiles are shown for simulations using the ϕ_{O^1D} values taken from Shetter et al., (1996) (— TM4, — TM5) against simulations using those of Matsumi et al., (2002) (— TM4, --- TM5).

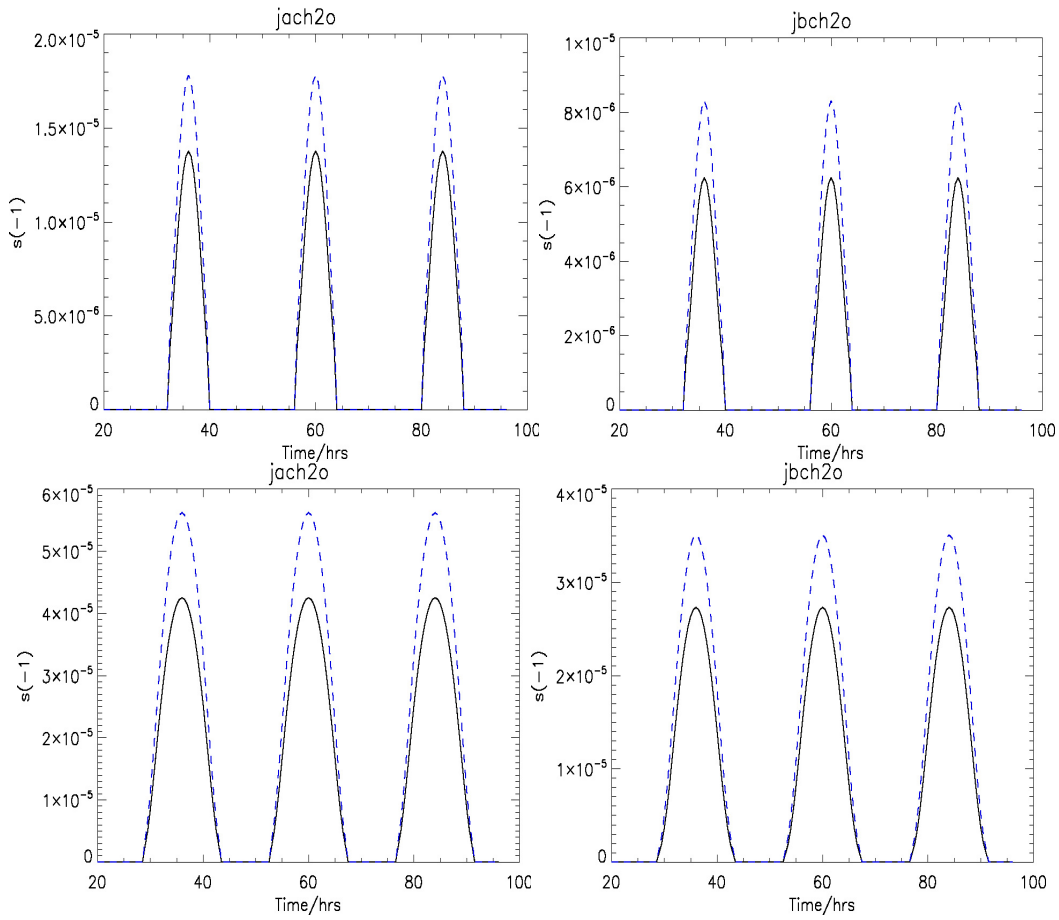

Figure 5: Comparisons of J_{aCH2O} and J_{bCH2O} for scenarios URW (top) and URS (bottom) as calculated using both old (—) and new (---) recommendations for the parameters σ_{HCHO} and ϕ_{HCHO}. The input data originates from Sander et al. (2002) and Sander et al. (2006) for the old and new simulations, respectively.

In general the differences in [HCHO] between TM4 and TM5 are largest for the URW scenario which is related to the efficiency of KFRMOH (i.e. differences in [OH], see Figure 4). Moreover, the substantial differences in [HO_2] cause related differences in both [H_2O_2] and [CH_3OOH], which both act as sources of OH via J_{H2O2} and J_{MEPE}, respectively. The heterogeneous loss of HO_2 on wet aerosol surfaces may also amplify this effect in any that CTM contains heterogeneous loss processes (although it should be noted that neither TM4 nor TM5 currently account for this effect). Therefore, we also perform additional simulations where we introduce a first-order loss rate for HO_2 of 2.7 x 10^{-3} s^{-1} into the box model in order to mimic this irreversible uptake of HO_2. This leads to a reduction in [HO_2] of ~15%. This decrease is in the range needed to reconcile explicit box model calculations with *in-situ* measurements of HO_x radicals taken at a coastal site (Sommariva et al., 2006), although uptake is highly dependent on both aerosol composition and pH.

Figure 6 shows comparisons for [HCHO], [HO_2], [H_2O_2] and [CH_3OOH] for simulations both with and without the additional loss of HO_2 on aerosols for both TM4 and TM5. The main effect of applying the updated *J* values is a ~15% reduction in the resident [HCHO], as would be expected due to the increased removal by photolysis, where the magnitude of the change in [HCHO] between TM4 and TM5 is almost identical. This has repercussions for both in-situ CO production (see section 3.5) and HO_2. The integrated effect of this perturbation in the HO_x budget over the simulation period can be assessed by comparing the Δ[H_2O_2] and Δ[CH_3OOH] between the cases shown in Figures 6e-h, where the effect on H_2O_2 is greater due to the second-order dependency of H_2O_2 formation on [HO_2] (see Appendix B). For the wintertime scenario the changes in [ROOH] are similar to those shown for [CH_3OOH], again due to the perturbation in [HO_2]. It should be noted that both HCHO and H_2O_2 are soluble in water and therefore subject to wet deposition

meaning that the effects in a CTM maybe moderated (see Section 5). For O_3, HNO_3, PAN, the other higher organics and SO_2/SO_4 this particular update has minimal effect.

For other scenarios similar changes are observed, although the differences are only a few percent for *e.g.* RLS and MAS. For scenario MAA (*i.e.* pristine locations) HCHO acts as an important precursor for HO_x radicals. Even though the magnitude of both J_{aCH2O} and J_{bCH2O} is smaller for MAA compared with Figure 5, a reduction in [HCHO] by nearly 10% occurs at the end of the simulation period (not shown). This is due to the relatively cold temperatures (259°K) enhancing the differences in the resulting *J* values. This subsequently increases both [OH] and [HO_2] during the day which has implications for the lifetime of CH_4. A further notable effect is an increase in [O_3] by ~2% by the end of the simulation period.

3.4 Other Miscellaneous Updates

This section summarises the effects introduced by applying the other updates which are given in the latest recommendations. These updates are: (a) the use of a new parameterization for the calculation of the temperature dependent values for $\sigma_{N_2O_5}$, (b) the use of explicit σ values for the calculation of J_{ALD2}, (c) the introduction of another product channel for the photo-dissociation of HNO_4, (d) the removal of the scaling factor for J_{ORGN} and (e) the application of high angle band settings in the parameterization of Landgraf and Crutzen (1998).

(a) The update concerning the temperature dependent values of $\sigma_{N_2O_5}$ has no effect on tropospheric chemistry due the new recommendations being concerned with $\sigma_{N_2O_5}$ for $\lambda < 250$nm. For the upper troposphere small differences maybe introduced depending on the geo-location therefore an update should be performed when feasible.

(b) In the modified CBM4 scheme ALD2 is a lumped species representing CH_3CHO and the higher aldehydes. The current TM chemistry uses σ_{CH_3CHO} values for the calculation of J_{ALD2} (M. Krol, personal communication, 2007), which were adopted from the TUV model (Madronich, 1992) during the last update of the photolysis scheme. In order to investigate whether J_{ALD2} is representative of a lumped species representing higher aldehydes, an average was taken between the σ_{CH_3CHO} and $\sigma_{C_2H_5CHO}$ values that are available in the latest recommendations (Sander et al., 2006). The result is an increase in J_{ALD2} by ~10% during the summer as compared to the original in both TM4 and TM5. However, this only has a marginal effect on the resident [ALD2] across the entire range of scenarios due to the photolysis rates being of the order of 10^{-5} s^{-1}.

(c) In the modified CBM4 mechanism the photo-dissociation of HNO_4 proceeds via reaction (4):

$$HNO_4 + h\nu \rightarrow HO_2 + NO_2 \quad (4)$$

In the latest JPL recommendations (Sander et al., 2006) an additional dissociation pathway is introduced, reaction (5):

$$HNO_4 + h\nu \rightarrow OH + NO_3 \quad (5)$$

Where ϕ for this second channel is 0.2 across the entire spectral region. Moreover, the tail of the absorption spectrum for HNO_4 has been extended out towards $\lambda = 350$nm compared to previous recommendations (Sander et al., 2002), although the values remain temperature independent. Due to the low [HNO_4] (in the order of 10pptv), the influence of introducing this second photolysis channel is negligible across the range of scenarios defined for this study. Moreover, the rapid photolysis of NO_3 and the high reactivity of OH mean that the transformation of the products from reaction (5) is almost instantaneous in the troposphere during the day.

(d) In the modified CBM4 mechanism the species ORGNTR represents lumped alkyl nitrates. The photolysis rate was originally calculated using absorption characteristics for a C_4 mono-nitrate as described in Houweling et al. (1998). However, the TM model uses values for methyl nitrate (CH_3ONO_2) without the inclusion of the temperature dependency for $\sigma_{CH3ONO2}$.

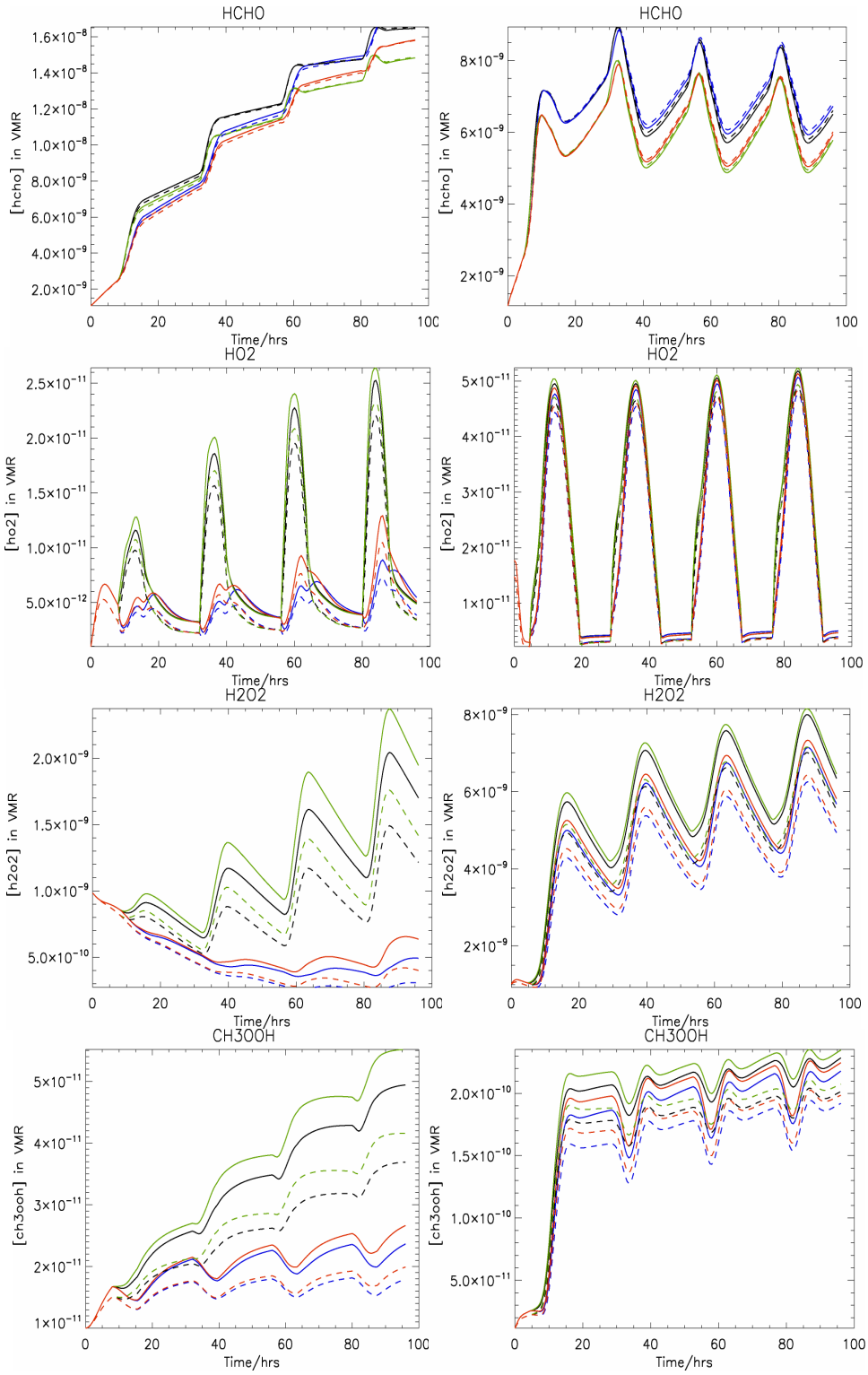

Figure 6: Comparisons of (a) HCHO, (b) HO_2, (c) H_2O_2 and (d) CH_3OOH for scenario URS calculated using both the old (— TM5, — TM4; no additional HO_2 loss: - - - TM5, - - - TM4 with additional HO_2 loss) and new (— TM5, — TM4; no additional HO_2 loss: - - - TM5, - - - TM4; with additional HO_2 loss) recommendations for σ_{HCHO} and ϕ_{HCHO}. The input data originates from Sander et al., (2002) and Sander et al. (2006), respectively.

Moreover, this rate is scaled up by a factor of 2.5 when applied in the current TM model in order to reduce the atmospheric lifetime of ORGNTR. To be consistent with the measured absorption data, this amplification is only warranted if the C_2 and C_3 alkyl nitrates have larger σ values than CH_3ONO_2. Analysis of the data indicates that the absorption tail past 300nm is in fact more truncated for these alkyl nitrates resulting in lower tropospheric *J* values (Roberts and Fayer, 1989). Considering that the absorption spectrum for CH_3ONO_2 has been used for the calculation of J_{ORGN}, the use of a further scaling factor of 2.5 cannot be justified. In the modified CBM4 scheme ORGNTR is predominantly formed via the oxidation of isoprene (via the operator species XO2N, see Appendix B), which means that in the TM model the majority of the formation occurs around the tropics. For the sensitivity test performed here we simply remove the scaling factor of 2.5, therefore using a temperature independent upper limit for all alkyl nitrates. This results in increases in [ORGNTR] by between 10-20% depending on the chosen scenario. In a CTM this will increase the amount of NO_2 transported away from source regions as a result of the increase in the atmospheric lifetime (see Section 5).

(e) In Williams et al. (2006) the errors associated with the photolysis rates calculated using the band approach for high SZA (θ>71°) have been shown to be significant in the lower atmosphere for important species such as HCHO and HNO_3 when using the original band settings, as defined in Landgraf and Crutzen (1998). Therefore, we test the effect of using the high-angle band settings and the application of limits to the resulting scaling ratios (Grid A in Williams et al., 2006) on the resulting *J* values. Figure 7 shows the resulting diurnal variation of both (a) J_{O3d} and (b) J_{NO2} for both the original and high-angle band settings for scenario MAA (where θ_{max}=77° for the chosen simulation period).

Differences in *J* values between the two band settings predominantly occur for those *J* values which are sensitive to the screening of incident photons in the UV spectral region by the overhead ozone column. For any given species the sensitivity to this effect is governed by their characteristic σ values. These differences are due to the application of unrealistic scaling ratios in the UV region when adopting the original band settings, resulting in enhanced band contributions to the final *J* values (see the detailed explanation provided in Williams et al., 2006). For instance, this artificial amplification results in J_{O3d} being nearly as large for θ > 80° as at the zenith for scenario MAA (the 'spikes' which are imposed on the diurnal variation as shown in Fig.7a). These 'spikes' subsequently disappear when applying the high-angle band settings. The integrated effect over a day for this scenario is that ~20% less O(^{1}D) production is formed via J_{O3d}. For J_{NO2} there is a marginal increase of ~5% at the zenith. Moreover, this has potential to alter the HO_x budget by increasing [HCHO] (not shown). Therefore this update has the potential to affect chemistry in the remote regions (e.g.) for mid-September the λ_{max} varies between 80°-70° over the latitudinal band 78-68°S, although the region where this occurs changes throughout the year.

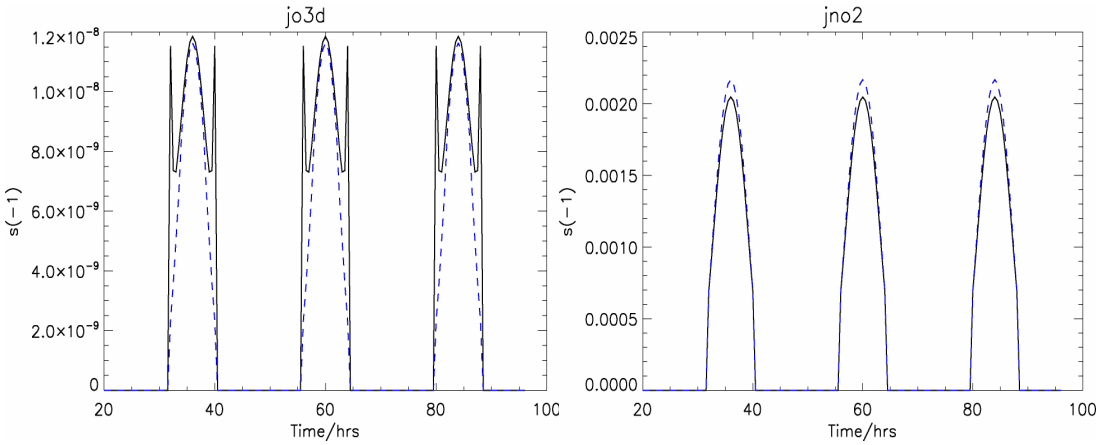

Figure 7: The diurnal variation of (a) J_{O3d} and (b) J_{NO2} for scenario MAA simulated. Comparisons are shown for both the original (—) and high angle band settings (---).

For other winter scenarios (namely MAW, RLW and URW), the instances where the SZA falls between the SZA limits needed for the application of the high angle grid is < 10% over a typical day, resulting in small differences of a few percent for most trace gas species. This update is included in the full_run described in section 3.5

3.5 The Cumulative Effect of Introducing Simultaneous Updates for Photolysis Rates

Finally, the individual updates discussed in the previous sections are implemented simultaneously to determine whether the simulated differences are moderated in any way when accounting for the cumulative effects of all the proposed updates to the photolysis rates. Here we differentiate between the updates that can be made to the TM model without the introduction of an online photolysis routine (or the 'operational settings') and the complete set of updates as introduced in the preceding sections. In the following analysis we refer to these as the op_run and the full_run, respectively. For the op_run we simply update the J_{MGLY} and J_{ORGN} values by modifying the scaling ratios applied.

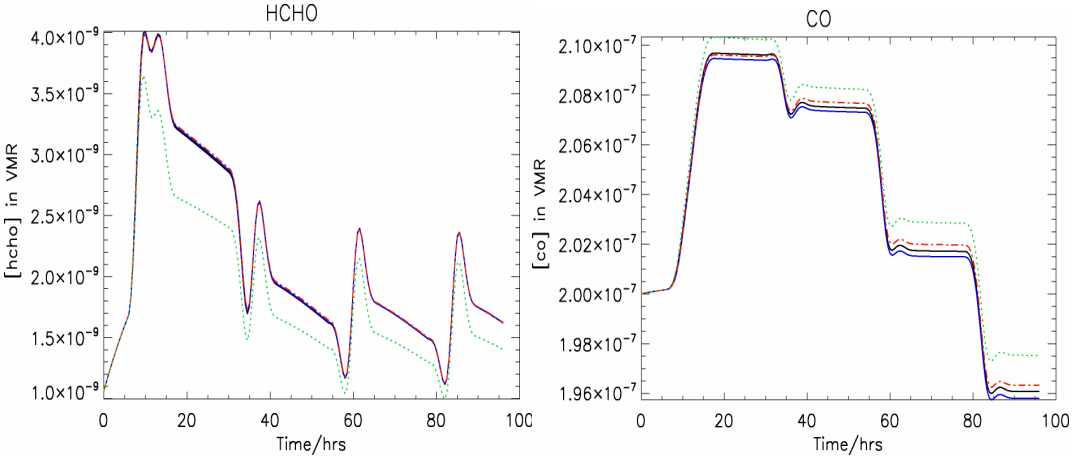

Figure 8: Comparisons of (a) HCHO and (b) CO showing increases in the *in-situ* production of tropospheric [CO] as a consequence of increased HCHO photolysis for the scenario TR. Changes are shown for TM4 (—) and TM5 (—) against those using the op_run (---) and the full_run (---).

For the full_run all updates are included except those associated with N_2O_5 and HNO_4, for which the individual effects were found to be negligible (see Section 3.4). Analysing the resulting changes in the evolution of trace gas species reveals that for some long-lived species similar differences occur across a range of scenarios. These differences are summarised below.

For the full_run there are reductions in [HCHO] of between ~5-10% across all of the scenarios due to increases in both J_{aCH2O} and J_{bCH2O} in line with the findings of section 3.3. For scenarios not influenced by strong CO emissions (e.g. MAS) this results in noticeable increases in [CO] of between ~2-3% as a result of the enhanced *in-situ* production. This is not captured by the op_run due to the use of the old HCHO recommendation although for these conditions both TM4 and TM5 show identical behaviour. Figures 8a and b show examples of such differences in [HCHO] and [CO] for the scenario TR. For [$CH_3C(O)CHO$] and [ORGNTR] there are decreases (increases) of between 20-500% and 15-20% between the op_run and TM4 (TM5), respectively. This is a direct result of the modification of the scaling ratios for these two species. Only negligible differences occur between the op_run and full_run for these two species. The resulting changes in tropospheric O_3 are similar to those shown in Figure 4, therefore the changes induced by updating the ϕ_{O^1D} values remain largely intact for all scenarios

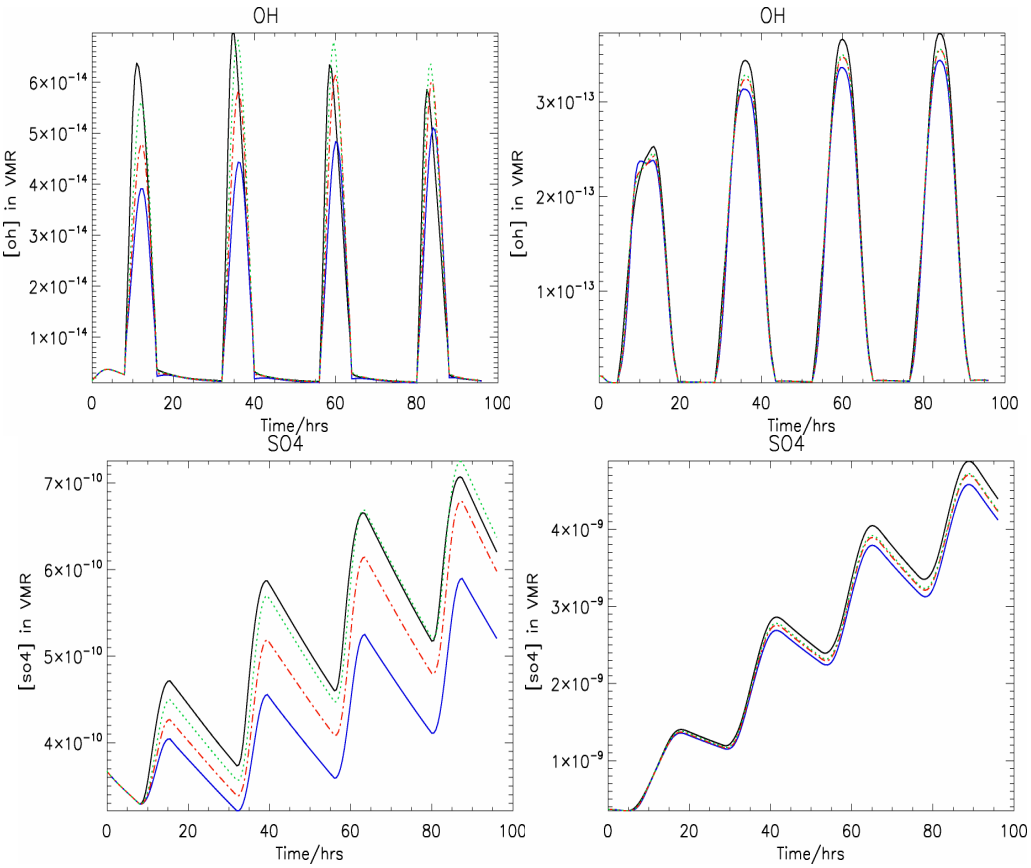

Figure 9: The effect of updating the photolysis data on [OH] and [SO_4] for scenarios URW (left) and URS (right) showing increases (decreases) in the rate of the production of SO_4 compared to TM4 (TM5). Changes are shown for TM4 (—) and TM5 (—) against those using the op_run (---) and the full_run (---).

As for TM4 versus TM5, the largest differences between the op_run and the full_run simulations occur for the urban scenarios, where anthropogenic emissions exert the strongest influence on (e.g.) tropospheric O_3 production and also where the resident [HCHO] and [$CH_3C(O)CHO$] are the highest of all the scenarios. Figures 9a-d show the differences for both [OH] and [SO_4] for the scenarios URW and URS, respectively, where the production rate of SO_4 is determined exclusively via reaction KSO2OH (see Appendix B). For URW it can be seen that for TM4 the rate of SO_4 production is ~50% lower than that calculated in TM5. This is related to the perturbation in the HO_x budget introduced via differences in J_{MGLY}. Moreover, comparing the op_run with the full_run shows that [OH] in the full_run is consistently higher than that calculated using the op_run by between 2-10% regardless of the season, similar to that shown in Figure 4 and due to similar reasons.

Another important effect of these differences in J_{MGLY} is the modification in the concentration of reactive nitrogen that is present in the system as discussed in Section 3.1. Figure 10 shows comparisons for [NO], [NO_2], [PAN] and [HNO_3] between TM4, TM5, the op_run and the full_run. Comparing the TM4 and TM5 simulations shows that for the scenario URW the total amount of nitrogen stored in reservoir compounds is much higher for TM5 than TM4 (considering that approximately 10 times as much PAN exists in the system). Moreover, the soluble fraction is higher for TM4 than TM5 for the urban scenarios due to the differences in the partitioning (c.f. Fig 10c). This could explain the difference seen in the regional loss of nitrogen via wet deposition between TM4 and TM5 for (e.g) East asia (Dentener et al, 2006). The higher [PAN] in TM5 will also introduce differences with respect to the global distribution of nitrogen, where PAN is subject to long-range transport. Finally, for this scenario the amount of reactive nitrogen available in TM4 is much higher as shown in Figures 10a and b. Comparing the op_run and full_run shows that the op_run has ~40% less reactive nitrogen available due to an over production of both PAN and HNO_3. Further analysis is limited to Section 4 where the application of all updates to both the reaction data and photolysis data occurs simultaneously.

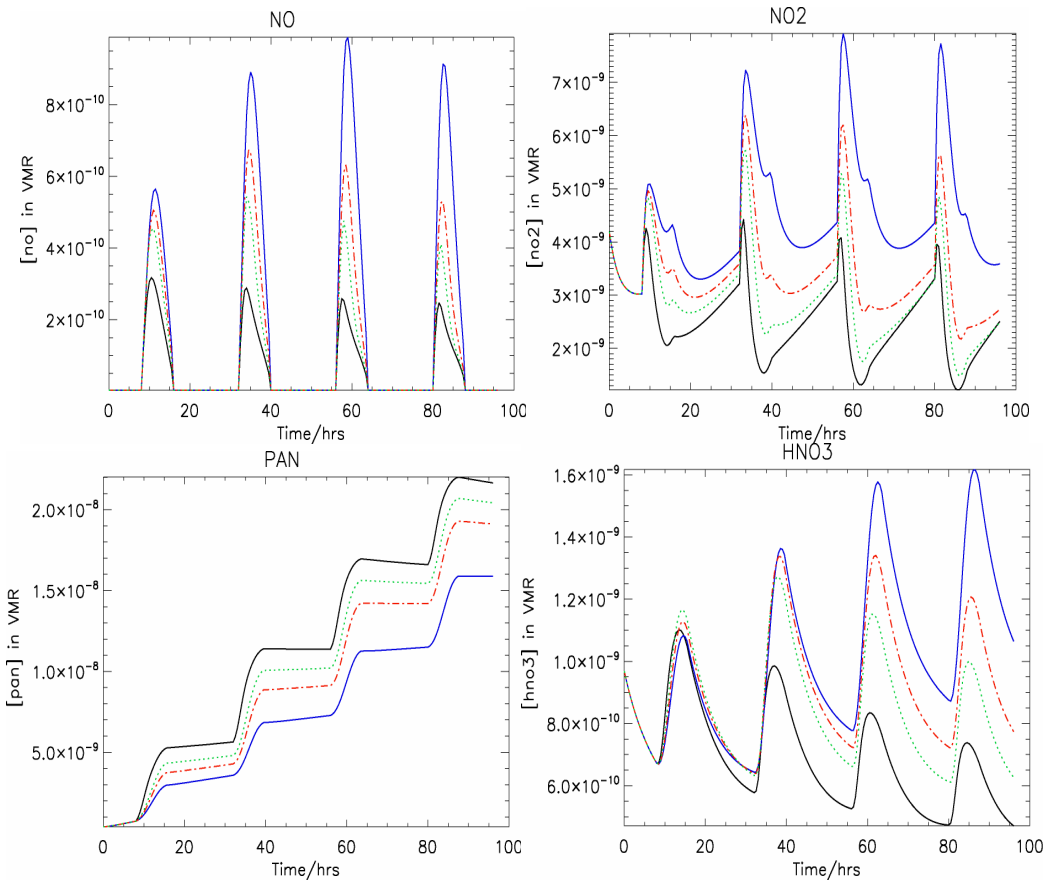

Figure 10: The effect of updating the photolysis data on [NO], [NO_2], [PAN] and [HNO_3] for the URW scenario where decreases (increases) in reactive nitrogen occur compared to TM4 (TM5). Changes are shown for TM4 (—), TM5 (—) op_run (-·-·-) and full_run (····).

4. The effect of updating the modified CBM4 mechanism on Atmospheric Composition

For the purpose of investigating the chemical effects introduced by updating both the reaction rate and photolysis rate data simultaneously we define a number of sensitivity studies in order to determine the main causes of the most significant differences. Table 3 summarises the subset of reactions selected for each of the sensitivity tests. In general, for the explicit reactions (e.g. KNOO3) the relevant data was taken directly from the latest recommendations (Sander et al, 2006; Atkinson et al, 2006). For reactions containing lumped species we provide details of the chosen parameters below. For more comprehensive details regarding the actual input data used for the updates the reader is referred to Appendix F.

Sensitivity test	Details of test	Reactions
SENSNOX	Inorganic reaction involving NO_x	KNOO3, KHO2NO, KMO2NO, KNO2OH, KNO2NO3, KN2O5, KNO2HO2 and KC46
SENSGHG	Reactions involving HO_x with CH_4, CO and O_3	KODM, KH2OOD, KO3HO2, KCOOH, KO3OH, KCH4OH, KHPOH and KH2OH
SENSRO2	Reactions involving RO_2	KMO2HO2, KMO2MO2, KHO2HO2, KC49-50, KC79-81, KC82 and KC85
SENSORG	Reactions involving HCHO and organics	KFRMOH, KC43-44, KC57-59, KC61-62, KC73, KC76-78, and KC84
SENSPAN	Update of Keq(PAN) only	KC47, KC48

Table 3: Definitions of the sensitivity tests used to identify the source of the most important changes which occur when updating the reaction rate data to the latest recommendations. For these sensitivity tests no updates were made to any of the photolysis rates.

Before we present the main differences that occur as a result of updating the modified CBM4 mechanism, we briefly highlight the most significant updates made to the gas phase reaction rates listed in Appendix F. For [OH] the production efficiency is reduced by an increase in the quenching of $O(^1D)$ via KODM by ~12%. Temperature dependencies are introduced for the fundamental reactions KH2OOD and KFRMOH. There is also a reduction by ~25% in the conversion rate of OH to HO_2 via KH2OH, where the scaling of KH2OH to KCH4OH is completely removed (see Appendix B) and the resident $[H_2]$ increased from 500 nmol/mol to 550 nmol/mol (Brasseur and Schimel, 1999). For the nitrogen reservoirs there is a ~30% increase in the formation rate of HNO_3 and a reduced decomposition rate for PAN (KC48). For CH_3O_2 there are reductions in the reaction with HO_2 and CH_3O_2 by ~10% and ~20%, respectively. For the reaction of $CH_3C(O)O_2$ with NO, HO_2 and $CH_3C(O)O_2$ there are changes of –83%, 775% and 217%, respectively, where the reaction data is now available for each explicit reaction. For Isoprene the oxidation by OH increases by ~18%, whereas the oxidation by O_3 and NO_3 both decrease by ~10%.

For KCOOH the formulation of the reaction now proceeds via two separate channels accounting for the formation, and subsequent decomposition, of an association complex, as described by reactions (6), (7) and (8):

$$OH + CO(+ M) \rightarrow H + CO_2 \quad (6)$$

$$OH + CO(+ M) \rightarrow HOCO \quad (7)$$

$$HOCO + O_2 \rightarrow HO_2 + CO_2 \quad (8)$$

Under atmospheric conditions k_8 = 1.5 x 10^{-12} cm^3 $molecule^{-1}$ s^{-1} at 298K, meaning that the decomposition is essentially instantaneous. Previous recommendations (e.g. Sander et al., 2002) simply declared reaction (6) with a pressure dependency derived for [N_2] = 0-1 bar between 200-300K. However, tropospheric temperatures often exceed 300K at ground level, especially under tropical conditions; therefore a more sophisticated treatment is needed. Here, we choose to use the formulation given in Sander et al. (2006) as Atkinson et al. (2006) imply that both reactions (6) and (7) need to be accounted for in order to account for the diverse range of temperatures and pressures found in the atmosphere. This results in a decrease in KCOOH of a few percent at standard temperature and pressure (see Appendix F).

For the lumped radical operator species XO2 and XO2N we make the following changes. For the reactions of XO2 with other radicals we take the average of the latest recommendations (Atkinson et al., 2006) for the rates of reaction of $CH_3CH_2O_2$ and $CH_3CH_2CH_2O_2$ (in the various isomers) with the respective radical (e.g.) HO_2 or with themselves depending on the stiochiometry of the reaction. For the reaction of NO + XO_2N (KC81) and HO_2 + XO_2 (KC82) we adopt the rates given in Yarwood et al. (2005b) due to a scarcity of laboratory data. For the production of ROOH (KC85) the rate changes implicitly as a result of updates to KC82 and KC79, where KC85 is equal to the ratio of (KC81 + KC82)/KC79. For the oxidation of ORGNTR and ROOH we again adopt the rates given in Yarwood et al. (2005b).

For brevity we do not discuss or show changes introduced by each sensitivity test but rather the cumulative effects introduced when applying all the updates to both the reaction rates and photolysis data together. For this purpose we again define an op_run and a full_run simulation, with the difference being that the op_run only contains the updates to the photolysis rates as defined in the op_run in Section 3.5. Comparisons are shown versus both TM4 and TM5 throughout.

4.1 The Changes concerning Tropospheric O_3 and OH

Figure 11 shows the change in both tropospheric O_3 and OH for scenarios MAS, RLS, URS and TR. For the majority of the scenarios the growth in tropospheric O_3 over the simulation period is identical for both TM4 and TM5, except for URS and URW, where the high [$CH_3C(O)CHO$] results in moderate differences (see Section 3.1). The influence of updating the reaction data is to reduce the production rate significantly resulting in ~10% less [O_3] by the fourth day of the simulations. This is predominantly due to the reduction in the availability of reactive nitrogen and the updates to the reaction rates associated with the higher organics as seen in SENSNOX and SENSORG (not shown). It is encouraging that the differences between the op_run and the full_run are limited to a few percent, with the full_run being consistently higher. For [OH] there are decreases of ~20% during the daytime across a range of scenarios. Therefore the increases in [OH] shown in Figure 9 associated with updating the photolysis rates are subsequently negated by the updates to the reaction data related to the formation of [OH] and the partitioning of NO_x, as determined in the SENSNOX and SENSGHG sensitivity tests (not shown). Again the differences between the op_run and full_run are limited to a few percent for specific scenarios.

Figure 12 shows the resulting effect on the oxidation of CH_4 by examining the differences in [CH_3O_2] as a convenient proxy for identical scenarios as those shown in Figure 11. As would be expected the resident [CH_3O_2] decreases in line with the decreases in [OH] shown in Figure 11. This negates the increase in [CH_3O_2] seen in the SENSRO2 sensitivity test (not shown), which occurs as a result of the decrease in the loss rates KMO2HO2 and KMO2MO2 (see Appendix F). Therefore the lifetime of CH_4 (hereafter denoted as $\tau(CH_4)$) increases in the box model as a result. For TM4 and TM5 the resident [CH_3O_2] is essentially identical. Moreover, it becomes apparent that there is generally ~5% less [CH_3O_2] in the full_run as compared with the op_run. This effect increases to ~10% in more remote regions (c.f. Fig 12a with 12b). The only exception is for scenario MAA, where the increased influence of the enhanced photolysis of HCHO results in a noticeable increase in [OH] in the full_run of a few percent (not shown). This occurs in spite of the application of the high angle band settings, although these do moderate the increase in OH.

For other species oxidized by OH (e.g.) SO_2 there are related decreases in the oxidation rate (not shown). For the some of the higher organics the increase in their atmospheric lifetimes due to a lower [OH] is offset by the simultaneous increase in the rate of oxidation due to the updates made to the reaction data (e.g.) Isoprene. One of the most influential effects

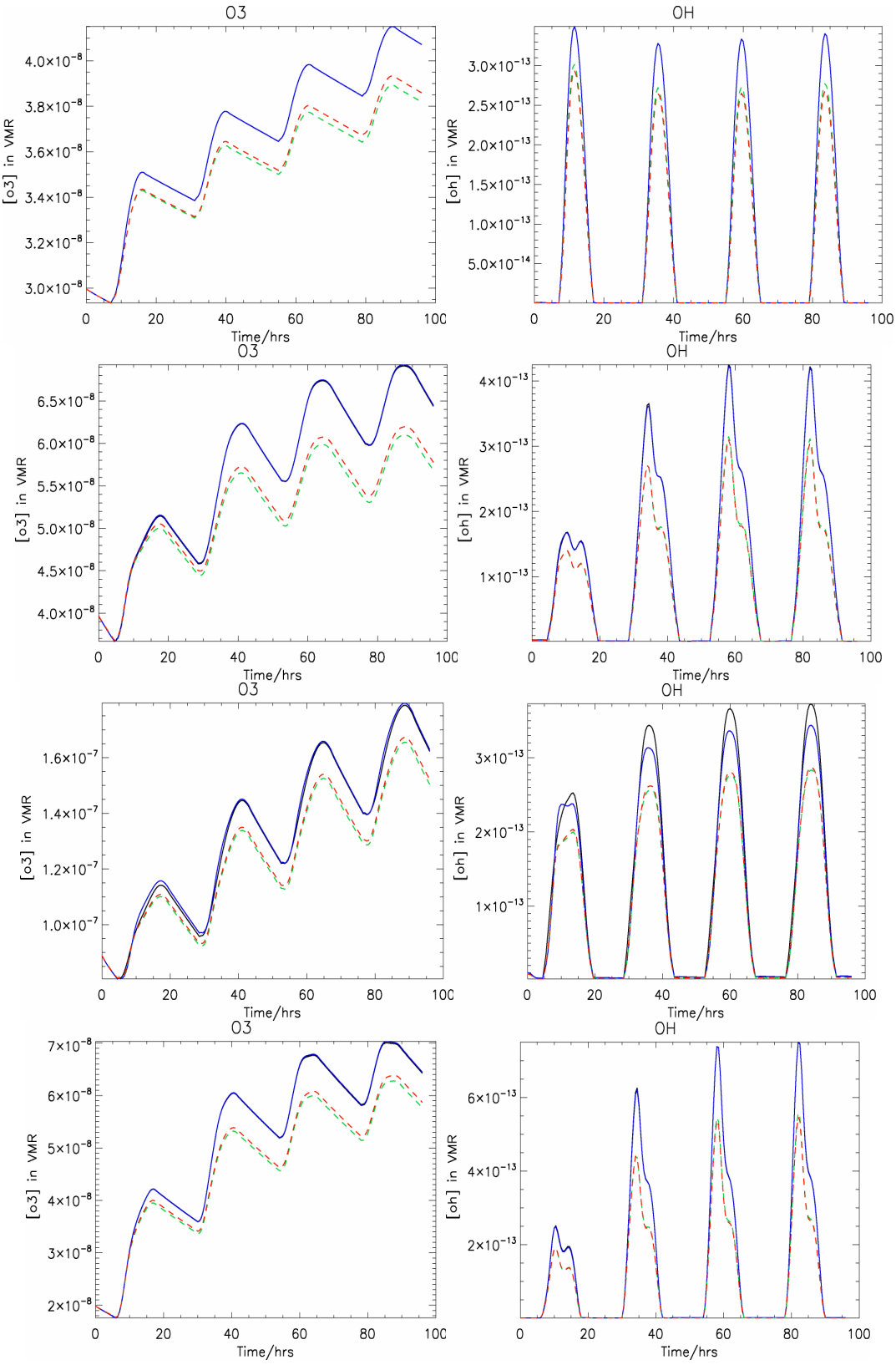

Figure 11: The effect of updating the modified CBM4 mechanism on tropospheric O_3 (left) and OH (right) for scenarios MAS, RLS, URS and TR. Comparisons are shown for TM4 (—), TM5 (—), the op_run (- - -) and the full_run (- - -).

concerns the decrease in the removal of ORGNTR via OH (KC84) which, in conjunction with the update to J_{ORGN}, results in a substantial increase in the partitioning of nitrogen into a more chemically passive form (see next section). This also contributes to the decrease in tropospheric O_3 by reducing the net flux of $O(^1D)$ production via J_{NO2}.

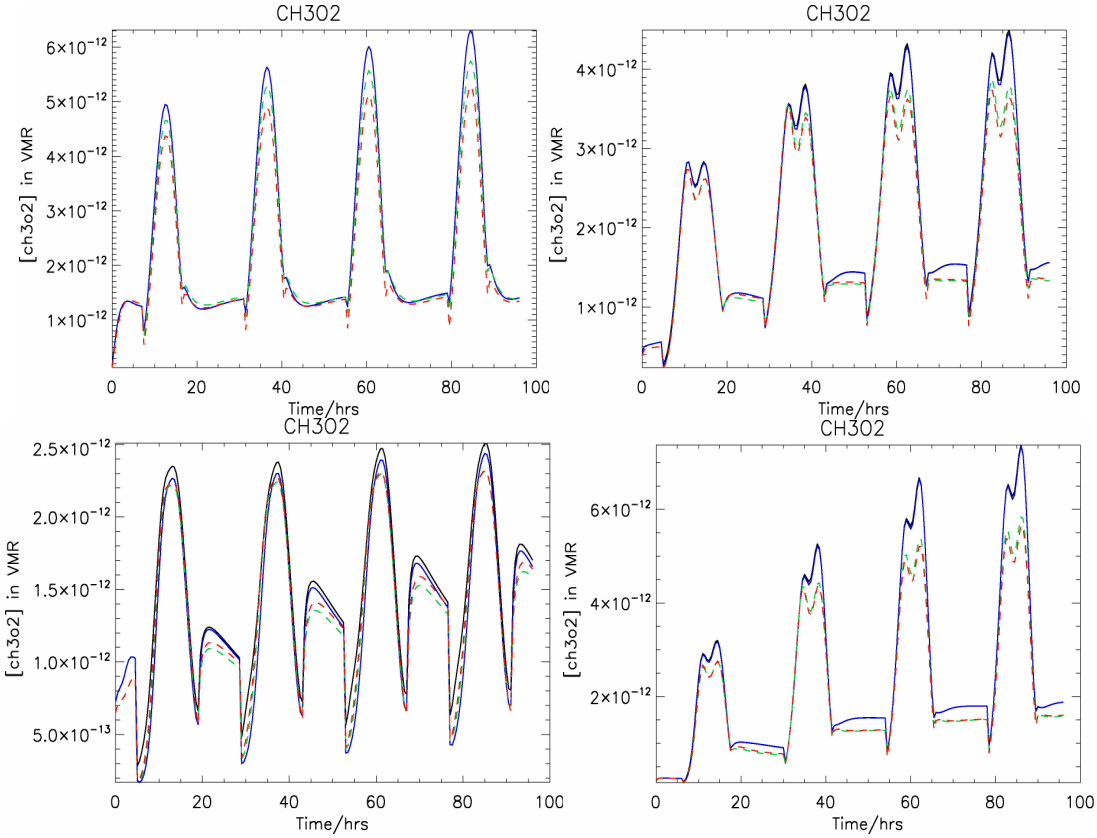

Figure 12: The effect of updating the modified CBM4 mechanism on the oxidation of CH_4 for scenarios MAS, RLS, URS and TR. Comparisons are shown for TM4 (—), TM5 (—), the op_run (- - -) and the full_run (- - -).

4.2 The Changes concerning CO

In section 3.3 we have shown that the one of the main effects of increasing both J_{aCH2O} and J_{bCH2O} is an increase in the *in-situ* formation rate of CO. Therefore we re-visit this to see whether this effect is enhanced by the reduction in OH shown above. Moreover, the modification in KFRMOH means that both of the main gas-phase removal routes for HCHO have been updated. Figures 13a-f shows the resulting change in both [HCHO] and [CO] for scenarios MAA, RLS, URS and TR, respectively. Here it can be seen that loss of [HCHO] in the full_run is compensated for by the update of the reaction rate data compared to when only the photolysis rates are updated (c.f. Figure 6b with Figure 14c). For the op_run the [HCHO] increases across a range of scenarios as compared to both TM4 and TM5 because of the missing update for both J_{aCH2O} and J_{bCH2O}. Again it should be noted that the high solubility of HCHO means that the effects shown in Figure 13 related to HCHO are most likely to be moderated when applied in a global CTM. For the associated change in [CO] it can be seen that the increase in the *in-situ* formation still occurs, where the highest growth rate is simulated for the full_run as a consequence of the contribution by the additional photolysis of HCHO. This has an effect even for scenarios that have high local emissions (e.g. URS). Contributions to this increase are simulated in SENSGHG, SENSORG and SENSNOX, which nullify the decreases in [CO] seen in SENSRO2. Moreover, these increases in CO enhance the chemical destruction of OH via reactions (6) and (7).

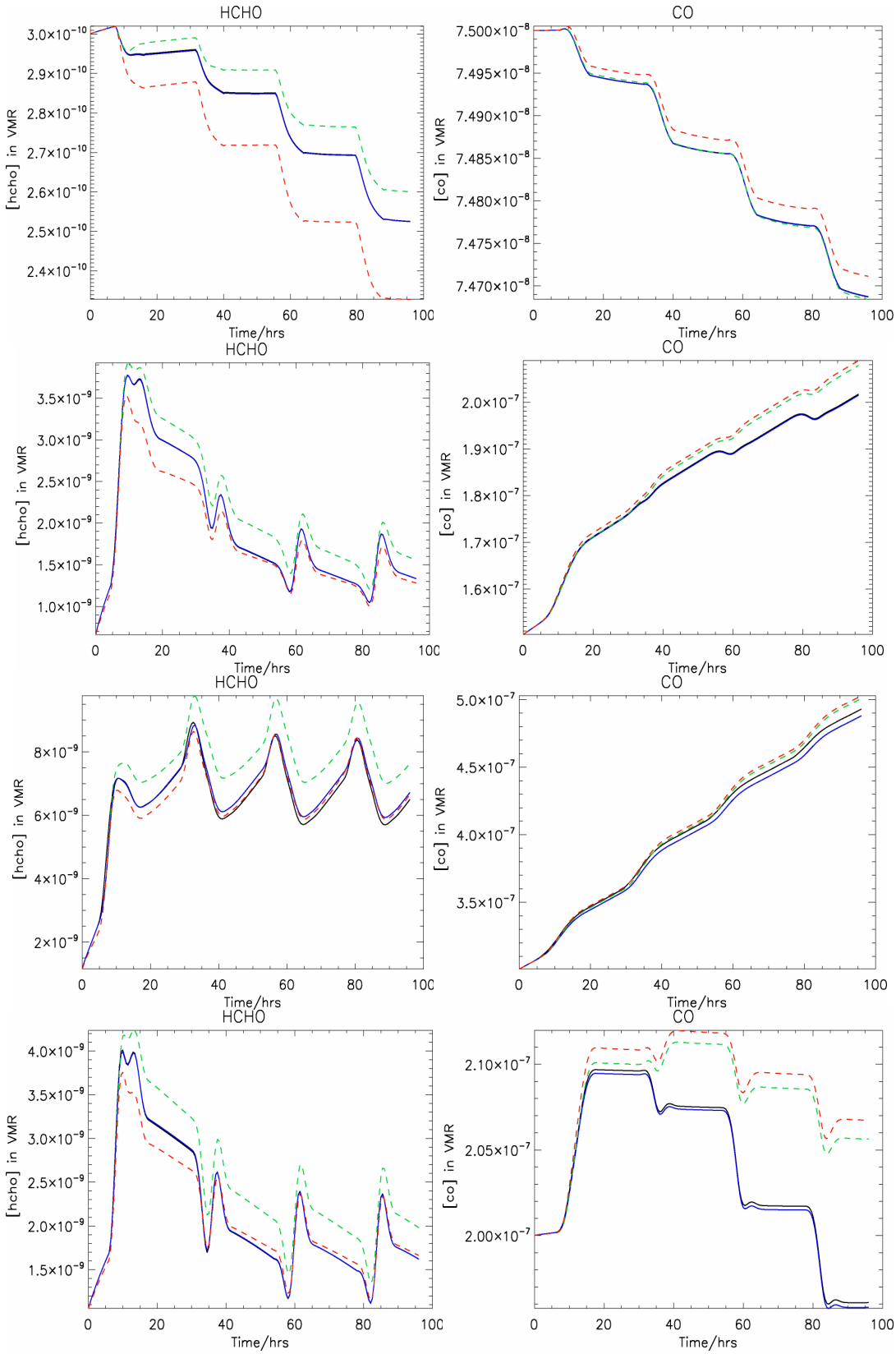

Figure 13: The effect of updating the modified CBM4 mechanism on [HCHO] (left) and [CO] (right) for scenarios MAA, RLS, URS and TR. Comparisons are shown for TM4 (—), TM5 (—), the op_run (- - -) and the full_run (- - -).

4.3 The Re-distribution of NOx into Nitrogen containing of Reservoir Species

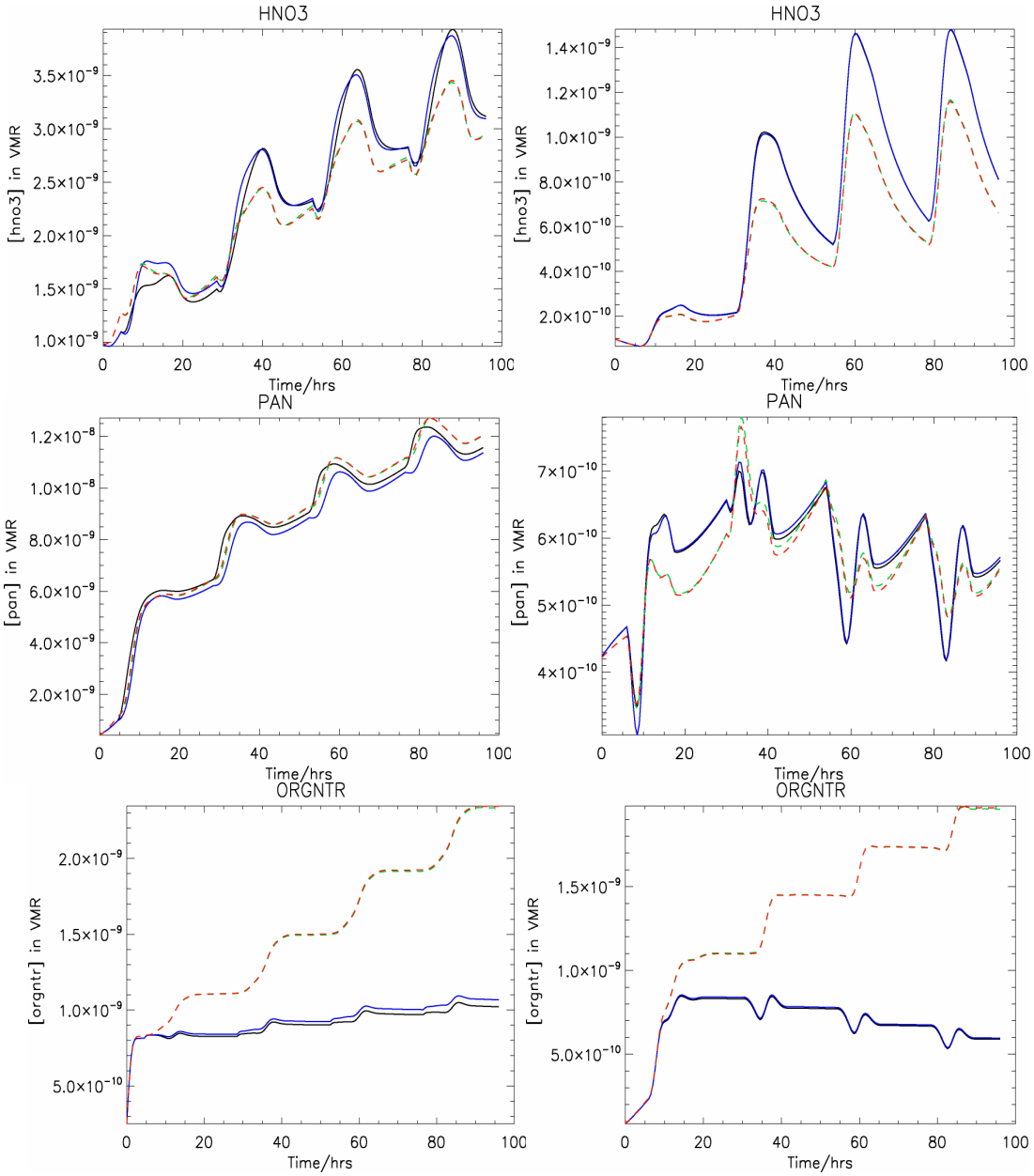

Figure 14: The effect of updating the modified CBM4 mechanism on the re-partitioning of reactive nitrogen for scenarios URS and TR. Plots are shown for HNO_3, PAN and ORGNTR, which act as important reservoir species in the modified CBM4 mechanism. Comparisons are shown for TM4 (—), TM5 (—), the op_run (- - -) and the full_run (- - -).

In section 3.5 we have shown that updating the photolysis rates results in a re-partitioning of nitrogen for the urban scenario. Introducing the new reaction data has the potential to increase this effect due to the reduction in OH shown in Section 4.1. Moreover, the reduction in the release of nitrogen from stable reservoirs (e.g.) the decrease in KC84 (OH + ORGNTR) by ~90% also has the potential to enhance this re-partitioning. Figure 14 shows the re-partitioning of nitrogen for scenarios URS and TR.

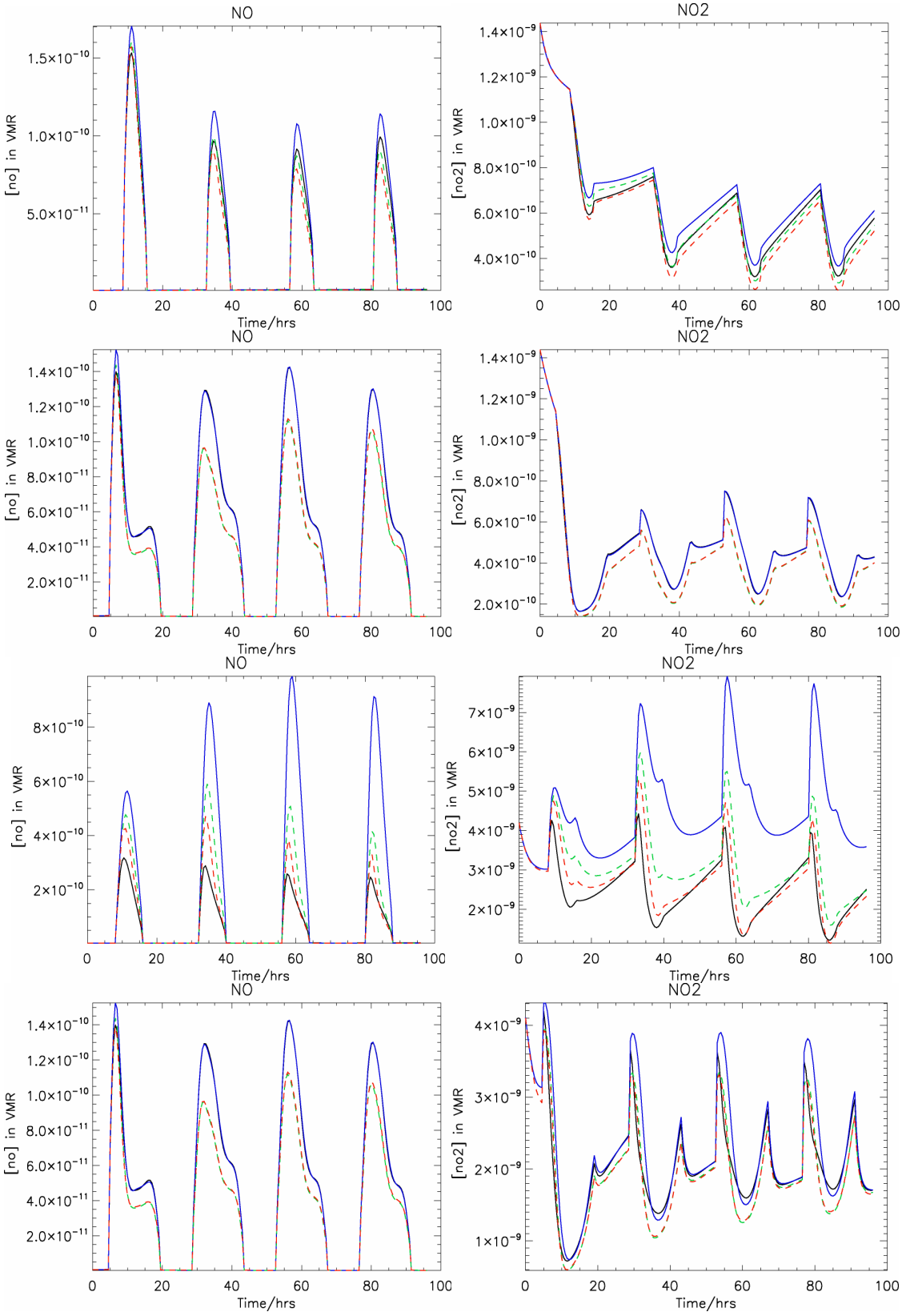

Figure 15: The effect of updating the modified CBM4 mechanism on [NO] and [NO_2] for scenarios RLW, RLS, URW, and URS. Comparisons are shown for TM4 (—), TM5 (—), the op_run (- - -) and the full_run (- - -).

For these scenarios it can be seen that there is a reduction in [HNO_3] of ~30% with an associated increase in both [PAN] and [ORGNTR] of ~10% and ~50%, respectively, as compared to both TM4 and TM5. Therefore, the ~28% increase in KNO2OH does not result in higher [HNO_3] when applying all of the updates due to both the decrease in [OH] and the availability of NO_2 (see below).

The substantial increase in [ORGNTR] is caused by both an increase in the formation rate (KC81) and a decrease in both the photolysis rate and the reaction with OH (see Appendix F).

In a CTM this reduces the fraction of nitrogen available for wet deposition (where HNO_3 is highly soluble) and increases the fraction of nitrogen that can be transported to higher altitudes by convection (see Section 5). For wintertime scenarios the increases in [ORGNTR] are limited although decreases (increases) occur for HNO_3 compared with TM4 (TM5) due to the effect of J_{MGLY} (see section 3.5). For the low NO_x scenarios (e.g. MAA, MAS) the [ORGNTR] increases in a similar manner to scenario TR (albeit by only a few 100pptv), with the [HNO_3] remaining unchanged

In Figure 15 we show the resulting effects on reactive nitrogen for both the rural and urban settings, where the highest [NO_x] régimes are found. With the exception of the URW scenario there are generally decreases in both [NO] and [NO_2] as compared with both TM4 and TM5, as would be expected considering the increased fraction of nitrogen that is stored in the reservoir compounds. This contributes to the decrease in tropospheric ozone discussed in section 4.1. In Figure 16 we show the effect on [NO_3] for identical scenarios. Due to the high photolysis rate this radical has maximal concentrations during the night, where it has a large influence on the oxidation capacity of the atmosphere due to the absence of OH. It can be seen that for summertime scenarios, there is a decrease by between ~30-50%. There is also a similar reduction in [N_2O_5], which again reduces the amount of nitrogen lost by heterogeneous scavenging on aqueous aerosol. For wintertime scenarios there is generally an increase by 5-10%. For the URW scenario the behavior compared to TM4 (TM5) is different in line with the differences simulated for the other nitrogen containing species.

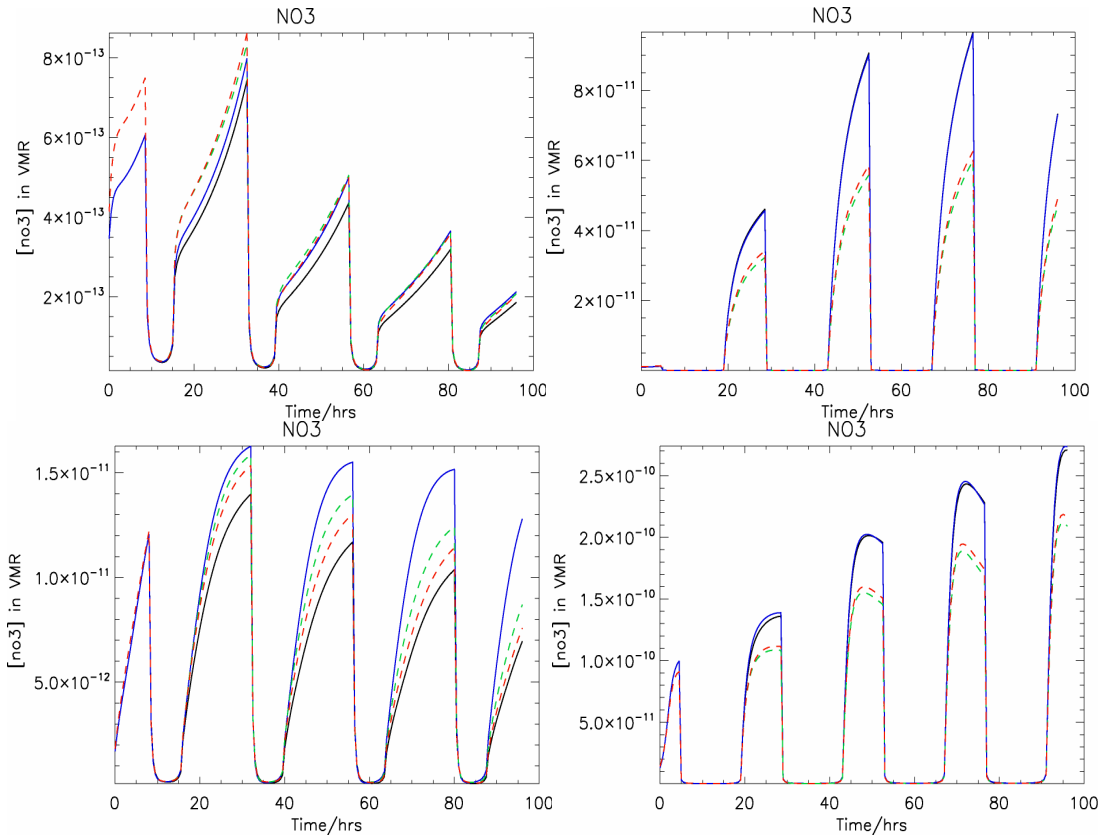

Figure 16: The effect of updating the modified CBM4 mechanism on [NO_3] for scenarios RLW, RLS, URW, and URS. Comparisons are shown for TM4 (—), TM5 (—), the op_run (- - -) and the full_run (- - -).

5. The Application of the Operational Updates in a Global CTM

In section 4 we have shown that many of the updates to the chemical reaction data discussed in this report can be introduced into the TM model immediately without the need for any lengthy upgrade to the CTM such as introducing the calculation of online photolysis rates. Although such an upgrade is deemed necessary in the long term, the updates can be tested in the context of (e.g.) the retrieval of tropospheric NO_2 columns without delay. It is also necessary to determine whether the changes in the resident concentrations of important trace gases calculated during the box model studies are in any way moderated by mixing processes, the use of different emission datasets and heterogeneous scavenging of soluble species (e.g. HNO_3). The prolonged transport times of ORGNTR away from source regions as a result of the increase in the atmospheric lifetime should result in interesting modifications to both NO_x and O_3 for regions such as the Tropics and more remote regions (e.g. South Pacific). Moreover, the temperature/pressure combinations found in the upper troposphere are typically different than those adopted from the AFGL profiles in the box model. This has the potential to enhance the effect of introducing new rate dependencies for dominant reactions such as KH2OOD and KFRMOH. Finally, the actinic fluxes used for the calculation of photolysis rates in TM4 are extracted from a look up table that adopts a single AFGL profile (for the Tropics) and clear sky conditions, although cloud coverage is included in the derivation of the total optical depth through the atmospheric column. This may result in significant differences to the resulting *J* values to those shown in the box-modelling study.

For this purpose we perform simulations using the version of TM4 that has recently participated in a host of model intercomparison studies (e.g. van Noije et al., 2006; Stevenson et al., 2006; Shindell et al., 2006). Since participating in these intercomparison studies a number of modifications have been made to the TM4 model, which are described as follows; (i) the total ozone column has been reduced by ~10% as a result of an error associated with the summation of the over head column, (ii) the partitioning of the NMV emissions has been reduced for PAR, OLE and MGLY (see Appendix G), (iii) the emission of isoprene is distributed over the first 200m to dampen surface concentrations in the tropics, (iv) the loss of OH by the reaction with SO_2 is now accounted for in the EBI solver, (vi) the biogenic emission of acetone given in the POET emission inventory is included as PAR (as defined in Yarwood et al., 2005), (v) the value of the γ_{N2O5} has been decreased to 0.02 from 0.04 according to the recommendation of Evans and Jacob (2005) and (vi) an updated method of convective scavenging is used.

For the baseline case the reaction data used to calculate the chemical rates is given in Appendices B and C (*i.e.*) the original scaling ratios for J_{MGLY} and J_{ORGN} are still adopted (hereafter referred to as the tm4_baseline_run). In this instance the J_{MGLY} value is set equal to J_{bCH2O} (in line with the original IPCC version of TM4 and that currently used for the retrieval of satellite products from (e.g.) OMI). For the updated chemistry the selection of updates is as defined above in Section 4 and Appendix F (hereafter referred to as tm4_op_run). Two further simulations are performed which include $CH_3C(O)CHO$ as a transported tracer to vent the lowest layer and account for an atmospheric lifetime of ~5hrs (see section 6.1 below). Moreover, dry deposition is added for $CH_3C(O)CHO$ using fluxes which are identical to HCHO following the approach of von Kuhlmann (2001). These runs are hereafter referred to as tm4_baseline_mgly and tm4_op_run_mgly, respectively.

All simulations are conducted for the year 2000 using 25 vertical layers and a horizontal resolution of 3° x 2°, with the emission sources and injection heights being identical to those defined in the IPCC study (see full details in Stevenson et al. (2006)). For the biomass burning emission datasets we adopt the average for 1997-2002 from the GFEDv1 database (van der Werf et al., 2003) rather than a specific dataset for the year 2000. The methane is constrained at 1760ppmv throughout the troposphere without any vertical or latitudinal gradients. A spin-up period of one year was used for the tm4_baseline_run and the tm4_op_run_mgly in order for the chemical system to attain equilibrium. For the tm4_op_run and tm4_baseline_mgly run a shorter period of 4 months was used taking initial fields from the tm4_baseline_run. The sensitivity studies presented here allow an independent determination of the influence of transporting $CH_3C(O)CHO$ from the changes introduced by updating the reaction rate data. Therefore, we analyse the budget of these runs to differentiate which updates cause the most influential effects. This allows one to assess the influence of the changes made to the TM model on (e.g) the lifetime of methane (hereafter referred to as $\tau(CH_4)$) as compared to the values given in Stevenson et al, (2006).

Since the IPCC ensemble runs there have been updates to the anthropogenic emission datasets in order to account for the under-estimation in the growth in emissions made during the IPCC assessment. These new emission estimates have been made available during the Royal Society modelling exercise entitled "Ground-level ozone in the 21st Century" (D. S. Stevenson, private communication, http://www.royalsoc.ac.uk). This results in a ~15% increase in the global emission of anthropogenic pollutants such as CO and NO_x. Comparing the resulting NO_x with the emissions applied in the IPCC assessment reveals that these changes are not homogeneous (e.g.) for Eastern Europe there is actually a decrease to account for the faster implementation of abatement technologies than was predicted in the IPCC assessment (Stevenson and Zheng, private communication, 2007). Therefore we also perform identical simulations as for the tm4_baseline_run and tm4_op_run in order to assess the influence of the updates when applied to another set of emissions. However, no figures are shown regarding the resulting differences, but these simulations are included in the analysis of the chemical budgets. An additional sensitivity test is performed using the updated biomass burning NO_x emissions and the GFEDv1 emission dataset for 2000 as described in van Noije et al. (2006), where comparisons made for O_3 against co-located sonde measurements which are shown in Appendix H. For this simulation a latitudinal gradient is also applied for surface CH_4 and a diurnal cycle imposed on the isoprene emission.

The following analysis is conducted on monthly mean tracer fields for the month of December 2000 for the tm4_op_run_mgly simulation. Although days are short in the NH, meaning less photo-dissociation, this month was chosen as it shows the integrated effects of the differences over an entire year. To analyse the changes which occur we show both surface concentrations and transects which pass through a longitude of 5°E upto 100hPa (hereafter referred to as the 'chosen cross-sections'). This transect passes through regions influenced by both high industrial and transport emissions (i.e. the Benelux region) as well as a significant signature due to biomass burning for this time of year (Equatorial Africa). To avoid an exhaustive treatise we focus on the main effects discussed in Section 4 for long-lived trace gases meaning that we do not present figures for each of the 24 transported species. All percentage differences are shown with respect to the original tracer fields calculated using the tm4_baseline_run.

5.1 The Lifetime and Transport of $CH_3C(O)CHO$

One of the updates found to exert a dramatic effect on the resident concentration of important trace gas species during the box modelling studies was the five-fold increase in J_{MGLY} (from 10^{-5} s^{-1} to 10^{-4} s^{-1}, Figure 3). It was found that applying this update decreases the atmospheric lifetime (and thus concentrations) of $CH_3C(O)CHO$ significantly. This is warranted as resident [$CH_3C(O)CHO$] can exceed 20-30 ppbv during wintertime for industrial regions in TM4 when using the original reaction rates (see Fig. 17b), where measurements suggest that concentrations should be in the range of a few ppbv in urban areas (Grossman et al, 2003). Another factor which exasperates this problem is that $CH_3C(O)CHO$ is not transported. In order to account for the higher organic species which are not accounted for in the modified CBM4 mechanism $CH_3C(O)CHO$ is emitted with significant fluxes as an analogue for xylene over industrial regions. Such high concentrations have the potential to introduce a bias in the chemistry at the surface. To avoid this it was decided to include $CH_3C(O)CHO$ as a transported tracer for the simulations used for assessing the effects of the updates to the reaction rates. It should be noted that all other non-transported tracers declared in the TM model are short-lived free-radical species (except NO and NO_2 which are transported collectively as NO_x). Figures 17a-f show examples of global monthly mean fields for [$CH_3C(O)CHO$] during both June and December 2000 for the tm4_baseline_run, the tm4_op_run and the tm4_op_run_mgly, respectively. Here it can be seen that for the tm4_baseline_run the [$CH_3C(O)CHO$] exceeds 20 ppbv over parts of Europe, the Eastern US and Japan during the winter. Applying the new chemical rates improves on this as a result of the increase in J_{MGLY}, where the maximum [$CH_3C(O)CHO$] at the ground is reduced to between 5-6 ppbv over the industrial regions. Figures 17e and f show that introducing tracer transport for $CH_3C(O)CHO$ gives a further improvement, where the maximum [$CH_3C(O)CHO$] at the ground is reduced to between 0.5-1 ppbv. For the J_{MGLY} value applied in TM5 (see Section 3.1) the maximal [$CH_3C(O)CHO$] is also reduced to < 1ppbv (not shown). Moreover, it should be noted that the high [$CH_3C(O)CHO$] shown for the tm4_baseline_run is lower than that simulated in the original IPCC runs, where maximal concentrations reach over 100ppbv during wintertime, as a consequence of applying the original repartitioning ratios of the NMV component as given in Appendix G.

It should be noted that for [ISOP], which is introduced into the model using emission fluxes given by the Global Emissions Inventory Activity (GEIA), high concentrations of between 30-70ppbv at the ground occur in the tropics when the emission is limited to the lowest layer. Measurements taken over the Amazon indicate that it should be around 5-10 ppbv (von Kuhlmann et al, 2004). This has consequences for the resulting in-situ formation of MGLY via reactions KC76-KC78, as well

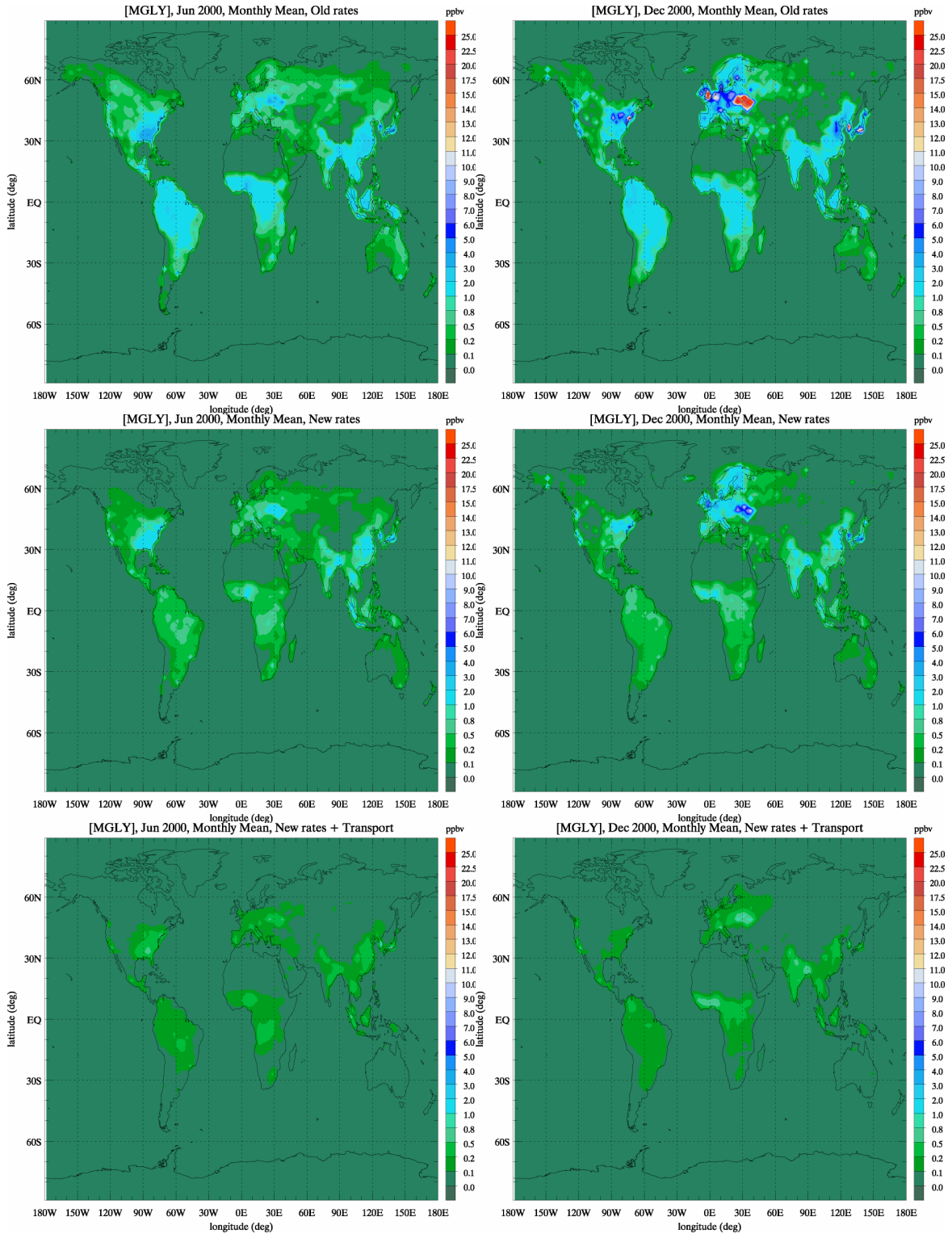

Figure 17: The effect of increasing the lifetime of $CH_3C(O)CHO$ in TM4 on the global monthly mean concentrations in the lowest layer for the tm4_baseline_run ((a) June 2000 and (b) Dec. 2000), the tm4_op_run ((c) June 2000 and (d) Dec. 2000) and the tm4_op_run_mgly ((e) June 2000 and (f) Dec. 2000).

as the depletion of OH, O_3 and NO_3. In order to address this we distribute the emission of isoprene in the first two layers in the tropics (20°N-20°S), which reduces [ISOP] to between 20-40ppbv (not shown), although a more sophisticated treatment needs to be introduced in the future such as a diurnal variation. The effect of introducing a diurnal emission flux on the budget of isoprene is discussed further in Section 5.3.

5.2 The Changes in the Global Distribution of Important Trace Gases

5.2.1 Tropospheric O_3

Here we show examples of the differences introduced for tropospheric O_3 for the chosen cross-sections. Figures 18a and b show the distribution of O_3 at the surface (between 0-50m) as calculated for the tm4_op_run_mgly simulation and the corresponding percentage differences which are introduced by applying the new reaction data and tracer transport of $CH_3C(O)CHO$. In the box model decreases in tropospheric [O_3] of between 5-10% were simulated for many of the scenarios (see Figure 11). However, the emissions of NO_x were spread homogeneously throughout the lowest kilometre of the atmosphere, whereas in TM the height at which emissions are introduced is dependent on the source of the emissions. Industrial emissions are introduced into the second and third layers of the model (which corresponds to 50-300m above the ground), using a distribution of 24% and 76%, respectively. Biogenic, domestic and agricultural emissions are introduced into the surface layer only. Terpenes are introduced into the model as additional isoprene using a ratio of two to one as defined in the IPCC exercise.

For biomass burning the emissions are introduced into the TM model between 0-6km, depending on the latitude of the burning event, in order to account for the additional pyrogenic convection (van Noije et al., 2006). This means that the surface layer is not directly affected by such emissions. This practise is adopted to account for the correct vertical distribution of gaseous emissions which originate from fires and to avoid the excessive titration of O_3 via the reaction KNOO3, which tends to occur when injecting the NO_x emission as NO into the lowest model layer only.

For surface [O_3] there are generally decreases of between 0-5% over the continents in the Northern and Southern Hemispheres (hereafter referred to as NH and SH, respectively). Exceptions are over Eastern Europe and Eastern China where these decreases reach 15-20%. For the outflow regions in the southern tropics there are increases of ~10% indicating that the transport of NO_x away from the source regions is more efficient as a result of the chemical updates (see next section). Moreover, increases of 0-5% also occur over the oceans in the SH, which was not seen in the box-model for a range of marine scenarios (see Fig. 13).

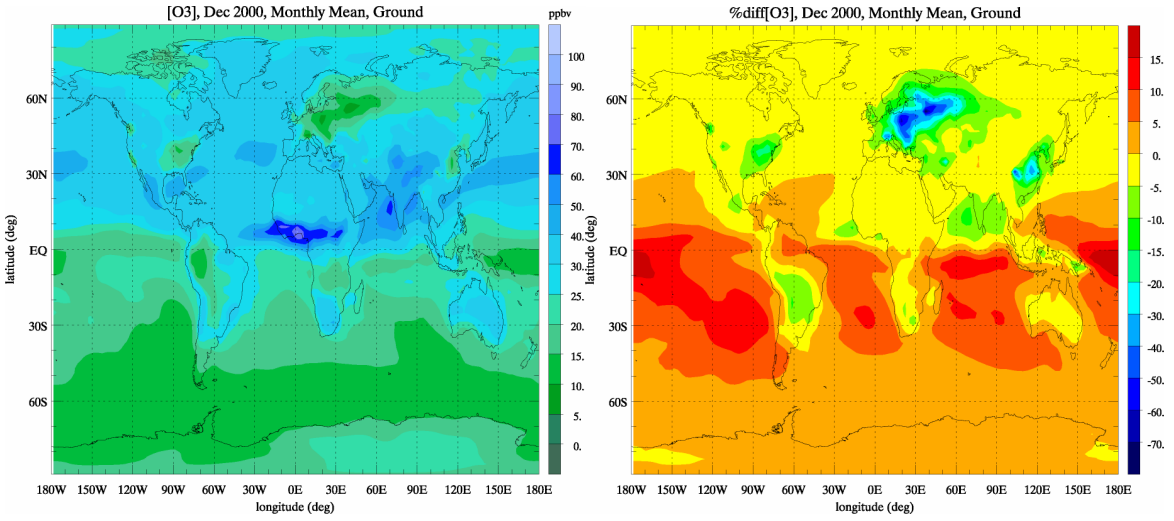

Figure 18: The global distribution of ozone at the surface as calculated using the updated reaction data (tm4_op_run_mgly) and the subsequent changes with respect to the current TM chemistry (tm4_baseline_run).

The largest surface [O_3] values in December for the tm4_op_run_mgly run occur in the tropics over Equatorial Africa (80-90ppbv) and the sub-tropics over the oceans around India (60-70ppbv), where these regions are affected by strong local emission fluxes of reactive gases from either biomass burning and/or anthropogenic activity, respectively. It is interesting

to note that for the Eastern US, Eastern Europe and Eastern China relatively low surface [O_3] values of 20-25ppbv occur. Comparing surface ozone values measured in Eastern Europe, which are available as part of the EMEP database, reveals that for (e.g) the Czech Republic (49.5°N, 16.2°E), Estonia (59.3°N, 25.5°E) and Latvia (56.1°N, 21.1°E) monthly means of ~35ppbv, ~40ppbv and ~25ppbv existed for December 2000. This indicates that the values simulated in TM4 are rather low for the Eastern European region. Moreover, decreases of between 10-40% occur as a result of the new reaction data. For the SH the background values typically range between 15-25 ppbv, which is the right order of magnitude (see Appendix H).

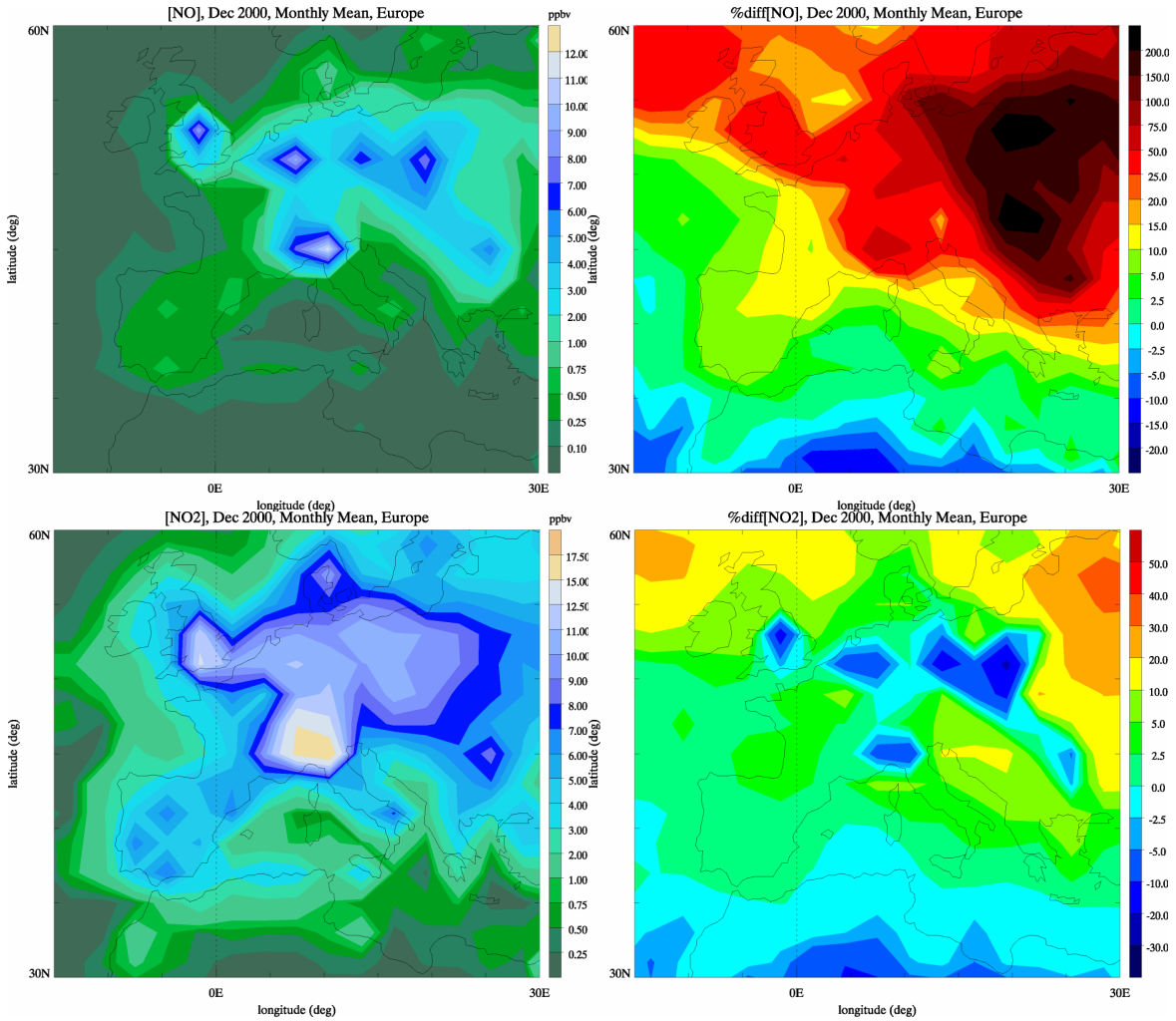

Figure 19: The monthly mean distribution of (a) NO and (c) NO_2 at the surface in Europe as calculated using the tm4_op_run_mgly. The percentage differences as compared to the tm4_baseline_run are shown in figures (b) and (d), respectively.

In order to understand the changes introduced with respect to surface O_3 it is useful to examine the effect of updating the reaction data on the availability of reactive nitrogen oxides (namely NO and NO_2), which, in the presence of sunlight, essentially determines the production efficiency of O_3. For this purpose Figures 19a-d show the monthly mean distributions of [NO] and [NO_2] at the surface over Europe, as simulated in the tm4_op_run_mgly, along with the corresponding percentage differences as compared to the tm4_baseline_run. These figures show that for the locations in Europe where [NO] is high there is a corresponding percentage increase of between 25-50% in the monthly mean value for December. This increase in [NO] is in contrast with the changes simulated in the box model for the scenario URW, where decreases of ~30% occurred (see Figure 12a). Moreover, the changes in [NO] in TM4 are also imposed on surface [O_3] (see Figure 18b). However, analysis of the chemical budgets reveals that the integrated annual loss of NO via KNOO3 decreases by ~21% in the NH, meaning that excess titration is not the cause of the decreases in [O_3]. For [NO_2], there are corresponding differences of between ±10% in the monthly mean values as shown in Figure 19d. These values are of the right order of magnitude as compared to the monthly mean values provided in the EMEP database for a range of

measurements sites (3-9ppbv in Central Europe for this period), although values in Spain are lower (1-3 ppbv for this period). The inter-conversion between NO and NO_2 is principally governed by reaction KHO2NO and J_{NO2} whose reaction rates remain unchanged during the updates (see Appendix F). However, the reduction in $[HO_2]$ (see section 5.2.3) results in the annual integrated production of NO_2 being ~12% lower in the NH, as determined from analysis of the chemical budgets. A dominating factor for the differences in surface $[O_3]$ is the repartitioning of reactive nitrogen into more long-lived reservoir species, which scavenges NO_2 near the source regions over time as discussed in the next section. This reduces the amount of O_3 formed via J_{NO2} by ~10% for the NH over the year. Moreover, typical $[NO]/[NO_2]$ ratios in the box model simulations range between 0.1-0.2 during wintertime, which is lower than the values of 0.3-0.5 that are shown in Figure 19. For the tm4_baseline_run ratios of between 0.2-0.4 exist, meaning that high [NO] is not solely a consequence of updating the reaction data. The screening of sunlight by clouds should reduce J_{NO2} over a typical month, meaning that the box model ratios could be considered as upper limits. It should be noted that all NO_x emissions are introduced into TM as NO.

Figures 20a and b show the distribution of tropospheric O_3 and the resulting percentage differences for a longitudinal transect taken at 5°E. Here it can be seen that there are differences of a similar magnitude to those seen for the lowest layer upto ~500hPa (c.f. Figure 18). The increases of between 0-5% above 200hPa have a dominant effect on the total ozone column due to the resident $[O_3]$ being much higher at these altitudes. Integrating the differences down from 100hPa it can be seen that the total ozone column increases more in the SH than the NH. This has consequences for other chemical species by reducing important *J* values at the ground by a few percent, which was not accounted for in the box model studies where the overhead total O_3 column remained fixed. Comparing differences for other model levels reveals that at 750 and 500hPa there are differences of ±5% for all latitudinal zones as compared to the tm4_baseline_run.

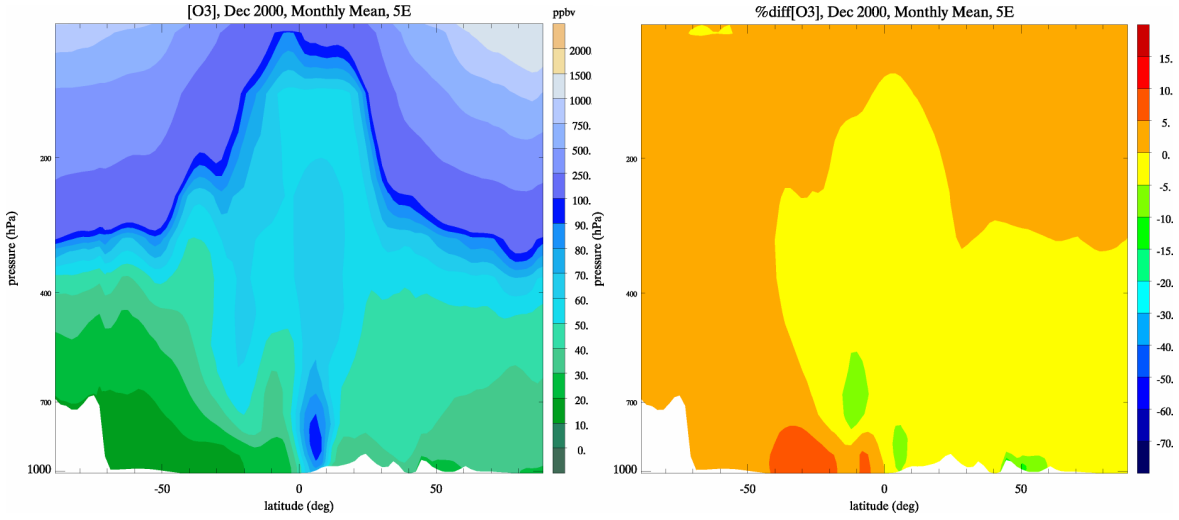

Figure 20: The monthly mean distribution of tropospheric ozone for December 2000 shown for a longitudinal transect taken at 5°E as calculated using the updated reaction data (tm4_op_run_mgly) and the subsequent changes with respect to the original reaction rates (tm4_baseline_run).

In order to assess whether updating the reaction data actually improves the performance of the model with respect to tropospheric ozone we show some co-located ozone profiles with those measured using ozonesondes in Appendix H. For the analysis we show the seasonal variation in the tropospheric O_3 column for De Bilt (52.1°N, 5.2°E), Paramaribo (5.8°N, 55.2°W), Sepang Airport (2.7°N, 101.7°W) and Neumayer (70.6°S, 8.2°W), where we compare TM4 profiles for the tm4_baseline_mgly, the tm4_op_run_mgly and the simulation using the GFEDv1 emission dataset for 2000. The differences between the TM4 runs are rather subtle and between ±5% as shown in Figure 20b. In general the use of the new reaction data improves the agreement with the measurements upto ~750hPa and reduces the agreement at higher altitudes. For the stations De Bilt, Sepang Airport and Paramaribo, TM4 overestimates $[O_3]$ by between ~50-100% upto 800hPa during wintertime. Moreover, for Sepang Airport and De Bilt, TM4 overestimates $[O_3]$ above 500hPa for this season by between 30-50%. For the summertime, with the exception of Sepang Airport, TM4 manages to capture the profiles quite well upto 750Hpa. For higher altitudes the model underestimates $[O_3]$ for De Bilt and Paramaribo. This implies that there is either a lack of convective transport of chemical pre-cursors to higher altitudes, an underestimation in the amount of lightning produced NO_x or the model fails to properly account for sufficient long-range transport of either

O_3 or NO_x. For TM5, which uses the same parameterization for convective mixing as TM4, it was found that convection is too weak during summertime from a simulation of SF_6 and CO_2 measurements (Boenisch et al, 2008). For Paramaribo there is a distinct peak in O_3 between 300-500hPa for most seasons that is related to a transport of polluted air masses from both within South America and across the Atlantic from West Africa, as determined by the trajectories shown on the SHADOZ website for season SON in 2000 (http://croc.gsfc.nasa.gov/shadoz/). The model is unable to capture this peak, even when increasing the model resolution to 34 layers and using the GFEDv2 biomass burning emission database (not shown). For Neumayer, which is situated at a remote location, TM4 manages to capture the vertical distribution of O_3 throughout the year. The use of the GFEDv1 biomass burning emission dataset introduces the largest effect for Sepang Airport, which is influenced by local emissions predominantly due to biomass burning.

For the African Continent vertical profiles of tropospheric O_3 are available from the MOZAIC flight data record (Marenco et al., 1998). These indicate that, although the spatial pattern of high surface O_3 shown in Figure 18a correlates with the number of fire counts for December, the surface [O_3] simulated in the TM model is rather high for this region (Sauvage et al. 2005). For instance, near Lagos (6.6°N, 3.3°E) and Abidjan (5.4°N, 4°W) surface O_3 ranges between 20-30 (±10) ppbv according to a mean of measurements over the period 1998-2002, whereas in TM4 the values are between 40-50 ppbv (see Figure 18a).

5.2.2 Nitrogen Reservoirs and NO_x

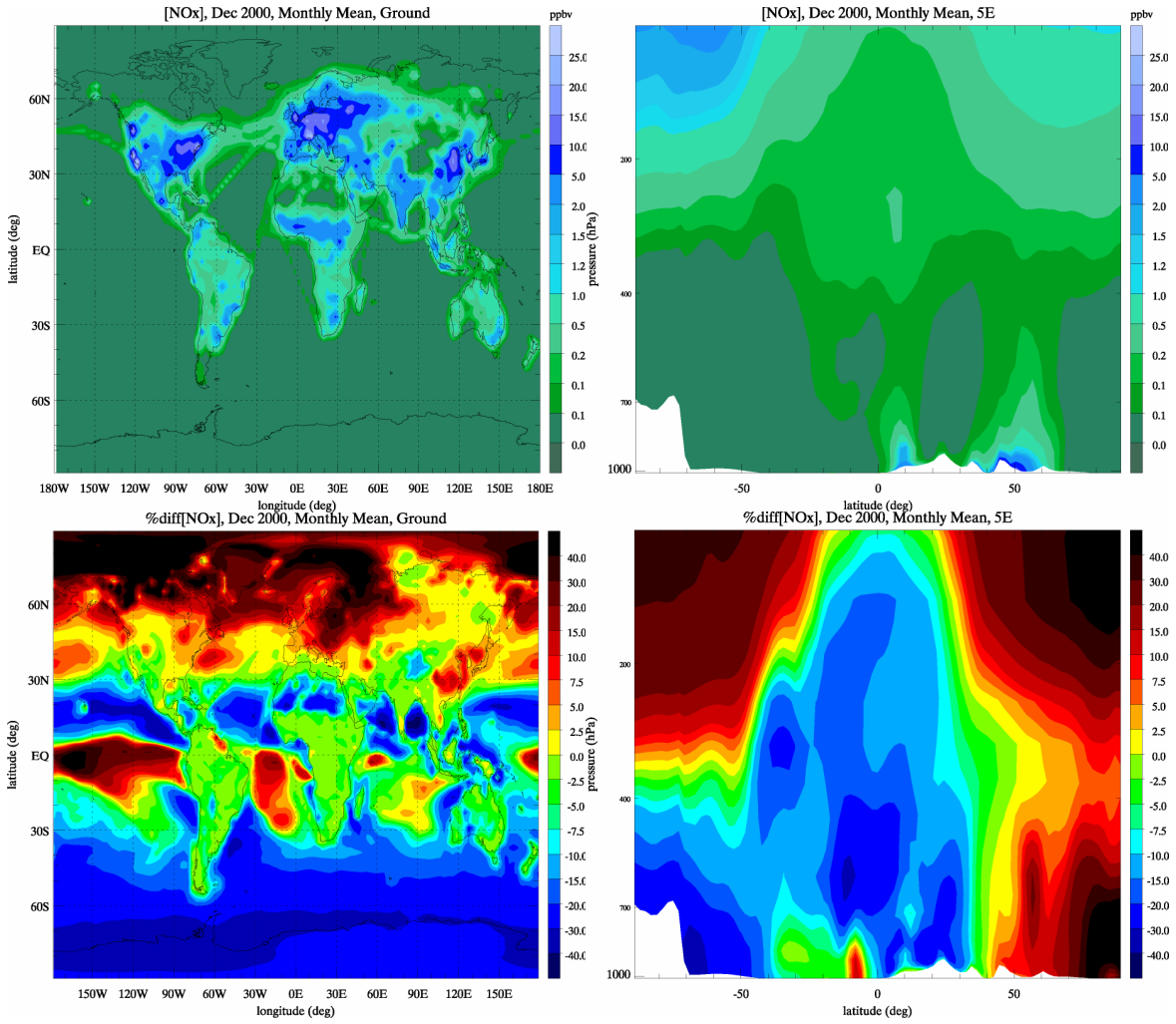

Figure 21: The monthly mean distribution of tropospheric NO_x (= NO + NO_2) for December 2000 as calculated using the updated reaction data (tm4_op_run_mgly) for (a) the ground layer and (b) a longitudinal transect taken at 5°E. The associated percentage differences are shown in (c) and (d), respectively.

The changes in tropospheric [O_3] discussed in the preceding section are, in part, the result of changes in the partitioning and availability of reactive nitrogen oxides, and their associated nitrogen reservoir species. Figures 21a-d show the global distribution of NO_x for the chosen cross-sections, along with the corresponding percentage differences. The maximum concentrations are located near industrial source regions, notably Central Europe, the Eastern U.S. and China. It should be noted that the distribution of NO_x is critically dependent on the emission datasets implemented in the model. Additional NO_x is injected in the upper layers to account for the emissions from aircraft and lightning. The vertical distribution of NO_x is determined by the rate at which it is chemically processed into more long-lived reservoir species in the lower layers, the rate of deposition of these reservoir species to the surface, the additional transport of these long-lived reservoir species by convection/mixing and the subsequent decomposition of these reservoir species to redistribute reactive nitrogen through the atmospheric column. The resulting [NO_x] in TM4 is largest directly above the source regions, becomes quite low in the middle troposphere (between 0-0.2 ppbv) and then increases again above ~300hPa. It can be seen that there is ~10-20% less reactive NO_x throughout the tropospheric column. This is due to the slower release of nitrogen from the reservoir compounds (see below):

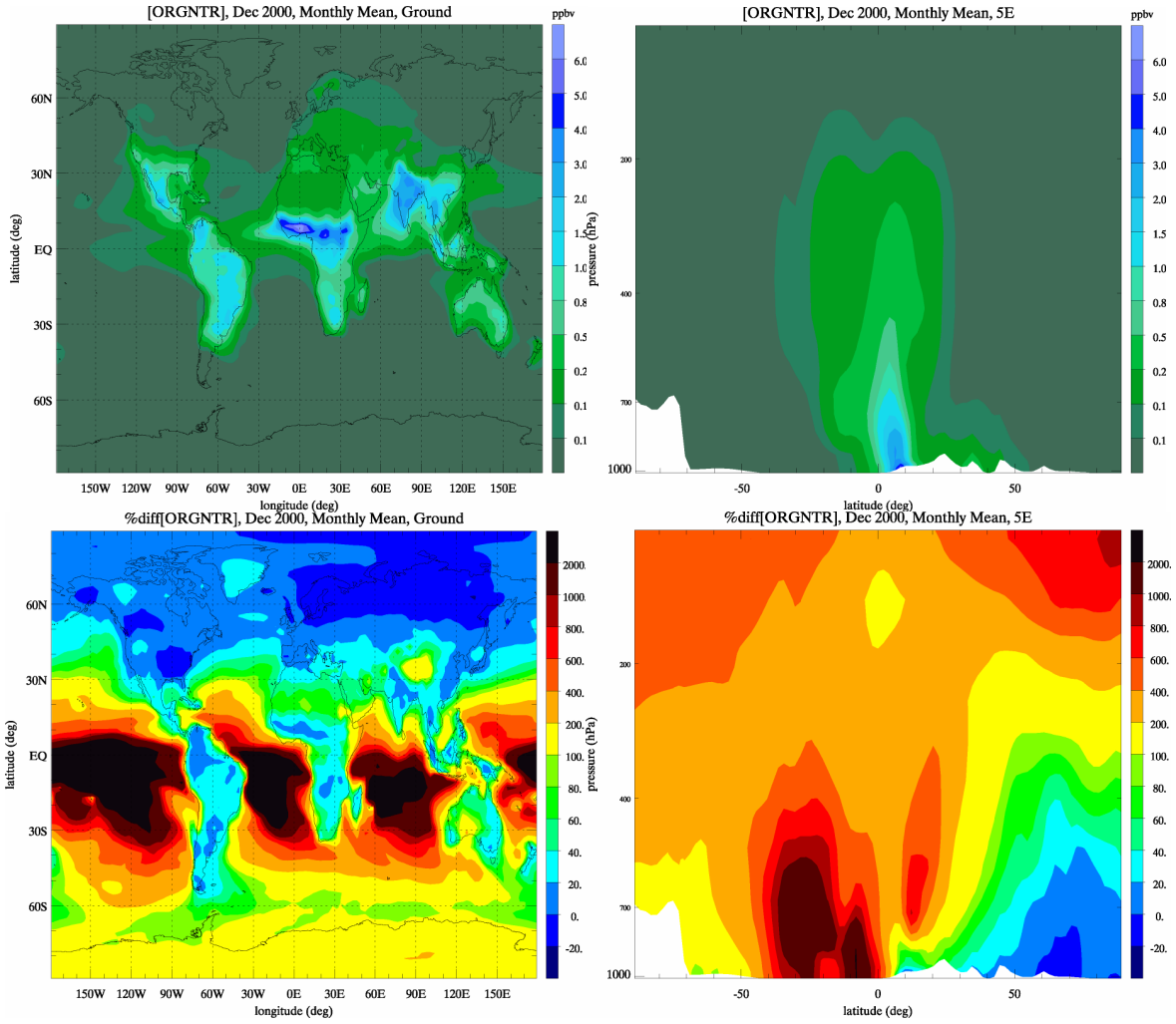

Figure 22: As for Figure 21 except for ORGNTR. The substantial increases which occur over the oceans in the tropics show that the formation and subsequent transport away from the sources regions is much more efficient using the new reaction data.

For the long range transport of NO_x away from the source regions the most important compounds are PAN, ORGNTR and, to a lesser extent, HNO_3. The first two of these NO_x reservoirs are relatively insoluble therefore do not undergo wet deposition, unlike HNO_3, meaning that their convective transport can be quite pronounced. Moreover, both PAN and ORGNTR tend to be predominantly formed near the surface when there is a sufficient source of NMHC and Isoprene,

respectively, whereas HNO_3 can be formed *in-situ* in the upper troposphere by reaction KNO2OH. In the box modelling sensitivity tests a substantial increase in [ORGNTR] occurred across a wide range of scenarios as a result of lowering J_{ORGN} and an increase in the production rate (KC81). However, for the wintertime scenarios (e.g. URW) the increase in $[CH_3C(O)O_2]$ generally resulted an increase in PAN formation (see Section 4). For $[HNO_3]$ there were decreases of ~30%. In general, these effects are amplified when applying the updated mechanism in TM4 except for PAN.

Figures 22a-d show the global distribution of ORGNTR for the chosen cross-sections, along with the corresponding percentage difference. Here it can be seen that at the surface the highest [ORGNTR] occurs near equatorial Africa as expected, considering that the production is governed by the availability of XO_2N, which is most efficiently formed via the oxidation of isoprene (i.e. KC76-78 as shown in Appendix B). Here it should be noted that the high [ISOP] which occurs in the first few layers of TM4 (20-40ppbv, not shown) has the potential to enhance the production of ORGNTR, thus perturbing the partitioning of reaction NO_x. For the more industrial regions the oxidation of PAR by reaction KC52 also acts as an important source of XO_2N. At the surface there are percentage increases in [ORGNTR] of between 0-25% for the NH and 80-200% for the SH. For the outflow regions between 30°N-30°S (e.g. off Western Africa) there are increases of between 500-2000%, although the [ORGNTR] remains below 1ppbv. This finding is in line with the box model studies where reactive nitrogen was bound up quite efficiently by ORGNTR when using the new reaction data for a diverse range of scenarios. These large increases in the outflow regions also correlate with increases in $[O_3]$ of between 5-10% (see Fig. 18) as a result of the additional $[NO_2]$ introduced in remote regions by the slow oxidation of ORGNTR. The most substantial increases in [ORGNTR] occur over the source regions (Equatorial Africa and India), where increases in [ORGNTR] of between 1-1.5ppbv occur.

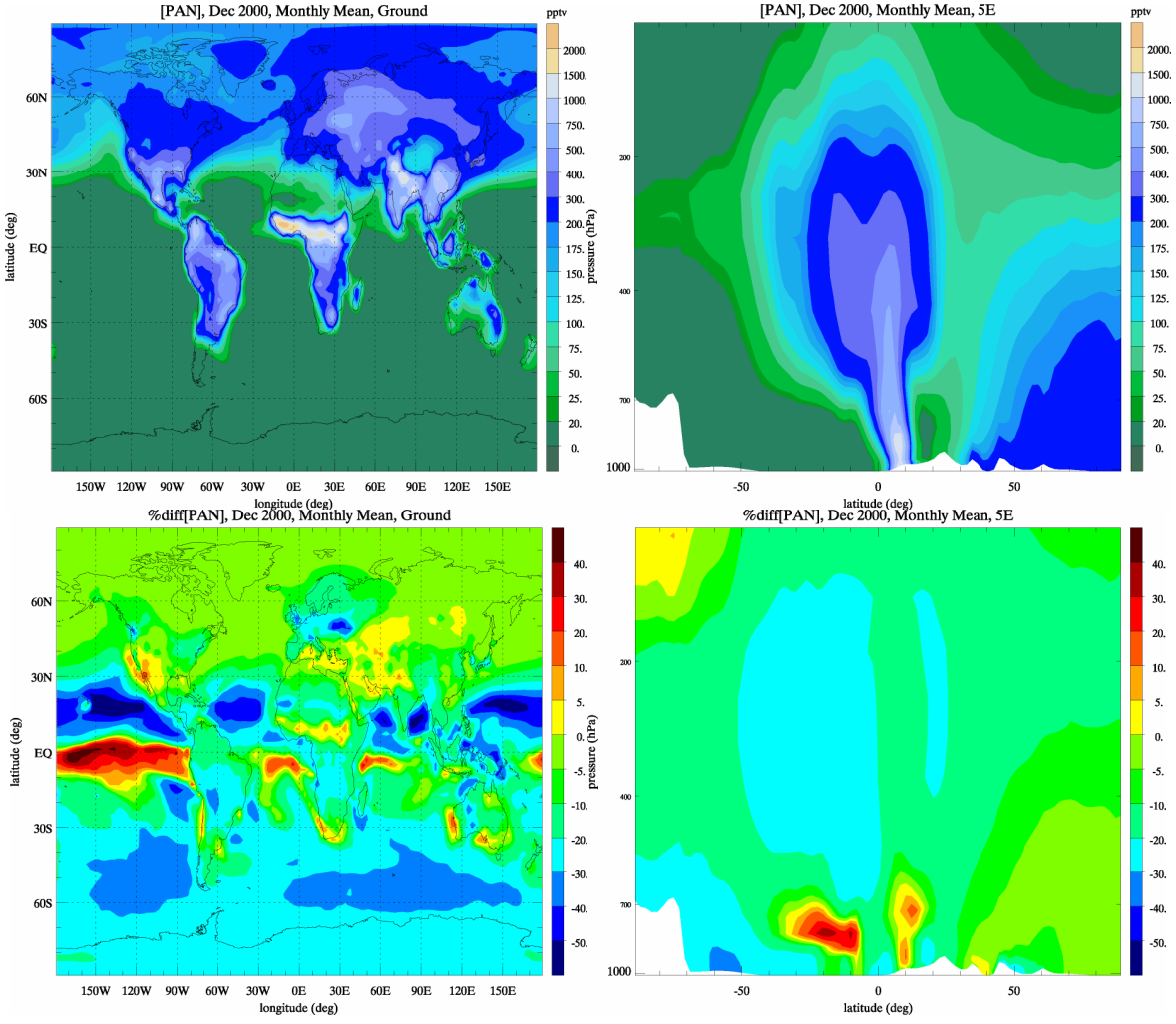

Figure 23: As for Figure 22 except for PAN.

For the tropospheric column the highest [ORGNTR] occurs directly above Equatorial Africa. In general, the percentage differences in [ORGNTR] are similar to those seen at the surface, where there are changes of ±20% in the NH and 100-200% in the SH. The largest increases of between 400-1000% are again associated with rather low [ORGNTR]. However, the amount of reactive nitrogen available through the tropospheric column is reduced as a result as is shown by the percentage differences which occur for both NO_x and O_3 (see Figs. 21d and 20d, respectively).

Figures 23a-d shows the global distribution of PAN similar to that shown for ORGNTR in Figure 22. For the formation of PAN the chemical precursors are NO_2 and $CH_3C(O)O_2$, resulting in strong production for regions influenced by industrial emissions, biogenic emissions (via the oxidation of isoprene) and/or biomass burning activity (see the surface distribution shown in Figure 23a). For December this results in lower [PAN] in the SH as compared to the NH, as shown by the surface distribution. Moreover, the thermal decomposition of PAN is enhanced by the warmer temperatures in the SH for this month. The effect of updating the reaction data is an annual decrease in PAN formation of ~30% in the NH and ~40% in both the tropics and SH as determined from the chemical budgets. This is despite the increases in $[CH_3C(O)O_2]$ which occur as a result of a higher J_{MGLY} (not shown). Therefore, even though the thermal decomposition of PAN becomes slower as a result of the new chemical data (see Appendix F) the formation is hindered by the reduced availability of NO_2. For the more remote regions there are associated decreases in [PAN] of ~5% in the NH and ~20-30% in the SH due a reduction in the amount being transported away from the source regions. In the box-modelling studies [PAN] remained fairly constant over a range of different scenarios, which is somewhat different to the findings presented here. Moreover, for the urban scenarios the box-modelling studies also predicted an increase in [PAN] of ~10% for regions influenced by anthropogenic activity.

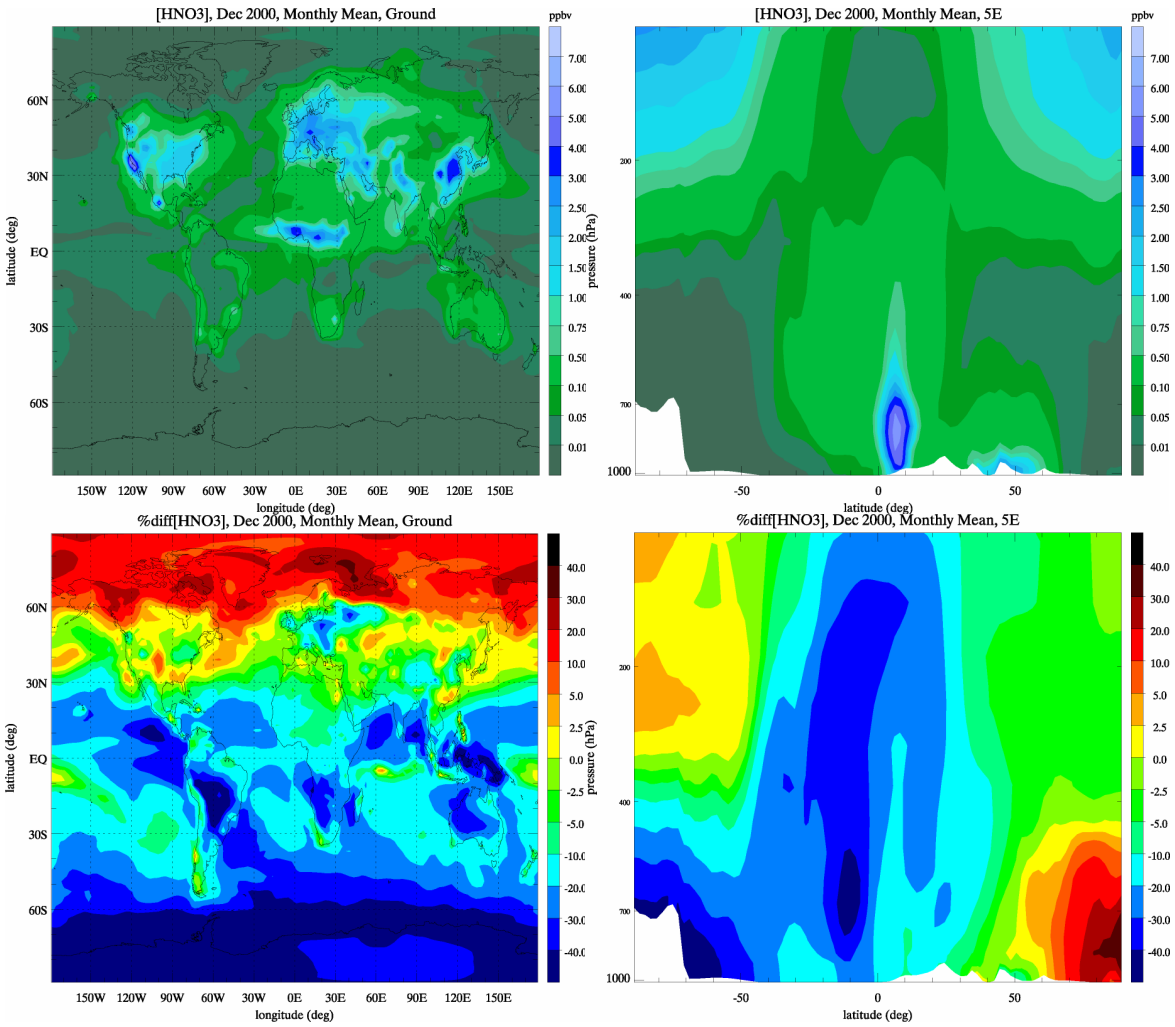

Figure 24: As for Figure 22 except for HNO_3.

For the vertical distribution of [PAN] there are generally decreases throughout the troposphere. Comparing Figures 22d and 23d reveals that the fraction of NO_2 transported as ORGNTR exceeds that of PAN above the tropics. One contributing factor is that ORGNTR is not represented as an equilibrium reaction in the modified CBM4 mechanism therefore destruction is limited to J_{ORGN} and the reaction with OH (KC84). Analysis of the chemical budgets shows that the net destruction of [ORGNTR] by KC84 remains fairly constant. Therefore, the increase in the resident [ORGNTR] offsets the decrease in KC84 of ~90% (see Appendix F). Therefore the reduction in J_{ORGN} essentially hinders the release of NO_2. A further point is that these results indicate that ORGNTR is as important for transporting reactive nitrogen away from the tropics to the upper troposphere as PAN when using the modified CBM4 mechanism with the updated reaction data.

The final nitrogen reservoir species to consider is HNO_3. Figures 24a-d show identical plots for HNO_3 as those provided above for PAN and ORGNTR. At the surface the highest [HNO_3] occur for those regions where there are significant NO_x emissions such as China, Europe and the US (see Figure 24a). The resulting percentage differences depend somewhat on the region. In general there are decreases of between 10-40% for December over the more industrial regions in the NH related to the decreases in both [NO_2] and [OH] (see next section). This finding is in line with the conclusions of the box modeling study, where decreases in [HNO_3] occurred in polluted scenarios (URS, Figure 14) as a consequence of the enhanced formation and increased atmospheric lifetime of ORGNTR. Integrating this effect globally over the entire year reveals that ~20% less [HNO_3] is formed via KNO2OH. However, a more important term for the global production of HNO_3 is the oxidation of ALD2 in the tropics by the NO_3 radical, which produces three times the amount when integrated over the entire year. Although the rate of KC44 increases by ~80%, this is negated by reduction in the [NO_3] radical as simulated in the box model studies.

The typical range of values for [HNO_3] which have been measured at the surface can fluctuate significantly over the period of a few days (e.g. Hanke et al., 2003). However, monthly means should be of the order of a 10-30 pptv for background locations (e.g. Huey et al., 2004) and 5-10 ppbv for polluted regions (e.g. Peng et al., 2006) during winter. This indicates that the [HNO_3] surface field simulated in the tm4_op_run_mgly simulation exhibits a distribution that is of the right order of magnitude, although proper validation is needed for the entire year if possible.

The distribution of HNO_3 throughout the tropospheric column is shown in Figure 24b. The maximum concentrations occur directly above the source regions as a result of convective transport of pre-cursors and subsequent *in-situ* production at the higher altitudes. In general, there are decreases in [HNO_3] of upto 40% up to a pressure level of ~200hPa. The remaining differences are introduced by a decrease in the *in-situ* production efficiency of HNO_3 as a result of the availability of NO_2. This reduces the amount of nitrogen lost through wet deposition by ~18% when integrated over the entire year for all regions.

A special case concerns the fate of N_2O_5, which acts as an intermediate species that can be scavenged by both cloud droplets and aqueous aerosols. Here we adopt the γ_{N2O5} value from Evans and Jacob (2005), who found that reducing this value in a CTM leads to increases in both [O_3] and [NO_x]. In addition to this effect, updating the reaction data can alter the formation efficiency by perturbing both NO_2 and NO_3. Analysing the chemical budgets reveals that, in terms of the total mass of nitrogen lost, a ~15%, reduction occurs via heterogeneous scavenging as a result of updating the new reaction data due to lower [N_2O_5], in line with the findings of the box model studies.

5.2.3 HCHO and HOx

Although the increases in both J_{aCH2O} and J_{bCH2O} have yet to be implemented in the TM model, one of the main conclusions of the box modelling studies was that [HCHO] increases of the order of 10-20% should occur as a result of updating the reaction data (see Figure 13 presented in Section 4). Moreover, HCHO acts as an important source of HO_x in remote areas meaning that any changes in [HCHO] has the ability to influence the lifetime of important greenhouse gases such as CH_4. Therefore we show the resulting changes in [HCHO] which occur in the TM model to investigate whether this finding pertains to CTM simulations.

Figures 25a-d show the global distribution of HCHO for the chosen cross-sections, along with the corresponding percentage differences. The highest concentrations occur near the regions dominated by biomass burning activity and biogenic emissions. A consequence of the high [ISOP] at the surface is that a large fraction of the total HCHO is formed via the oxidation of isoprene (reactions KC76 and KC77). However, there are generally decreases in [HCHO] of between 5-20% near regions where the highest concentrations occur (e.g. Equatorial Africa) and between 50-100% near industrial regions. For the vertical distribution of HCHO the resulting percentage changes are shown in Figure 25d. It can be seen that as altitude increases the resident [HCHO] becomes smaller meaning that it is predominantly formed near the surface

and subsequently transported upwards. Again, the percentage differences in the lower troposphere are similar to those shown at the surface. As a result there is ~12% less wet deposition of HCHO when globally integrated over the entire year. The differences shown in Figure 25 suggests that using the new reaction data could have a substantial impact on the retrieval of HCHO from (e.g.) GOME, which is critically dependent on the tropospheric distribution of HCHO.

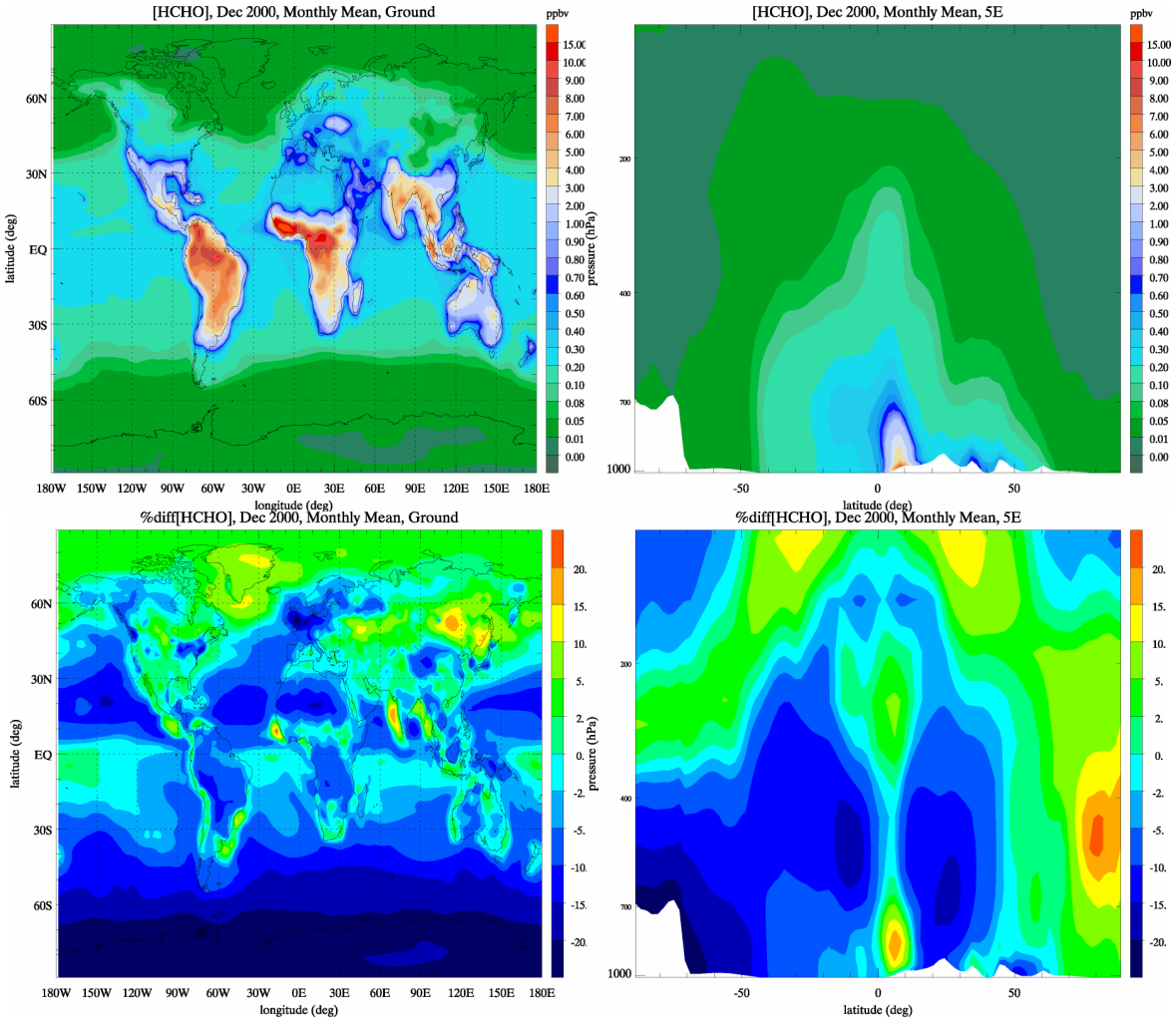

Figure 25: The monthly mean distribution of HCHO for December 2000 as calculated using the updated reaction data (tm4_op_run_mgly) for (a) the ground layer and (b) a longitudinal transect taken at 5°E. The associated percentage differences are shown in (c) and (d), respectively.

The associated changes in both OH and HO_2 at the surface are shown in Figures 26a and b, respectively. In general there are decreases in both [OH] and [HO_2] of ~10%, with larger decreases near regions influenced by high industrial emissions in line with the results of the box model studies. This perturbation in [OH] also increases the lifetime of both CO and CH_4 by reducing the rate of oxidation (see section 5.3). The reaction KCOOH acts as the predominant source of [HO_2] in the atmosphere (Tan et al., 2001) resulting in decreases in both [CH_3OOH] and [H_2O_2] of between 0-20% (not shown), which themselves act as sources of HO_x radicals. For instance, the amount of [OH] formed via the photolysis of H_2O_2 falls by ~10% when integrated globally for all regions. For the vertical distribution there are also decreases in [OH] throughout the lower troposphere. Analysing the chemical budgets reveals that ~8.5% less [OH] is formed via KH2OOD, resulting ina lower oxidising capacity for the troposphere. There are similar differences of ±5% for [HO_2] throughout the column. This results in a decrease in the wet deposition of H_2O_2 of ~13% when integrated over the entire year for all regions. The chemical conversion of OH to HO_2 controls the HO_x ratio, which changes as a result of updating the chemical rates as discussed in Section 5.3

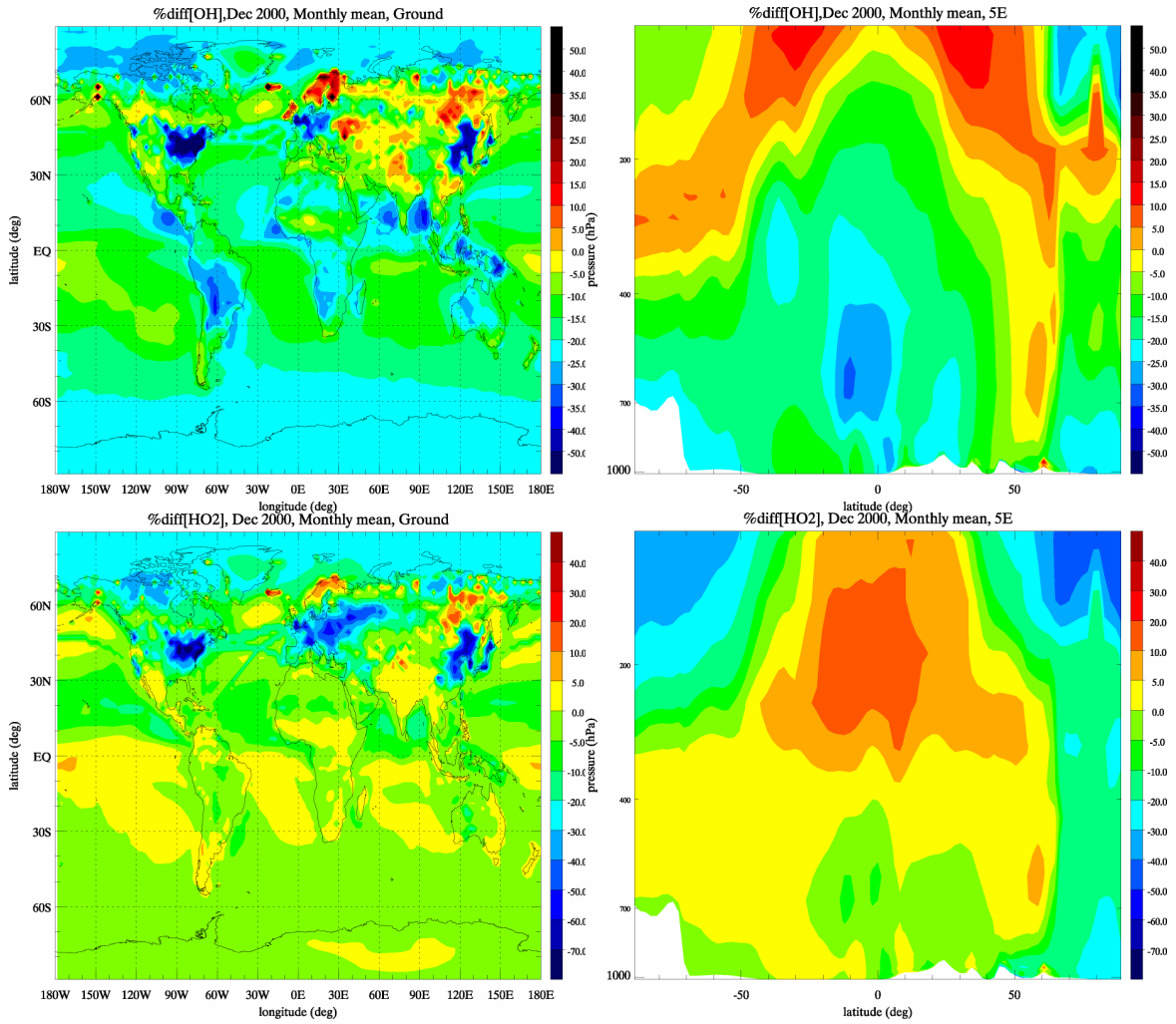

Figure 26: The differences introduced for (a) [OH] and (b) [HO_2] as a result of updating the modified CBM4 mechanism. It can be seen that the largest decreases in [OH] and [HO_2] occur over regions that exhibit the highest [NO_x] emissions for this season.

5.5 Tropospheric CO

One of the most important reactions involved in determining the lifetime of atmospheric greenhouse gases is the reaction of OH with CO, which contributes to determining the atmospheric lifetime of CH_4 by scavenging a significant fraction of the available OH. In Appendix F it can be seen that the recent update of KCOOH results in a modest decrease of a few percent in the rate constant at STP. The box-model studies have shown the in-situ production of CO also increases as a result of updating the reaction data. The integrated effect should be most noticeable for [CO] in the Southern Hemisphere, which is relatively unaffected by direct CO emissions.

Figures 27a-d show the global distribution of CO for the chosen cross-sections, along with the corresponding percentage differences. For the vertical distribution the highest [CO] is found directly above regions that have the strongest CO emission sources for this month, especially in the tropics. The largest percentage increases at the surface are seen in the SH, where increases of ~14% occur in the monthly mean. Near the source regions there are more modest increases of between 3-5% (e.g. Europe and China), although these are associated with much higher [CO] levels. This typically equates to an additional ~10ppbv for the SH, ~8ppbv for regions such as Europe the Eastern U.S. and the NH and ~20ppbv over Equatorial Africa. These findings agree with the main conclusions of the box modelling study presented in Section 4.

Comparisons of TM4 fields with CO columns retrieved from SCIAMACHY for the year 2004 have shown that the seasonal cycle at selected locations correlates quite well (de Laat et al., 2007). However, considering the background [CO] shown in

Figure 26a suggests that the agreement between these total columns and the simulations discussed here could degrade, although refinements to the retrieval process are currently ongoing (e.g. Gloudemans et al., 2008).

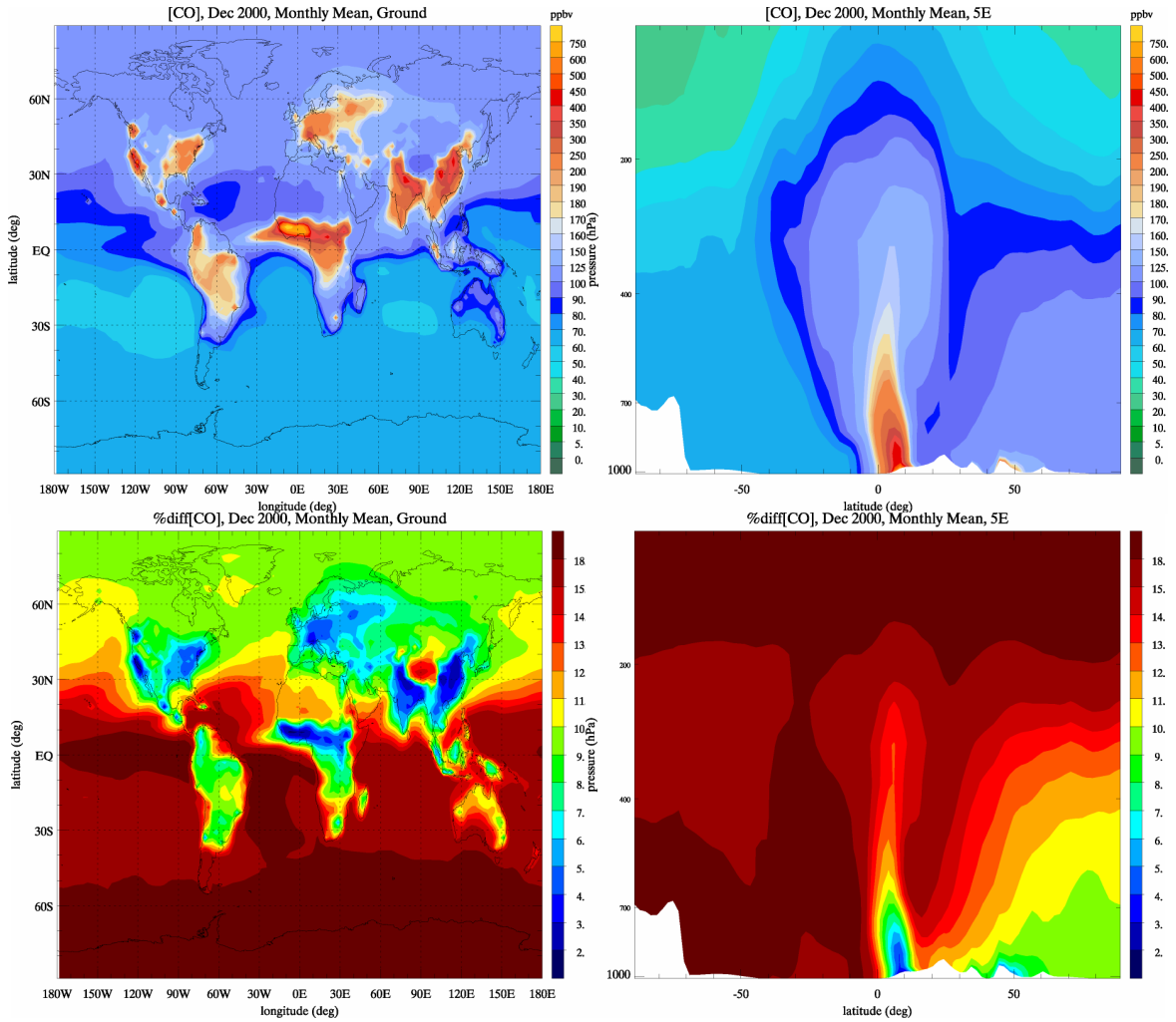

Figure 27: The monthly mean distribution of CO for December 2000 as calculated using the updated reaction data (tm4_op_run_mgly) for (a) the ground layer and (b) a longitudinal transect taken at 5°E. The associated percentage differences are shown in (c) and (d), respectively.

In Appendix I we expand on this and present comparisons between CO measured at a selection of CMDL surface sites with co-located output from the tm4_baseline_run and the tm4_op_run_mgly. The seasonal cycle in [CO] observed in the measurements is captured at many of the locations, which gives confidence regarding the timing of the release of the emissions and the subsequent transport away from the source regions. For the high latitudes sites TM4 simulates [CO] which is low by ~50% for the first 6 months of the year across a wide range of longitudes both with and without the new chemical rates (Fig. I1). In the SH an overestimation exists for the entire year, although the application of the reduced grid makes comparison difficult. This is the so-called NH bias described in the multi-model intercomparison of Shindell et al. (2006) concerning CO comparisons, who attributed this to an under estimation in emissions from East Asia. For the mid-latitude sites the agreement is better but more variable from station to station (e.g.) for Tenerife (IZO) and Bermuda (BME) agreement is good, whereas for Cape Grim (CGO) and Tae Ahn (TDF) there is an over estimation. In all instances the surface [CO] is higher when using the updated chemical rates, resulting in a better correlation with the CMDL measurements. Finally for the tropical stations the agreement is again variable, with the agreement being good for Guam (GMI) and the Seychelles (SEY), and under predictions occurring for (e.g.) Assekrem (ASK) and Mount Loa (MLO). Again a bias occurs for the first half of the year that is most likely related to the bias seen at the high latitude sites. Therefore, although the updated chemistry improves agreement issues still exist for a large subset of the stations.

5.3 Budget Analysis concerning the Atmospheric Lifetimes of CH_4 and O_3

In this final section we analyze the differences concerning $\tau(CH_4)$, the tropospheric lifetime of O_3 (hereafter denoted as $\tau(O_3)$), the tropospheric burdens of both O_3 and CO (hereafter denoted as BO_3 and BCO), changes in the scavenging efficiency for [OH] between the different sensitivity runs and the effect of introducing a diurnal emission flux for isoprene. We also provide an analysis for simulations performed using the Royal Society emission dataset to investigate the robustness of the changes when using more up-to-date emission estimates. For the analysis we use some of the diagnostics defined in the multi-model intercomparison of Stevenson et al. (2006) and define the troposphere as all grid cells which contain $[O_3] < 150$ppbv in the monthly means according to the standard definition used in previous IPCC assessments (Prather and Ehhalt, 2001). All budgets are calculated by integrating the global changes in the reaction fluxes of the entire year.

Definition of run	Tropospheric destruction of CH_4 ($Tg\ yr^{-1}$)	τ_{CH_4} (years)	Atmospheric Chemical Lifetime (years)
Previous value	497.1	8.80	-
tm4_baseline_run	575.6	7.73	8.67
tm4_baseline_mgly	574.9	7.74	8.69
tm4_op_run	483.7	9.02	10.33
tm4_op_run_mgly	468.4	9.27	10.67
tm4_GFED2000_ch4grad	447.1	9.40	10.87
tm4_baseline_rs	594.5	7.51	8.40
tm4_op_run_rs	502.6	8.73	9.94

Table 4: Details concerning the changes in the annual tropospheric destruction rate of CH_4 (via KCH4OH), the atmospheric lifetime of CH_4 and the atmospheric chemical lifetime of CH_4 for all four sensitivity studies. For the calculation of τ_{CH_4} a soil sink of 30 $Tg\ yr^{-1}$ and stratospheric sink of 40 $Tg\ yr^{-1}$ is included as given in Prather and Ehhalt (2001). The atmospheric chemical lifetime is calculated using the total destruction of CH_4 in the troposphere. The multi-model ensemble average for $\tau(CH_4)$ given in Stevenson et al. (2006) is 8.67±1.32 years.

Table 4 provides information concerning the integrated tropospheric destruction of CH_4 via KOHCH4, $\tau(CH_4)$ and also the atmospheric chemical lifetime of CH_4. For the tm4_baseline_run the $\tau(CH_4)$ decreases by ~12% to ~7.7 years primarily as a result of correcting the summation of the total ozone column, which increases J_{O3d} by ~18% and J_{NO2} by ~2%. The agreement with the multi-model ensemble average given in Stevenson et al (2006) subsequently decreases (see footnote of Table 4), although this value is still within the 1-σ variability. Comparing the results given for the tm4_baseline_mgly run indicates that introducing the transport of $CH_3C(O)CHO$ into the model only has a minimal effect on $\tau(CH_4)$. This is due to the regional perturbations in $[HO_x]$ being limited when keeping J_{MGLY} fixed. When using the updated chemical reaction data $\tau(CH_4)$ increases by ~17% as compared with the tm4_baseline_run as a result of the reduction in [OH] (see Figure 26). Introducing the transport of $CH_3C(O)CHO$ results in a further increase in $\tau(CH_4)$ of ~3% as compared with the tm4_baseline run. Thus, the effect of transporting $CH_3C(O)CHO$ is enhanced when used in conjunction the new chemical rates, due to the increase in J_{MGLY}. Again, the resulting $\tau(CH_4)$ values still fall within the 1-σ variability of the multi-model mean. Taking the differences with the multi-model ensemble mean shows that although the chemically activity of the model decreases as a result of updating the reaction data, the difference is reduced by 0.37 years compared to multi-model ensemble mean. Therefore, the oxidizing capacity of the troposphere decreases as a result of updating the reaction data. For the simulation performed using the specific GFEDv1 emission dataset for 2000, the $\tau(CH_4)$ increases by a further 0.13 years mainly due to the increased scavenging of OH by the ~9% increase in the CO emission flux. For the simulations using the Royal Society emission dataset there is a difference of ~15% between a baseline run and the run using the new chemical rates. Therefore, the extent to which perturbations in $[HO_x]$ occur do seem to be somewhat dependent on the emission scenarios which are adopted in the model, most probably due to the change in the O_3 production terms that are dependent on global NO_x emissions (Wild, 2007).

Definition of run	Chemical O_3 Production ($Tg\ O_3\ yr^{-1}$)	Chemical O_3 Loss ($Tg\ O_3\ yr^{-1}$)	Dry Deposition ($Tg\ O_3\ yr^{-1}$)	Strat-Trop Exchange ($Tg\ O_3\ yr^{-1}$)	τ_{O_3} (days)
Previous value	4806	4594	720	508	23.6
tm4_baseline_run	5119	4958	683	527	20.7
tm4_baseline_mgly	5119	4958	683	527	20.7
tm4_op_run	4514	4363	675	530	23.2
tm4_op_run_mgly	4506	4354	679	526	23.3
tm4_GFED2000_ch4grad	4259	4134	651	532	23.8
tm4_baseline_rs	5232	5053	702	527	20.5
tm4_op_run_rs	4622	4453	696	531	22.9

Table 5: The changes associated with the chemical production, chemical loss, dry deposition, Stratosphere-Troposphere Exchange and tropospheric lifetime for tropospheric ozone as a result of updating the chemical reaction data. Results are given all the four of the sensitivity studies. The multi-model ensemble means are $4974\pm233\ Tg\ O_3\ yr^{-1}$, $4577\pm291\ Tg\ O_3\ yr^{-1}$, $953\pm154\ Tg\ O_3\ yr^{-1}$, $556\pm154\ Tg\ O_3\ yr^{-1}$ and 22.2 ± 2.22 days, respectively.

Definition of run	BO_3 (Tg)	BCO (Tg)	τ_{CO} (months)
Original run	344	-	-
tm4_baseline_run	320	305	~1.7
tm4_baseline_mgly	320	306	~1.7
tm4_op_run	319	338	~2.0
tm4_op_run_mgly	320	348	~2.0
tm4_GFED2000_ch4grad	311	348	~2.1
tm4_baseline_rs	322	305	~2.2
tm4_op_run_rs	322	335	~2.1

Table 6: The changes associated with the burdens of tropospheric O_3 and tropospheric CO for all four sensitivity studies. The multi-model ensemble mean for BO_3 is 336 ± 27 Tg.

Table 5 provides information concerning the tropospheric ozone budget in terms of the integrated chemical O_3 production, integrated chemical O_3 loss, the loss by dry deposition, the magnitude of the stratosphere-troposphere exchange and $\tau(O_3)$ for all runs listed in Table 4. The values for the multi-model ensemble average for each of these diagnostics as given in Stevenson et al. (2006) are provided in the footnote of the table. Comparing these values reveals that the effect of the bug fixes is an increase in the chemical activity of the model, where both the production and destruction terms increase, causing $\tau(O_3)$ to decrease by ~10%. This reduces the potential of long-range transport of O_3 away from the source regions. Moreover, the chemical loss subsequently lies outside the 1-σ variability of the multi-model ensemble values. The difference between the production and loss terms is reduced which lowers the tropospheric burden of O_3 (see below). For the simulations that use the new reaction data this increase in chemical activity is subsequently dampened. Here the chemical production moves outside the 1-σ variability whilst the chemical loss recovers. This is primarily due to the increased scavenging of NO_2 as discussed in Section 5.3. For the Royal Society emission dataset the chemical activity of the model increases as would be expected considering the net increase in the global NO_x emission. Again the application of the new reaction data dampens this chemical activity thus increasing $\tau(O_3)$.

The tropospheric burden of any trace gas maybe defined as the integrated mass of a particular trace species contained in the troposphere. The values of BO_3 and BCO calculated for all sensitivity runs are provided in Table 6. Comparing these values shows that the total $[O_3]$ decreases when applying the bug fixes, but remains relatively unaffected when using the new reaction data despite the changes in both the chemical production and loss terms. For the Royal Society runs the burden increases in line with the increased emissions of important pre-cursors. For BCO there is a significant increase of ~10% when using the new reaction data as a result of the slower removal as a result of a decrease in KCOOH and the lower resident [OH].

Next we present the differences introduced with respect to the main loss reactions of the OH radical. Table 7 lists those reactions that scavenge more than 1% of the total available [OH]. The most efficient scavenging term in all simulations is the reaction with CO. Although the rate of oxidation of CO decreases (see increase in BCO above) the amount of available

[OH] scavenged by CO increases by ~2%. The lower oxidation rate means that the conversion of OH to HO_2 is subsequently reduced, which nullifies any increase in [HO_2] due to the increase in J_{MGLY}. Moreover, the globally integrated conversion of OH to HO_2 via KFRMOH, KHPOH and KH2OH also decreases by −50%, -28% and −25%, respectively. This alters the [OH]:[HO_2] ratio where values get lower, apart from in the upper troposphere for altitudes which exhibit increases in [OH] (see Figure 26). For the reaction with peroxides the percentage loss of [OH] is scaled down to account for the OH that is formed as a product (see Appendix B).

Reaction	Previous value	tm4_baseline run	tm4_op_run	tm4_baseline_rs	tm4_op_run_rs
OH + CH_4	16.0	16.7	15.8	20.3	16.2
OH + CO	42.5	40.4	42.8	42.5	43.2
OH + HCHO	7.0	7.4	5.8	6.0	6.0
OH + CH3OOH(*)	4.4	4.8	4.5	5.2	4.5
OH + ROOH(*)	2.3	2.5	2.5	2.0	2.3
OH + H_2	5.3	5.5	5.2	4.0	5.3
OH + HO_2	4.9	5.4	5.2	4.4	5.3
OH + H_2O_2	3.5	3.8	3.5	3.2	3.6
OH + ISOP	4.0	3.8	4.3	3.4	3.8
OH + OLE	2.6	2.4	2.9	2.3	2.6
OH + ALD2	3.1	2.9	3.2	2.7	3.0
OH + PAR	2.0	2.3	2.6	2.4	2.6
OH + ORGNTR	0.3	0.4	0.1	0.1	0.1

Table 7: The dominant loss processes for tropospheric [OH] as derived from chemical budgets produced during the simulations. For CH3OOH and ROOH the percentage loss is scaled to take account of the fractional OH produced in the reaction (see Appendix B).

Reaction	Previous value (Tg/yr-1)	tm4_baseline_run (Tg/yr-1)	tm4_op_run_mgly (Tg/yr-1)	tm4_GFED2000 ch4grad (Tg/yr-1)
OH + ISOP	388.8 (0.71)	423.5 (0.75)	409.1 (0.74)	431.1 (0.79)
O3 + ISOP	133.6 (0.24)	115.2 (0.21)	119.5(0.22)	99.2 (0.18)
NO3 + ISOP	27.7 (0.05)	25.2 (0.04)	24.1(0.04)	14.4 (0.03)

Table 8: Changes in isoprene oxidation as a result of updating the reaction data and imposing a diurnal cycle on the emission flux. The total emission flux is 630Tg yr-1 in all of the sensitivity runs. The fraction lost by each oxidation pathway is given in red. The total mass of isoprene oxidized in each run is : 553 Tg yr^{-1}, 563.9 Tg yr^{-1}, 552.7 Tg yr^{-1} and 554.7 Tg yr^{-1}, respectively.

Finally we examine the influence of introducing a diurnal variation on the oxidation of isoprene. This was motivated by the high [ISOP] which occurs in the lower layers of the model when assuming that the emission only occurs in the lowest 50m. Table 8 provides details related to the total mass of isoprene oxidized by OH, O_3 and NO_3, as integrated globally over the entire year. The predominant oxidation pathway in all runs is that by OH. Updating the chemical reaction data lowers the total amount of isoprene oxidized per year and results in a larger fraction being oxidized by O_3 (see footnote of Table 8). Introducing the diurnal variation results in more isoprene being oxidized by OH as a result of the peak in isoprene emissions occurring when there is maximal daily [OH]. This subsequently reduces the loss of O3 by KC77 by ~15%. The product distribution is subsequently altered according to the Stiochiometry of each of the reactions (see Appendix B). Although the representation of isoprene oxidation is rather crude in the modified CBM4 mechanism the result indicates that the diurnal cycle should be implemented as a default into TM4.

6. Conclusions and Recommendations

In this study we have shown that updating the modified CBM4 mechanism with the latest recommendations for the chemical reaction data has a significant effect on the resident concentrations of important trace gas species such as tropospheric O_3 and CO. A box model sensitivity study was conducted which concluded that differences in the scaling ratios adopted for the calculation of the photolysis of $CH_3C(O)CHO$ result in differences in the performance of the modified CBM4 mechanism for urban scenarios between TM4 and TM5. The most significant effects were found to occur for urban (polluted) scenarios throughout all seasons. In summary, the most important updates were: (i) a retuning of the photolysis rate for $CH_3C(O)CHO$, (ii) the ~30% increase in the photo-dissociation rate of formaldehyde (HCHO), (iii) changes to the reaction rates involving organic peroxy-radicals and (iv) an enhanced formation of ORGNTR. Applying these updates resulted in a decrease in the availability of reactive nitrogen which subsequently influences the production efficiency of ozone. When incorporating an operational set of these updates into the 3D global CTM TM4 it was found that both increasing the J_{MGLY} value and introducing tracer transport for $CH_3C(O)CHO$ significantly reduced the surface concentrations over industrial regions by up to 80%. For the other trace gases there were generally decreases in tropospheric [OH], [HO_2], [O_3], [PAN], [HNO_3] and [HCHO], with associated increases in [ORGNTR] and [CO]. In general, the oxidising capacity in the model atmosphere decreases as a result of the lower global production rate of OH. Comparisons made against selected ozonesonde profiles shows that TM4 generally over predicts surface ozone in the tropics whilst underestimating surface ozone in remote locations. For the upper troposphere TM4 generally under predicts tropospheric ozone indicating that the transport and/or release of reactive nitrogen is insufficient. For surface CO there are generally improvements in the correlation between values simulated in TM4 and a host of CMDL measurement sites. The atmospheric lifetimes of both CH_4 and O_3 become ~9.3 years and 23.6 days, respectively, where both these values are in the 1-σ variability of the multi-model ensemble mean given in Stevenson et al (2006) for the IPCC 2000 simulations.

The recommendations that can be made to the chemical component of the TM model as a result of this study are summarised below:

(i) Methylgloxal ($CH_3C(O)CHO$), which has an atmospheric lifetime of ~5 hours, should be included as a transported tracer species. This prevents the accumulation of large concentrations in the lowest model layer as a result of using the emission of $CH_3C(O)CHO$ as a surrogate for (e.g.) xylene.

(ii) The scaling factor used for the calculation of J_{MGLY} should be changed to $5.5*J_{bCH2O}$ in order to bring the J_{MGLY} value in line with explicit calculations.

(iii) The scaling factor of 2.5 should be removed from the calculation of J_{ORGN} in order to increase the long range transport of organic nitrates (and thus NOx).

(iv) The diurnal emission of isoprene should be included to avoid the removal of too much ozone during the night.

(v) The updated chemical reaction data should be incorporated as given in Appendix F.

It should be noted that adopting recommendations (ii) and (iii) would bring the modified CBM4 scheme used online back in line with the original study of Houweling et al. (1998).

A further set of recommendations are now given which refer to changes which can be made in the longer term in order to further improve the TM model.

(i) The implementation of an online photolysis scheme avoiding the use of look-up tables for the derivation of height resolved actinic flux. This would allow important updates to (e.g.) the photolysis of HCHO to be implemented into TM.

(ii) The introduction of a more advanced chemical scheme based on the CB05 mechanism (Yarwood et al., 2005b). Comparisons against smog chamber data have shown that CB05 performs better for (e.g.) HCHO compared to CBM4. It includes updates to the oxidation of isoprene, updates the product distribution for 14 of the reactions included in the modified CBM4 mechanism and introduces organic products into the description of the oxidation of ORGNTR and ROOH. It is estimated that this upgrade would need the inclusion of 7 extra transported tracer species aimed at providing a better description of the NMHC chemistry.

Further validation of the updated mechanism is ongoing for more recent years as part of the SCOUT-O3, HYMN and AMMA projects during 2008-2009.

Appendix A

Chemical Species

In Table A we list the chemical species which were included in the chemical box model. These essentially mimic the species declared in the TM model. Due to the nature of the modified CBM4 mechanism (Houweling et al., 1998) some of the organic species relate to lumped aggregates, which are further defined in the footnotes at the bottom of the table.

Chemical Species	Chemical Species	Chemical Species
O_3	ROOH [4]	NO_2
NO_x	ORGNTR [5]	NO_3
H_2O_2	ISOP	N_2O_5
CH_4	SO_2	HNO_4
CO	DMS	CH_3COCHO
HNO_3	NH_3	C_2O_3
CH_3OOH	SO_4	ROR [6]
HCHO	NH_4	RXPAR [7]
PAR[1]	MSA	XO_2[8]
C_2H_4	NO	XO_2N [9]
OLE [2]	HO_2	NH_2
ALD2 [3]	CH_3O_2	
PAN	OH	

Table A: The nomenclature for the chemical species included in the box model. The definitions of the lumped species are: [1] paraffinic carbon bonds, [2] olefinic carbon bond, [3] CH_3CHO and higher aldehydes, [4] higher organic peroxides, [5] alkyl nitrates, [6] organic ethers, [7] PAR budget corrector, [8] NO to NO2 operator, [9] NO to alkyl nitrate operator. These definitions are taken from Houweling et al. (1998).

Appendix B

Reaction Rates

In Table B below we provide details related to the input data used for the calculation of the chemical reaction rates in the TM model. The details given are: the name of the reaction rate, the stoichiometry of the reaction, the magnitude of the rates at standard temperature and pressure (298K and 1013hpa) and the source of the input parameters used for calculating the rates. It should be noted that we provide the reference for the last JPL recommendation for which the specific rate parameters were valid rather than the original reference as given in Houweling et al., (1998). This version of the modified CBM4 mechanism and the corresponding rate constants were used for the contributions to the fourth assessment of the IPCC made by both TM4 and TM5, as well as the many intercomparison papers subsequently published (*e.g.* Stevenson et al., 2006).

Reaction name	Stiochiometry of reaction	$K_{298k,1atm}$ Molecules cm^3 s^{-1}	Reference
KNOO3	$NO + O_3 \rightarrow NO_2$	1.82×10^{-14}	DeMore et al. (1997)
KHO2NO	$NO + HO_2 \rightarrow NO_2 + OH$	8.56×10^{-12}	DeMore et al. (1994)
KMO2NO	$NO + CH_3O_2 \rightarrow HCHO + HO_2 + NO_2$	7.68×10^{-12}	Sander et al. (2000)
KNO2OH	$NO_2 + OH (+ M) \rightarrow HNO_3$	8.26×10^{-12}	Not Known
KOHHNO3	$OH + HNO_3 \rightarrow NO_3$	1.55×10^{-13}	Sander et al. (2006)
KNO2O3	$NO_2 + O_3 \rightarrow NO_3$	3.23×10^{-17}	Sander et al. (2006)
KNONO3	$NO + NO_3 \rightarrow NO_2 + NO_2$	2.65×10^{-11}	Sander et al. (2006)
KNO2NO3	$NO_2 + NO_3 \rightarrow N_2O_5$	1.27×10^{-12}	Sander et al. (2000)
KN2O5	$N_2O_5 \rightarrow NO_2 + NO_3$	4.36×10^{-2} (*)	DeMore et al. (1997)
KHNO4OH	$OH + HNO_4 \rightarrow NO_2$	4.65×10^{-12}	Sander et al. (2006)
KNO2HO2	$NO_2 + HO_2 \rightarrow HNO_4$	1.39×10^{-12}	Sander et al. (2002)
KHNO4M	$HNO_4 (+ M) \rightarrow NO_2 + HO_2$	8.62×10^{-2} (*)	Sander et al. (2006)
KODM	$O^1D (+ M) \rightarrow$	2.88×10^{-11}	Sander et al. (2002)
KH2OOD	$O^1D + H_2O \rightarrow OH + OH$	2.2×10^{-10}	Sander et al. (2002)
KO3HO2	$O_3 + HO_2 \rightarrow OH$	2.05×10^{-15}	DeMore et al. (1997)
KCOOH	$CO + OH \rightarrow HO_2$	2.4×10^{-13}	Sander et al. (2003)
KO3OH	$O_3 + OH \rightarrow HO_2$	6.83×10^{-14}	DeMore et al. (1997)
KHPOH	$OH + H_2O_2 \rightarrow HO_2$	1.7×10^{-12}	Sander et al. (2002)
KFRMOH	$OH + HCHO \rightarrow CO + HO_2$	1.0×10^{-11}	Sander et al. (2000)
KCH4OH	$OH + CH_4 \rightarrow CH_3O_2$	6.31×10^{-15}	DeMore et al. (1994)
KOHMPER	$OH + CH_3OOH \rightarrow 0.7CH_3O_2 + 0.3HCHO + 0.3OH$	7.43×10^{-12}	Sander et al. (2006)
KOHROOH	$OH + ROOH \rightarrow 0.7XO_2 + 0.3OH$	3.0×10^{-12}	Atkinson (1994)
KMO2HO2	$CH_3O_2 + HO_2 \rightarrow CH_3OOH$	5.57×10^{-12}	Sander et al. (2000)
KMO2MO2	$CH_3O_2 + CH_3O_2 \rightarrow 1.33HCHO + 0.67HO_2$	4.73×10^{-13}	Sander et al. (2000)
KHO2OH	$OH + HO_2 \rightarrow$	1.11×10^{-10}	Sander et al. (2006)
KHO2HO2	$HO_2 + HO_2 \rightarrow H_2O_2$	5.0×10^{-12}	Sander et al. (2002)

KH2OH	$OH + H_2 \rightarrow HO_2$	8.233×10^{-2}	$1.06 * KCH4OH * [H_2]$
KC41	$NO_3 + HCHO \rightarrow HNO_3 + CO + HO_2$	5.8×10^{-16}	Sander et al. (2006)
KC43	$ALD2 + OH \rightarrow C_2O_3$	1.62×10^{-11}	Gery et al. (1989)
KC44	$ALD2 + NO_3 \rightarrow C_2O_3 + HNO_3$	2.5×10^{-15}	Gery et al. (1989)
KC46	$NO + C_2O_3 \rightarrow HCHO + XO_2 + HO_2 + NO_2$	1.91×10^{-11}	Gery et al. (1988)
KC47	$NO_2 + C_2O_3 \rightarrow PAN$	9.91×10^{-12}	0.96*KC47 Atkinson et al. (2006)
KC48	$PAN \rightarrow NO_2 + C_2O_3$	4.23×10^{-4} (*)	Gery et al. (1988)
KC49	$C_2O_3 + C_2O_3 \rightarrow 2HCHO + 2XO_2 + 2HO_2$	2.0×10^{-12}	Gery et al. (1989)
KC50	$C_2O_3 + HO_2 \rightarrow HCHO + XO_2 + HO_2 + 0.79OH + 0.21ROOH$	6.5×10^{-12}	Gery et al. (1989)
KC52	$OH + PAR \rightarrow 0.87XO_2 + 0.76ROR + 0.11HO_2 + 0.11ALD2 + 0.11RXPAR + 0.13XO_2N$	8.1×10^{-13}	Gery et al. (1989)
KC53	$ROR \rightarrow 1.1ALD2 + 0.96XO_2 + 0.04XO_2N + 0.02ROR + 2.1RXPAR + 0.94HO_2$	2193.25	Gery et al. (1989)
KC54	$ROR \rightarrow HO_2$	1600.0 (*)	Gery et al. (1989)
KC57	$OH + OLE \rightarrow HCHO + ALD2 + XO_2 + HO_2 + RXPAR$	2.82×10^{-11}	Gery et al. (1989)
KC58	$O_3 + OLE \rightarrow 0.44ALD2 + 0.64HCHO + 0.25HO_2 + 0.29XO_2 + 0.37CO + 0.9RXPAR + 0.4OH$	1.03×10^{-17}	Stockwell et al. (1997)
KC59	$NO_3 + OLE \rightarrow 0.91XO_2 + HCHO + 0.09XO_2N + NO_2 + ALD2 + RXPAR$	7.7×10^{-15}	Gery et al. (1989)
KC61	$OH + C_2H_4 (+M) \rightarrow HO_2 + 1.56HCHO + 0.22ALD2 + XO_2$	8.15×10^{-12}	Sander et al. (2002)
KC62	$O_3 + C_2H_4 \rightarrow HCHO + 0.26HO_2 + 0.12OH + 0.43CO$	1.59×10^{-18}	DeMore et al. (1994)
KC73	$OH + CH_3COCHO \rightarrow XO_2 + C_2O_3$	1.7×10^{-11}	Atkinson et al. (1992)
KC76	$OH + ISOP \rightarrow 0.85XO_2 + 0.61HCHO + 0.58OLE + 0.85HO_2 + 0.15 XO_2N + 0.03CH_3COCHO + 0.63PAR$	1.0×10^{-10}	Atkinson (1994)
KC77	$O_3 + ISOP \rightarrow 0.9HCHO + 0.55OLE + 0.36CO + 0.15C_2O_3 + 0.63PAR + 0.3HO_2 + 0.18XO_2 + 0.03CH_3COCHO + 0.28OH$	1.43×10^{-17}	Atkinson (1994)
KC78	$NO_3 + ISOP \rightarrow 0.9HO_2 + 0.9ORGNTR + 0.45OLE + 0.12ALD2 + 0.08CH_3COCHO + 0.1NO_2 + 0.03HCHO$	7.8×10^{-13}	Wille et al. (1991)
KC79	$NO + XO_2 \rightarrow NO_2$	7.68×10^{-12}	Atkinson (1994)
KC80	$XO_2 + XO_2 \rightarrow$	1.33×10^{-12}	Atkinson (1994)
KC81	$NO + XO_2N \rightarrow ORGNTR$	6.8×10^{-13}	Atkinson et al. (2006)
KC82	$HO_2 + XO_2 \rightarrow ROOH$	1.0×10^{-11}	Atkinson (1994)
KC83	$PAR + RXPAR \rightarrow$	8.0×10^{-11}	Hertel et al. (1993)

KC84	$OH + ORGNTR \rightarrow NO_2 + XO_2$	1.78×10^{-12}	Atkinson (1994)
KC85	$HO_2 + XO_2N \rightarrow ROOH$	8.88×10^{-13}	Atkinson (1994)
Kdmsoha	$DMS + OH \rightarrow SO_2$	4.38×10^{-12}	Chin et al. (1996)
Kdmsohb	$DMS + OH \rightarrow 0.75\ SO_2 + 0.25MSA$	1.74×10^{-12}	Chin et al. (1996)
Kdmsno3	$DMS + NO_3 \rightarrow SO_2$	1.01×10^{-12}	Sander et al. (2006)
Kso2oh	$OH + SO_2 \rightarrow SO_4$	8.85×10^{-13}	Sander et al. (2002)
Knh3oh	$OH + NH_3 \rightarrow NH_2$	1.57×10^{-13}	Sander et al. (2006)
Knh2no	$NO + NH_2 \rightarrow$	1.72×10^{-11}	DeMore et al. (1994)
Knh2no2	$NO_2 + NH_2 \rightarrow$	1.86×10^{-11}	Sander et al. (2006)
Knh2ho2	$HO_2 + NH_2 \rightarrow$	3.4×10^{-11}	Sander et al. (2006)
Knh2o2	$O_2 + NH_2 \rightarrow$	3.09×10^{-12}	Sander et al. (2006)
Knh2o3	$O_3 + NH_2 \rightarrow$	1.90×10^{-13}	Sander et al. (2006)

Table B: The details concerning the reaction data used for the calculation of the chemical reaction rates in the TM model. The ubiquitous reaction products O_2 and H_2O are not shown as these are fixed using the meteorological input data given in the AFGL atmospheres and not calculated explicitly by the EBI solver. The red reactions indicate updates to the rate data that have already been made to the modified CBM4 mechanism prior to this study. The reactions involving SO_2, DMS and NH_3 have been added to the modified CBM4 scheme in order to account for the oxidation of the important trace gases missing from the standard scheme. Reaction rates with (*) are in units of s^{-1}.

Appendix C

Photolysis Rates

In Table C below we provide details concerning the photolysis rates that are calculated in the TM model. The following details are given: the name of the photolysis rate, the stiochiometry of the reaction and sample rates calculated for standard temperature and pressure (298K and 1013hpa) at SZA = 10°, 45° and 60°, respectively. All input data originates from DeMore et al. (1997) apart from the exceptions given in the footnotes of the table (M. Krol, personal communication, 2007). These photo-dissociation rates were used for the contributions made by both TM4 and TM5 to the fourth assessment of the IPCC, as well as the many intercomparison papers subsequently published (*e.g.* Stevenson et al., 2006).

Reaction name	Stiochiometry	$J_{sza=10^\circ}$ s^{-1}	$J_{sza=45^\circ}$ s^{-1}	$J_{sza=60^\circ}$ s^{-1}
JO3d[1]	$O_3 + h\nu \rightarrow O^1d$	3.69 x 10^{-6}	1.75 x 10^{-6}	7.72 x 10^{-7}
JNO2	$NO_2 + h\nu \rightarrow NO + O_3$	9.24 x 10^{-3}	7.29 x 10^{-3}	5.39 x 10^{-3}
JH2O2	$H_2O_2 + h\nu \rightarrow OH + OH$	7.84 x 10^{-6}	5.23 x 10^{-6}	3.25 x 10^{-6}
JHNO3	$HNO_3 + h\nu \rightarrow OH + NO_2$	8.00 x 10^{-7}	4.58 x 10^{-7}	2.43 x 10^{-7}
JHNO4	$HNO_4 + h\nu \rightarrow HO_2 + NO_2$	5.29 x 10^{-6}	3.02 x 10^{-6}	1.57 x 10^{-6}
JN2O5	$N_2O_5 + h\nu \rightarrow NO_2 + NO_3$	5.31 x 10^{-5}	3.65 x 10^{-5}	2.35 x 10^{-5}
JaCH2O	$HCHO + h\nu \rightarrow CO$	5.71 x 10^{-5}	4.18 x 10^{-5}	2.85 x 10^{-5}
JbCH2O	$HCHO + h\nu \rightarrow CO + 2HO_2$	3.85 x 10^{-5}	2.53 x 10^{-5}	1.51 x 10^{-5}
JMEPE	$CH_3OOH + h\nu \rightarrow HCHO + HO_2 + OH$	6.21 x 10^{-6}	4.25 x 10^{-6}	2.71 x 10^{-6}
JaNO3	$NO_3 + h\nu \rightarrow NO_2 + O_3$	0.184	0.167	0.149
JbNO3	$NO_3 + h\nu \rightarrow NO$	2.20 x 10^{-2}	2.00 x 10^{-2}	1.77 x 10^{-2}
JPAN	$PAN + h\nu \rightarrow C_2O_3 + NO_2$	9.00 x 10^{-7}	5.62 x 10^{-7}	3.27 x 10^{-7}
JORGN [2]	$ORGNTR + h\nu \rightarrow HO_2 + NO_2$	5.52 x 10^{-6}	3.10 x 10^{-6}	1.58 x 10^{-6}
J45	$ALD2 + h\nu \rightarrow HCHO + XO_2 + CO + 2HO_2$	4.91 x 10^{-5}	3.15 x 10^{-5}	1.85 x 10^{-5}
J74 [3]	$CH_3C(O)CHO + h\nu \rightarrow C_2O_3 + HO_2 + CO$	1.93 x 10^{-3}	1.26 x 10^{-3}	7.57 x 10^{-4}
JROOH [4]	$ROOH + h\nu \rightarrow OH$	6.21 x 10^{-6}	4.25 x 10^{-6}	2.72 x 10^{-6}

Table C: The nomenclature and stiochiometry of the photolysis reactions implemented in the TM model, where the reaction products O_2 and H_2O are not shown as these are prescribed from meteorological input data and not calculated explicitly by the EBI solver. The photolysis rates are calculated using the summer mid-latitude AFGL atmospheric profile (Anderson et al., 1986) with marine aerosol prescribed for the bottom 3 km of the atmospheric column as defined by Shettle and Fenn (1979) and background aerosol defined for the remaining layers. The wavelength dependant ground albedo is taken from the atlas of Koelemeijer et al. (2003). The photolysis rates given in blue are temperature independent. Additional details: [1] the quantum yield for the production of O^1D from the photolysis of O_3 is taken from Shetter et al. (1996), [2] JORGN = 2.5* JORGN where the □ values for a C4 mono-nitrate are used (Roberts and Fayer, 1989), [3] J74 = 50*JbCH2O (TM5) or JbCH2O (TM4) where values for TM5 are given, [4] JROOH = JMEPE.

Appendix D

Emissions and Depositions

In Tables D1 and D2 below we provide details concerning the emission and deposition fluxes used in the chemical box model. For the emissions the following details are given: the name of the chemical species for which the emission is relevant and the four fluxes for the different atmospheric scenarios. It should be noted that 'rural' is not pristine but still influenced by regional anthropogenic emissions, whereas 'ocean' is completely isolated from such influences (*e.g.*) the Southern Pacific. For the depositions the following details are given: the name of the chemical species for which the flux is relevant, the magnitude of the flux and the source of the value. The sources for these emission fluxes are provided in the footnote of the table. It should be noted that none of the fluxes are temperature dependent and only isoprene has a diurnal variation imposed for the emission flux.

Name of species	Marine Molec. cm^{-2} s^{-1}	Rural Molec. cm^{-2} s^{-1}	Urban Molec. cm^{-2} s^{-1}	Tropical Molec. cm^{-2} s^{-1}
NO	7.0×10^4 [1]	2.86×10^5 [2]	2.25×10^6 [7]	4.75×10^5 [8]
CO	8.53×10^5 [2]	3.70×10^6 [2]	1.0×10^7 [8]	8.53×10^5 [10]
NH_3	4.57×10^5 [2]	9.06×10^5 [2]	3.03×10^6 [2]	4.57×10^5 [10]
SO_2	7.92×10^4 [2]	2.91×10^5 [2]	3.27×10^6 [2]	7.92×10^4 [10]
HCHO	17.8 [2]	3028. [2]	2.58×10^5 [2]	3028. [10]
ISOP	0.0 [2]	6.0×10^6 [5]	3.0×10^6 [9]	9.30×10^6 [6]
C_2H_4	45.0 [2]	4.54×10^4 [2]	2.61×10^6 [2]	0.0 [9]
ALD2	10.51 [2]	3171 [2]	5.93×10^5 [2]	0.0 [9]
PAR	24.43 [3]	7.33×10^5 [3]	3.53×10^6 [8]	24.43 [10]
CH_3COCHO	0.721 [4]	1.13×10^4 [4]	9.88×10^5 [4]	0.0 [9]
OLE	11.7 [5]	1.55×10^4 [5]	1.24×10^6 [5]	0.0 [9]

Table D1: The Emission fluxes used in the chemical box model studies for the various scenarios. The sources of these emission fluxes are as follows: [1] equivalent to 0.1ppbv day^{-1} (estimated), [2] from Ervens et al. (2003) based on a synthesis of the inventories of Guenther et al. (1995) and Olivier et al. (1996), [3] set to the sum of the emission fluxes for C_2H_6, HC3, HC5 and HC8 as given in Ervens et al. (2003) using the appropriate scaling factors to convert to PAR, [4] set equivalent to the flux for XYL given in Ervens et al. (2003) as $CH_3C(O)CHO$ is considered to be a stable oxidation products of XYL (Houweling et al., 1998), [5] set equivalent to the flux for DIEN given in Ervens et al. (2003), [6] based on Pöschl et al. (2000) where a diurnal variation is imposed on the emission rate, [7] from Pöschl et al. (2000), [8] emission fluxes selected by tuning the chemical box model, [9] estimated, [10] best guesses using the information for the pristine Marine scenario. NH_3 is lower than rural due to lack of agriculture. CO emissions are implicit in the NMHC emissions.

Name of species	Ocean 10^{-6} s^{-1}	Land 10^{-6} s^{-1}	Reference
NO	0.8	0.9	Von Kuhlmann (2001)
NO_2	0.8	0.9	Von Kuhlmann (2001)
NO_3	0.8	0.9	Von Kuhlmann (2001)
HNO_3	10.0	20.0	Schwartz and White (1981)
N_2O_5	0.4 [1]	0.45 [1]	Von Kuhlmann (2001)
HNO_4	0.8	0.9	Von Kuhlmann (2001)
H_2O_2	10.0	9.0	Lind and Kok (1986)
CO	0.0	0.2	Von Kuhlmann (2001)
O_3	0.5	2.6	Von Kuhlmann (2001)
NH_3	10.0	10.0	Ervens et al. (2003)
SO_2	5.0	10.0	Ervens et al. (2003)
SO_4	2.5[2]	5.0[2]	Ervens et al. (2003)
HCHO	9.0	3.6	Staudinger and Roberts(1996)
CH_3OOH	3.5	1.8	O'Sullivan et al. (1996)
PAN	0.2	1.0	Von Kuhlmann (2001)
CH_3COCHO	9.0	2.2	Betterton and Hoffman (1988)
ALD2	0.3	0.7	Staudinger and Roberts (1996)
ROOH	4.0	1.4	O'Sullivan et al. (1996)
C2O3	10.0 [3]	6.4 [3]	O'Sullivan et al. (1996)
ORGNTR	0.0 [4]	0.1 [4]	Kames and Schurath(1992)
MSA	2.5 [2]	5.0 [2]	Ervens et al. (2003)
NH_4	10.0 [5]	10.0 [5]	Ervens et al. (2003)

Table D2: Deposition velocities included in the chemical box model for both the ocean (marine) and land scenarios (rural, urban and tropics). Additional details are: [1] scaled for two N atoms, [2] set equal to 50% of deposition velocity of SO_2, [3] set equal to value for $CH_3C(O)O_2H$, [4] set equal to 1-butylnitrate, [5] set equal to deposition velocity of NH_3.

Appendix E

Initial Starting Conditions

In table E below we provide details regarding the initial conditions used for the various atmospheric scenarios defined for the box model study for 23 of the chemical species.

Chemical species	Marine ppbv	Rural ppbv	Urban ppbv	Tropical ppbv
O_3	30 [1]	40 [1]	90 [1]	20 [5]
NO_x (as NO_2)	0.5 [1]	1.5 [1]	4.5 [1]	0.5 [6]
H_2O_2	0.43 [2]	1.0 [1]	1.0 [1]	0.43 [6]
CH_4	1760 [2]	1760 [2]	1760 [2]	1760 [2]
CO	75 [2]	150 [1]	300 [1]	200 [5]
HNO_3	0.67 [2]	0.3 [1]	1.0 [1]	0.1 [5]
CH_3OOH	0.44 [2]	0.07 [2]	0.01 [2]	1.5×10^{-2} [2]
HCHO	0.3 [2]	0.59 [2]	1.0 [1]	1.0 [5]
PAR	5.0 [3]	8.5 [3]	15.8 [3]	5.0 [5]
C_2H_4	1.7×10^{-2} [2]	4.7 [2]	5.15 [2]	0.63 [2]
OLE	1.7×10^{-2} [2]	1.37 [2]	1.71 [2]	0.61 [2]
ALD2	7.4×10^{-2} [2]	2.25 [2]	5.67 [2]	0.39 [2]
PAN	3.5×10^{-2} [2]	0.32 [2]	0.38 [2]	0.42 [2]
ROOH	0.6 [2]	4.6×10^{-2} [2]	4.7×10^{-2} [2]	8.9×10^{-2} [2]
ORGNTR	4.8×10^{-2} [2]	3.6×10^{-2} [2]	3.7×10^{-2} [2]	7.4×10^{-2} [2]
ISOP	1×10^{-2} [2]	2.0 [5]	1.0 [7]	5.0 [5]
SO_2	0.72 [2]	1.0 [1]	5.0 [1]	0.3 [2]
DMS	4×10^{-2} [2]	2.7×10^{-3} [2]	5.7×10^{-3} [2]	1.5×10^{-4} [2]
NH_3	2.8×10^{-2} [2]	1.9 [2]	5.9 [2]	0.45 [2]
SO_4	6.7×10^{-2} [2]	0.31 [2]	0.37 [2]	4.6×10^{-2} [2]
NH_4	0.1 [2]	3.5 [2]	3.4 [2]	9.2×10^{-2} [2]
MSA	2.3×10^{-3} [2]	2.7×10^{-4} [2]	2.6×10^{-4} [2]	1×10^{-4} [2]
MGLY	0.0 [4]	1×10^{-2} [4]	0.1[4]	0.0 [5]

Table E: Initial conditions for the four atmospheric scenarios chosen in this study. For $[H_2]$ and $[H_2O]$, fixed mixing ratios of 550 ppbv and that defined in bottom layer of the relevant standard atmosphere are used, respectively. Additional details: [1] from Ervens et al. (2003), [2] values obtained from averaged TM5 output for the relevant region, [3] set equal to the sum of alkanes given in Ervens et al. (2003), [4] set equal to initial XYL conditions in Ervens et al. (2003), [5] from Poschl et al. (2000), [6] set equal to pristine ocean, [7] estimated.

Appendix F

Differences in Reaction Rates

In table F below we provide information regarding the percentage differences introduced to the chemical reaction rates at STP when adopting the latest JPL recommendations [Sander et al., 2006]. Differences are calculated by comparison to those rates provided in Appendix B.

Reaction rate	$K_{298k,1atm}$ TM value	$K_{298k,1atm}$ updated	Percentage difference	New rate expression
KNOO3	1.82×10^{-14}	1.95×10^{-14}	+7.1%	3.0E-12*exp(-1500/T)
KHO2NO	8.56×10^{-12}	8.10×10^{-12}	-5.7%	3.5E-12*exp(250/T)
KMO2NO	7.68×10^{-12}	7.66×10^{-12}	-0.2%	2.8E-12*exp(300/T)
KNO2OH	8.26×10^{-12}	1.06×10^{-11}	+28.3%	K_o = 1.8E-30*(300/T) $^{3.0}$ K_∞ = 2.8E-11
KNO2NO3	1.27×10^{-12}	1.19×10^{-12}	-6.7%	K_o = 2.0E-30*(300/T) $^{4.4}$ K_∞ = 1.4E-12*(300/T) $^{0.7}$
KN2O5	4.36×10^{-2}	4.1×10^{-2}	-6.0%	KNO2NO3/EQN2O5[1]
KNO2HO2	1.39×10^{-12}	1.14×10^{-12}	-17.9%	K_o = 2.0E-31*(300/T) $^{3.4}$ K_∞ = 2.9E-12*(300/T) $^{1.1}$
KODM	2.88×10^{-11}	3.25×10^{-11}	+12.8%	3.3E-11*exp(55/T)*[N_2] + 2.15E-11*exp(110/T)*[O_2]
KH2OOD	2.2×10^{-10}	1.99×10^{-10}	-10%	1.63E-10*exp(60/T)
KO3HO2	2.05×10^{-15}	1.93×10^{-15}	-6.2%	1.0E-14*exp(-490/T)
KCOOH	2.4×10^{-13}	2.37×10^{-13}	-1.25%	K_o = 5.9E-33*(300/T) $^{1.4}$ K_∞ = 1.1E-12*(300/T) $^{-1.3}$ K_o = 1.5E-13*(300/T) $^{-0.6}$ K_∞ = 2.1E9*(300/T) $^{-6.1}$
KO3OH	6.83×10^{-14}	7.25×10^{-14}	+6.1%	1.7E-12*exp(-940/T)
KCH4OH	6.31×10^{-15}	6.34×10^{-15}	+0.5%	2.45E-12*exp(-1775/T)
KMO2HO2	5.57×10^{-12}	5.1×10^{-12}	-9.2%	4.1E-13*exp(750/T)
KMO2MO2	4.73×10^{-13}	3.52×10^{-13}	-21.1%	9.5E-14*exp(390/T)
KHO2HO2	5.0×10^{-12}	4.56×10^{-12}	-8.8%	3.5E-13*exp(430/T) 1.77E-33*exp(1000/T) 1.4E-21*exp(2200/T)
KH2OH	6.69×10^{-15}	5.09×10^{-15}	-24.0%	2.8E-12*exp(-1800/T)
KHPOH	1.7×10^{-12}	1.8×10^{-12}	+5.8%	1.8E-12
KFRMOH	1.0×10^{-11}	8.37×10^{-12}	-19.0%	5.5E-12*exp(125/T)
KC43	1.63×10^{-11}	1.74×10^{-11}	+4.3%	Average of : 4.4E-12*exp(365/T) 4.9E-12*exp(405/T)
KC44	2.5×10^{-15}	4.61×10^{-15}	+84.0%	Average of : 1.4E-12*exp(-1860/T) 6.5E-15
KC46	1.91×10^{-11}	7.66×10^{-12}	-82.9%	8.1E-12*exp(270/T)

KC47	9.91×10^{-12}	1.04×10^{-11}	+4.9%	$K_0 = 2.7E\text{-}28*(300/T)^{7.1}$ $K_\infty = 1.2E\text{-}11*(300/T)^{0.9}$
KC48	4.23×10^{-4}	3.27×10^{-4}	-22.7%	$K_0 = 4.9E\text{-}3*\exp(-12100/T)$ $K_\infty = 5.4E16*\exp(-13830/T)$
KC49	2.0×10^{-12}	1.55×10^{-11}	+775%	2.9E-12*exp(500/T)
KC50	6.5×10^{-12}	1.41×10^{-11}	+217%	4.3E-13*exp(1040/T)
KC57	2.82×10^{-11}	3.90×10^{-11}	+38.3%	Average of : 1.86E-11*exp(175/T) 8.12E-12*exp(610/T) 2.6E-12*exp(610/T)
KC58	1.03×10^{-17}	5.47×10^{-18}	-46.9%	Average of : 8.5E-16*exp(-1520/T) 1.4E-15*exp(-2100/T) 1.0 E-17
KC59	7.7×10^{-15}	4.85×10^{-15}	-37.1%	Average of : 4.0E-14*exp(-400/T) 6.0E-16 3.5E-15
KC61	8.15×10^{-12}	8.2×10^{-12}	+0.6%	$K_0 = 1.0E\text{-}28*(300/T)^{4.5}$ $K_\infty = 8.8E\text{-}12*(300/T)^{0.85}$
KC62	1.59×10^{-18}	1.76×10^{-18}	+10.7%	1.2E-14*exp(-2630/T)
KC73	1.7×10^{-11}	1.5×10^{-11}	-11.8%	1.5E-11
KC76	1.0×10^{-11}	1.18×10^{-11}	+18%	2.7E-11*exp(390/T)
KC77	1.43×10^{-17}	1.29×10^{-17}	-9.8%	1.04E-14*exp(-1995/T)
KC78	7.8×10^{-13}	6.96×10^{-13}	-10.7%	3.15E-12*exp(-450/T)
KC79	7.68×10^{-12}	9.18×10^{-12}	+20%	Average of : 2.55E-12*exp(380/T) 2.9E-12*exp(350/T) 2.7E-12*exp(360/T)
KC80	1.33×10^{-12}	1.44×10^{-13}	+8.3%	Average of : 6.8E-14, 3.0E-13 and 6.4E-14
KC81	6.8×10^{-13}	8.85×10^{-12}	+1300%	2.6e-12*exp(365/T)
KC82	1.0×10^{-11}	7.85×10^{-12}	-22.5%	7.5E-13*exp(700/T)
KC84	1.78×10^{-12}	1.76×10^{-13}	-90.2%	5.9e-13*exp(-360/T)
KC85	8.88×10^{-13}	7.57×10^{-12}	+852%	(KC81*KC82)/KC79
Kdmsoha	4.38×10^{-12}	4.96×10^{-12}	+13.2%	1.1E-11*exp(-240/T)
Kdmsohb	1.74×10^{-12}	1.51×10^{-12}	-13.3%	1.0E-39*exp(5820/T) 5.0E-30*exp(6280/T)
Kso2oh	8.85×10^{-13}	9.38×10^{-13}	+6.0%	$K_0 = 3.3E\text{-}31*(300/T)^{4.3}$ $K_\infty = 1.6E\text{-}12*(300/T)$
Knh2no	1.72×10^{-11}	1.81×10^{-11}	+5.2%	4.0E-12*exp(450/T)

Table F: The percentage differences in the reaction rates which are updated in this box-model study. For Keq(N_2O_5), Keq(HNO_4) and Keq(PAN), where Keq = k_f/k_b, there are changes of <0.1%, -17.9% and -25%, respectively.

Appendix G

The partitioning of Non-Methane Volatile emissions into the modified CBM4 mechanism

In table G below we provide information regarding the partitioning of the non-methane hydrocarbon inventory used in the IPCC and Royal Society simulations which are discussed in Section 5. Updated partitioning ratios are used for the industrial and biomass burning contributions in this study. The changes are made based on the speciation tables provided in Yarwood et al. (2005). This changes the contributions of species such as benzene and tri-methylbenzene to the lumped CBM4 species. The stiochiometry for the contribution due to xylene was also updated where the original values of 2 molecules of PAR and MGLY from 1 molecule of xylene was downscaled to 1.1 molecules of PAR and 0.8 molecules of MGLY in line with the stiochiometry of the OH + XYL reaction in the original CBM4 mechanism (Gery et al. (1989)). Both the original and updated percentage contributions of each CBM4 species are listed in the table below.

Type of Emissions	PAR	ETE	OLE	ALD2	MGLY	HCHO	Total
IPCC (Industrial)	49.6	8.9	5.5	1.1	4.6	0.2	69.9
IPCC (biomass burning)	24.6	25.0	13.7	4.3	1.5	0.5	66.6
Updated (Industrial)	50.4	4.5	2.7	0.57	1.8	0.2	60.2
Updated (biomass burning)	28.7	12.5	6.8	2.2	0.6	0.5	51.3

Table G: Details of the partitioning of the total NMV emission inventories into the lumped species used in the modified CBM4 mechanism. Numbers are given for the ratios used in the original IPCC simulations and the CTM studies presented in Section 5.

Appendix H

Comparison of tropospheric O3 profiles versus selected ozonesonde measurements for the year 2000.

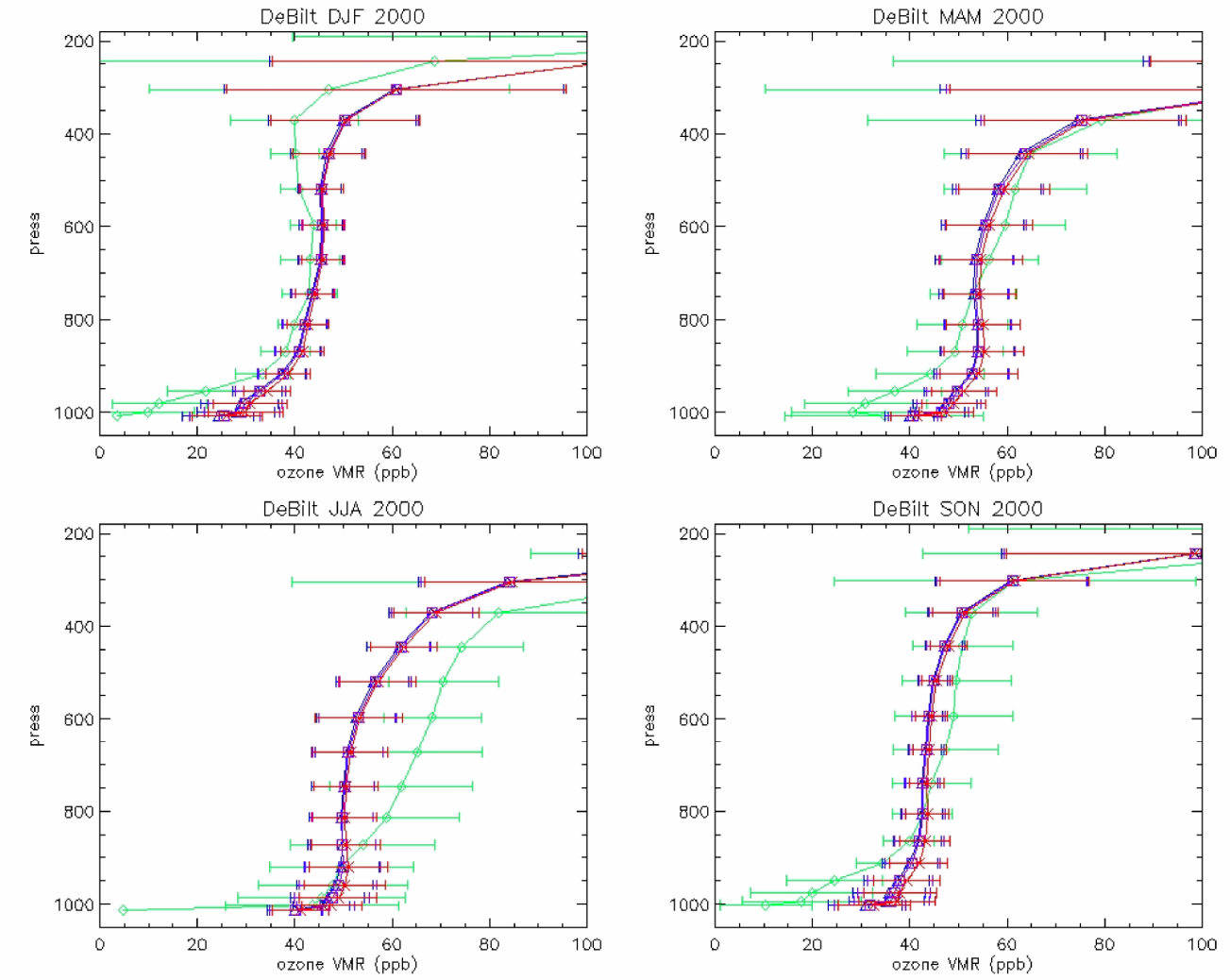

Figure H1: Comparison of seasonal means in the vertical profiles for tropospheric ozone between sondes (green), tm4_baseline_mgly (red), tm4_op_run () and tm4_GFED2000_ch4grad (blue) for De Bilt, the Netherlands (51.2°N, 5.2°E). The number of observations for each season are as follows: DJF (9), MAM (11), JJA (12) and SON (12)

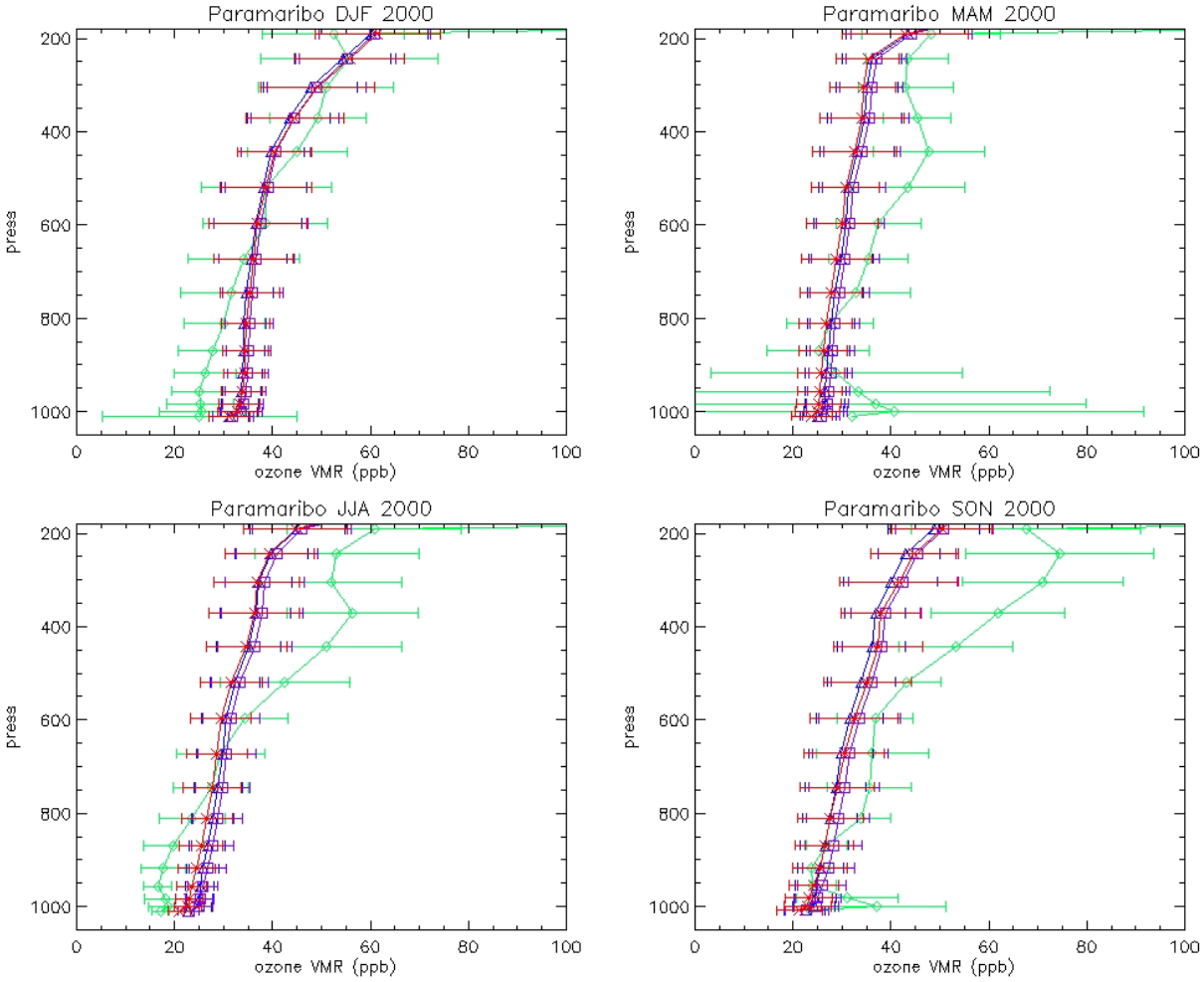

Figure H2: As for Figure H1 except for Paramaribo, Suriname (5.8°N, 55.2°W). The number of observations for each season are as follows: DJF (11), MAM (13), JJA (12) and SON (12).

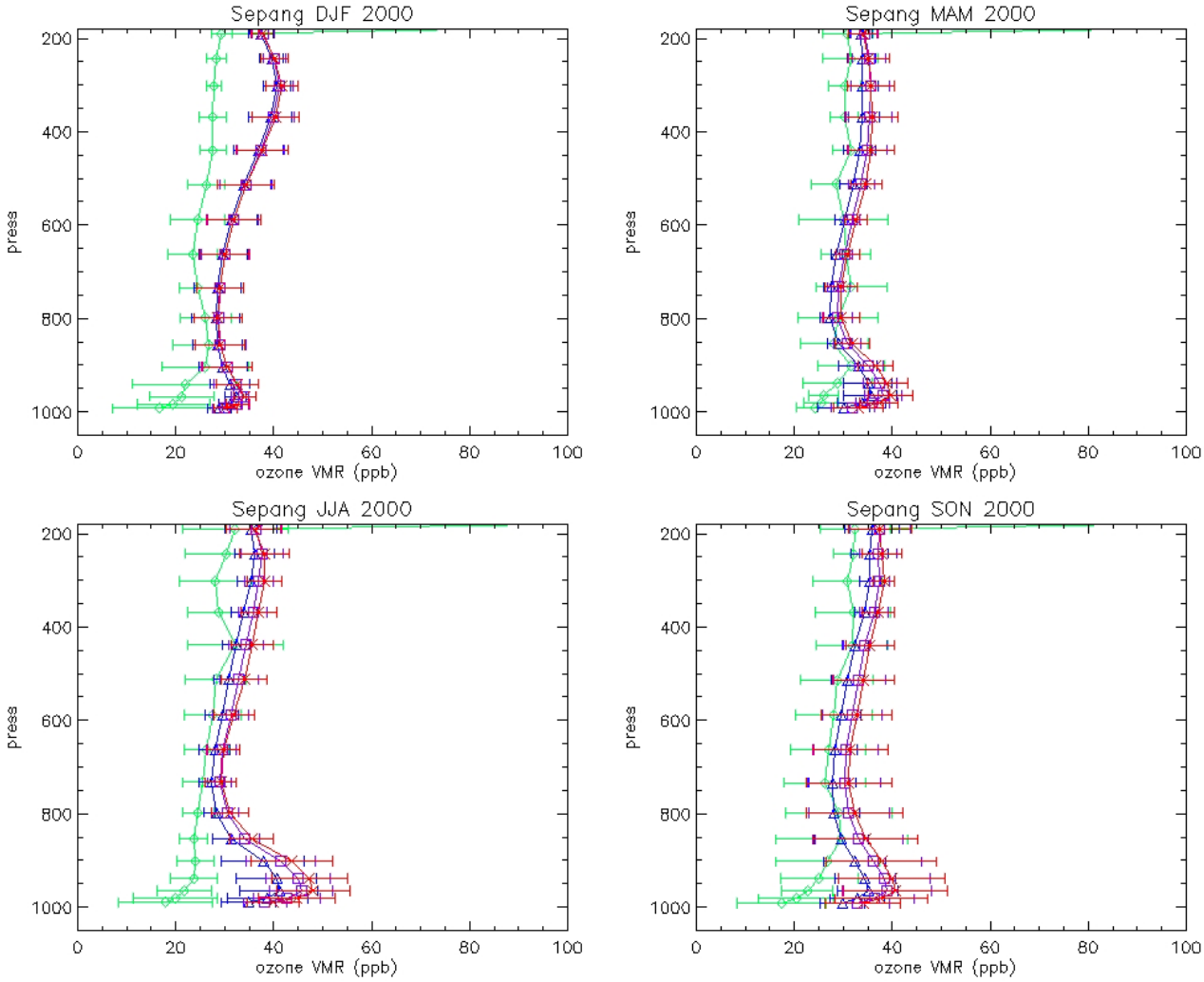

Figure H2: As for figure H1 except for Sepang Airport, Malaysia (2.7°N, 101.7°E). The numbers of observations for each season are as follows: DJF (5), MAM (5), JJA (5) and SON (7).

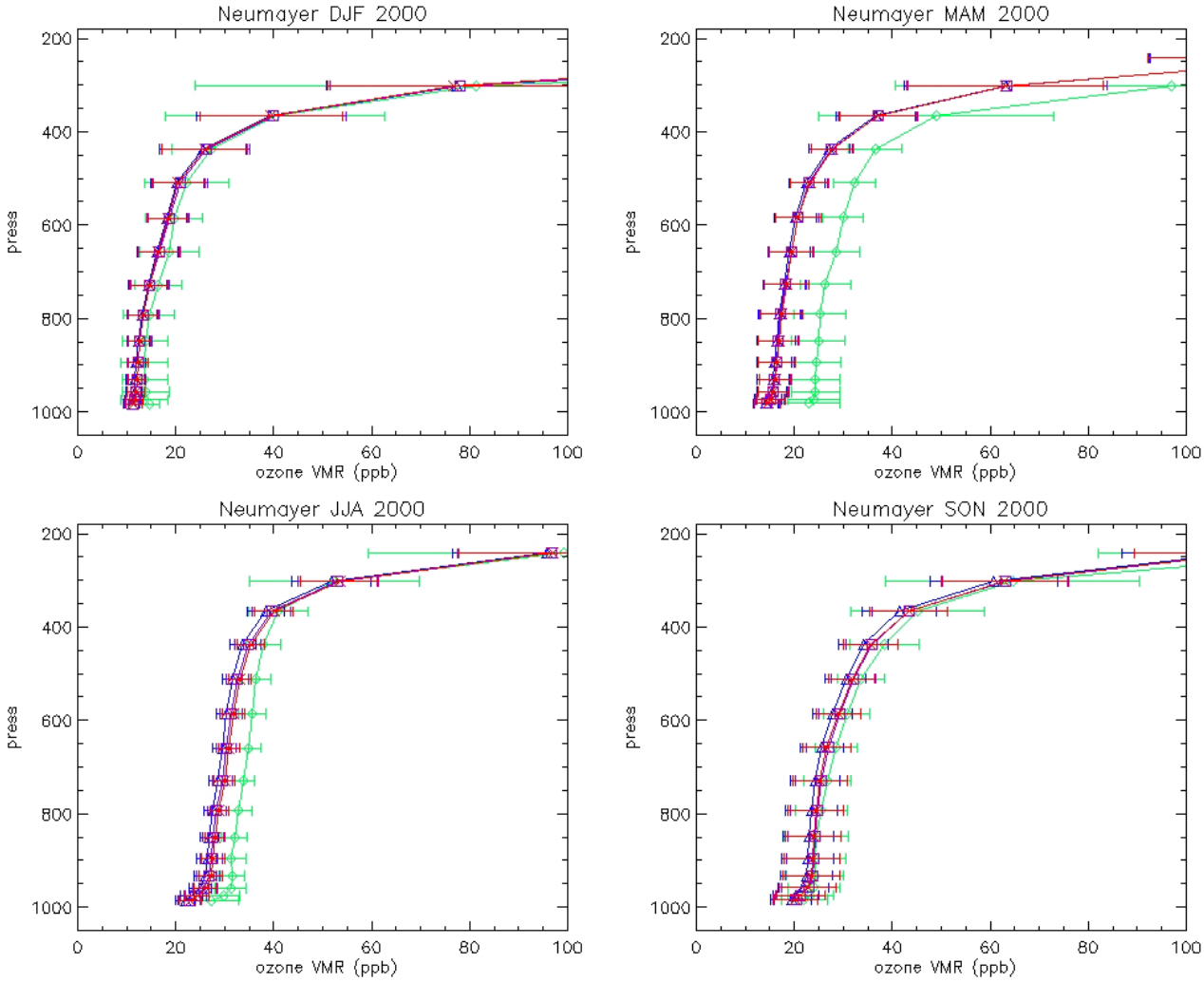

Figure H2: As for figure H1 except for Neumayer, Antarctica (70.6°S, 8.2°W). The numbers of observations for each season are as follows: DJF (16), MAM (13), JJA (16) and SON (27).

Appendix I

Comparison of surface [CO] versus selected CMDL measurement sites for 2000.

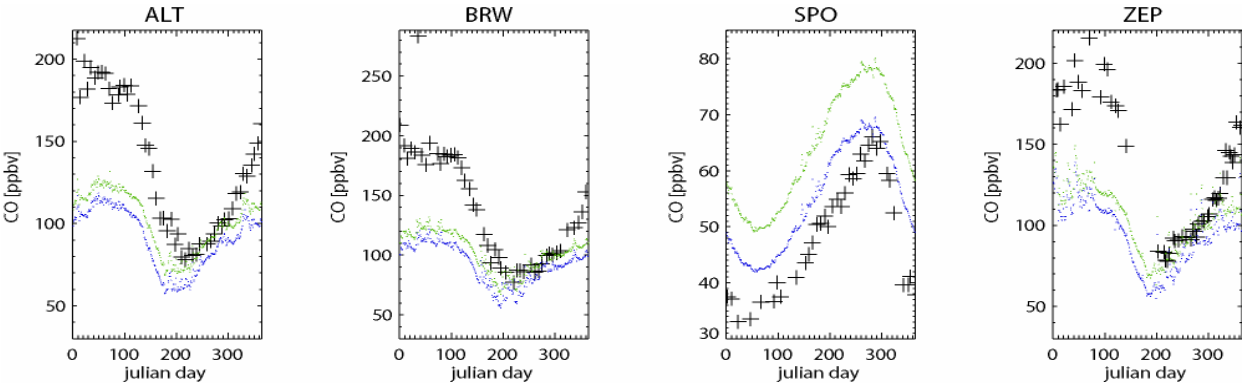

Figure 11: Comparison of surface [CO] for high latitude locations as derived from CMDL flask measurements (+), the tm4_baseline_run (blue) and the tm4_op_run_mgly (green). The sites shown are, from left to right, Alert (82.3°N, 62.3°W), Barrow (71.2°N, 156.4°W), South Pole (89.6°S, 24.5°W) and Mount Zeppelin (78.5°N, 11.5°E).

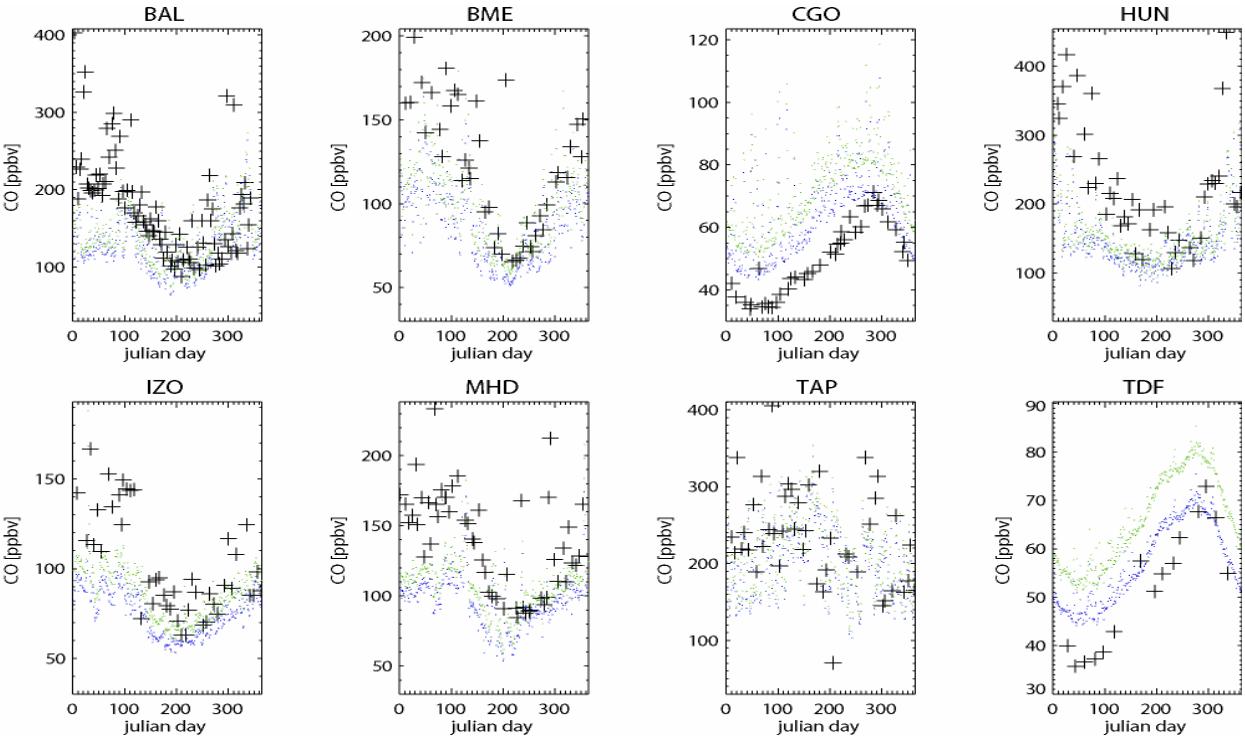

Figure 12: As for Fig 11 except for mid-latitude measurement sites. The sites shown are, from left to right, Baltic Sea (55.3°N, 16.4°E), Bermuda (32.2°N, 64.4°W), Cape Grim (40.4°S, 16.3°E), Hegyharsal (46.6°N, 16.2°E), Tenerife (28.2°N, 16.3°E), Mace Head (53.2°N, 9.5°W), Mahe Island (4.4°S, 55.1°E) and Tutuila (14.2°S, 170.3°W).

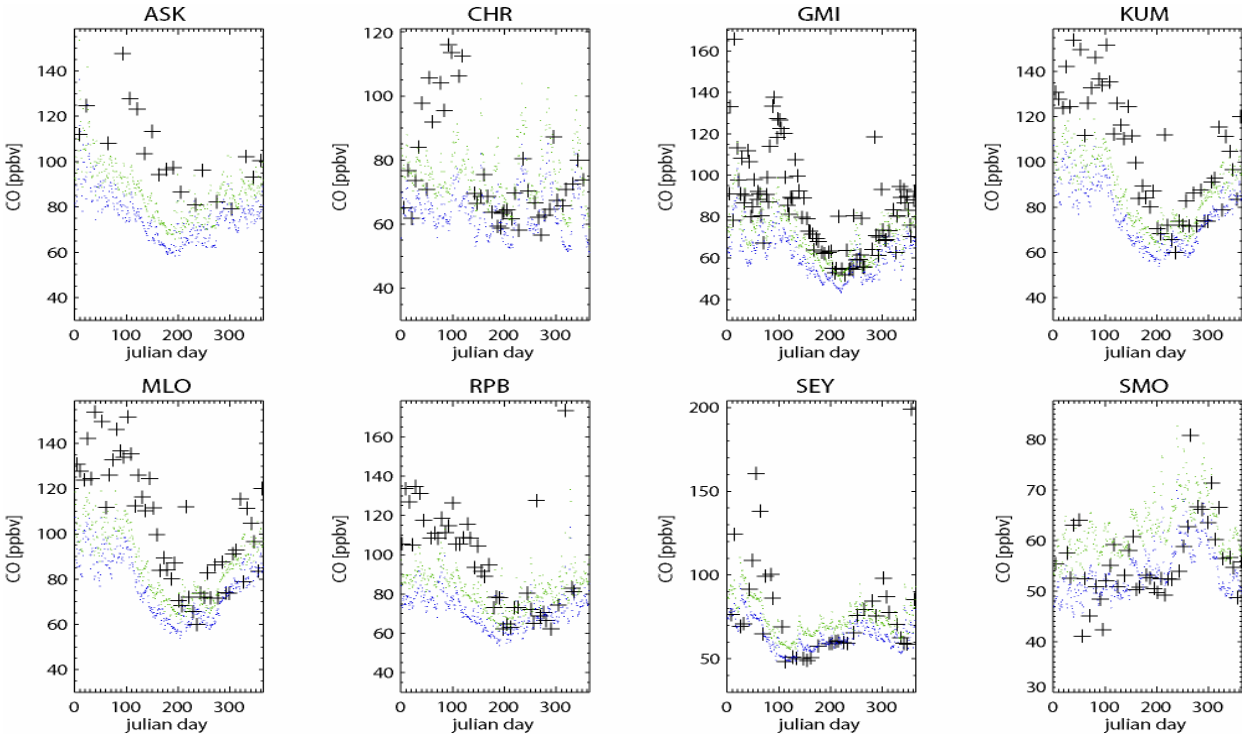

Figure 13: As for Fig 11 except for tropical measurement sites. The sites shown are, from left to right, Assekrem (23.1°N, 5.3°E), Christmas Island (1.4°N, 157.1°W), Guam (13.3°N, 144.5°E), Cape Kumahkahi (19.3°N, 154.5°W), Mount Loa (19.5°N, 155.5°W), Ragged Point (31.1°N, 59.3°W), Mahe Island (4.4°S, 55.1°E) and Tutuila (14.2°S, 170.3°W).

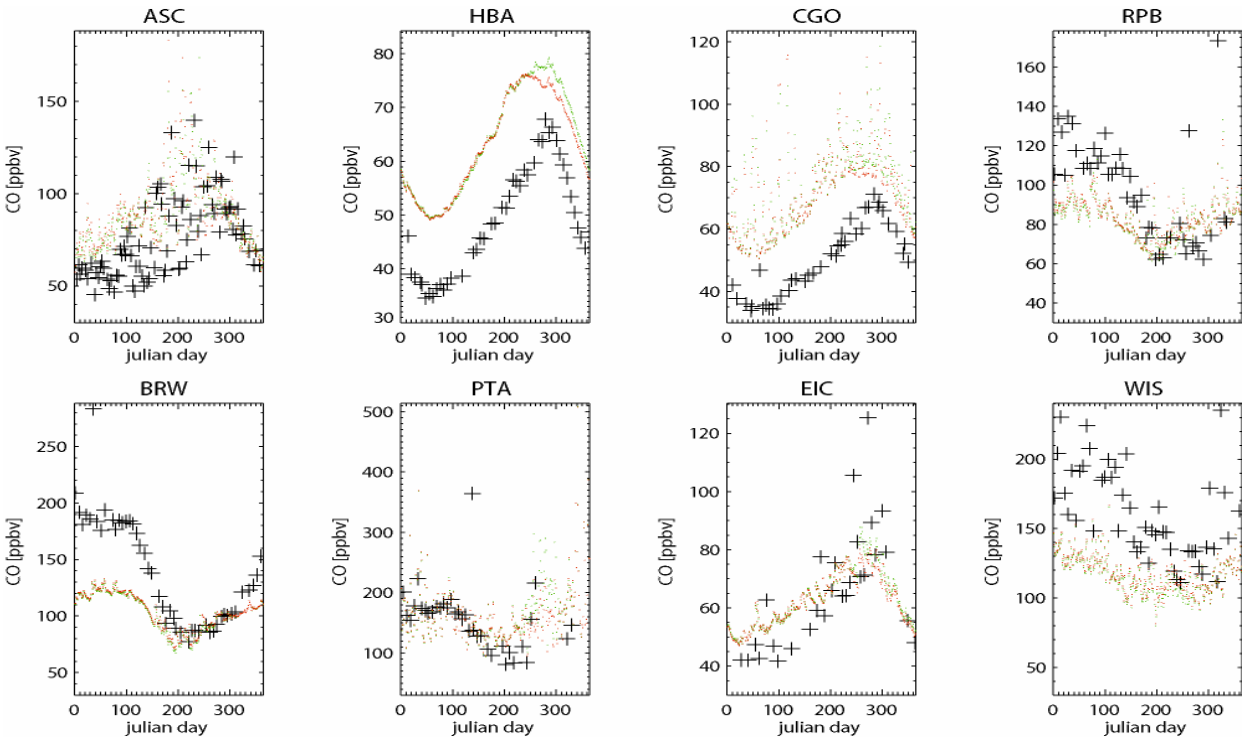

Figure 13: Comparison of surface [CO] for high latitude locations as derived from CMDL flask measurements (+), tm4_op_run_mgly (green).and the tm4_GFED2000_ch4grad run (orange). The sites shown are, from left to right, Assekrem (23.1°N, 5.3°E), Halley Bay (1.4°N, 157.1°W), Cape Grim (40.4°S, 16.3°E), Ragged Point (31.1°N, 59.3°W), Barrow (71.2°N, 156.4°W), Point Area (38.9°N, 123.7 °W), Easter Island (27.2°S, 109.5°W) and Seda Boker Negev desert (31.1°N, 34.9°E).

Bibliography

Anderson, G. P., J. H. Chetwynd, S. A. Clough, E. P. Shettle and F. X. Kneizys, AFGL Atmospheric Constituent Profiles (0-120km), *Environ. Res. Paper No.954*, AFGL-TR-86-0110, Air Force Geo-physics Lab., 1986.

Atkinson, R., Gas-phase tropospheric chemistry of organic compounds, *J. Phys. Chem. Ref. Data Monogr 2,* 1994.

Atkinson, R., D. L. Baulch, R. A. Cox, R. F. Hampson, J. A. Kerr and J. Troe, Evaluated kinetic and photochemical data for atmospheric chemistry: supplement IV, *Atmos. Environ.*, 26, 1187-1230, 1992.

Atkinson, R., D. L. Baulch, R. A. Cox, R. F. Hampson, J. A. Kerr, M. J. Rossi and J.Troe, Evaluated kinetic, photochemical and heterogeneous data for atmospheric chemistry: Supplement V - IUPAC Subcommittee on Gas Kinetic Data Evaluation for Atmospheric Chemistry, *J. Phys. Chem. Ref. Data*, 26, No.3, 521-1011, 1997.

Atkinson, R., D. L. Baulch, R. A. Cox, J. N. Crowley, R. F. Hampson, R. G. Hynes, M. E. Jenkin, M. J. Rossi, and J. Troe, Evaluated kinetic and photochemical data for atmospheric chemistry: Volume II – gas phase reactions of organic species, *Atms.Chem.Phys.*, *6*, 3625-4055, 2006.

Betterton, E. A. and M. R. Hoffmann, Henry's law constants of some environmentally important aldehydes, Env. Sci. Tech., 22, 1415-1418, 1988.

Bonisch, H., P. Hoor, Ch. Gurk, W. Feng, M. Chipperfield, A. Engel and B. Bregman, Model Evaluation of CO2 and SF6 in the extratropical UT/LS region, *J. Geophys. Res.,* 113, doi: 10.1029/2007JD008829, 2008.

Brasseur, G.P and D. Schimel, Atmospheric Chemistry and the Earth System, In: Atmospheric Chemistry and Global Change, Eds: Brasseur, G.P., J. J. Orlando and G.S.Tyndall, Oxford University Press, 1999.

Chen, Y. and L. Zhu, Wavelength-dependent photolysis of methylglyoxal in the 290-440 nm region, J. Phys. Chem. A, 104, 11126-11131, 2000.

Chin. M., D. J. Jacob, G. M. Gardner, M. S. Foreman-Fowler, P. A. Spiro and D. L. Savoie, A global three-dimensional model of tropospheric sulphate, *J. Geophys. Res., 101(D13)*, doi: 10.1029/96JD01221, 18667-18690, 1996.

de Laat, A. T. J., A. M. S. Gloudemans, I. Aben, M. Krol, J. F. Meirink, G. R. van der Werf and H. Schrijver, Scanning Imaging Absorption Spectrometer for Atmospheric Chartography carbon monoxide total columns: Statistical evaluation and comparison with chemistry transport model results, *J. Geophys. Res.*, *112,* doi:10.1029/2006JD008256, 2007.

de Meij, A., P. Thunis, C. Cuvelier, E. Vignati, F. Dentener, and M. Krol, The sensitivity of aerosol in Europe to two different emission inventories and temporal distribution of emissions, *Atmos. Chem. Phys.*, *6*, 4287-4309, 2006.

DeMore, W. B., S. P. Sander, D. M. Golden, R. F. Hampson, M. J. Kurylo, C. J. Howard, A. R. Ravishankara, C. E. Kolb and M. J. Molina, Chemical kinetics and photochemical data for use in stratospheric modelling, Evaluation No. 11, JPL publ. 94-26, Jet Propulsion Laboratory, Pasadena, CA, 1994.

DeMore, W. B., S. P. Sander, D. M. Golden, R. F. Hampson, M. J. Kurylo, C. J. Howard, A. R. Ravishankara, C. E. Kolb and M. J. Molina, Chemical kinetics and photochemical data for use in stratospheric modelling, Evaluation No. 12, JPL publ. 97-4, Jet Propulsion Laboratory, Pasadena, CA, 1997.

Dentener, F., J. Drevet, J.F. Lamarque, I. Bey, B. Eickhout, A.M. Fiore, D. Hauglustaine, L.W. Horowitz, M. Krol, U.C. Kulshrestha, M. Lawrence, C. Galy-Lacaux, S. Rast, D. Shindell, D. Stevenson, T. Van Noije, C. Atherton, N. Bell, D. Bergman, T. Butler, J. Cofala, B. Collins, R. Doherty, K. Ellingsen, J. Galloway, M. Gauss, V. Montanaro, J.F. Müller, G. Pitari, J. Rodriguez, M. Sanderson, F. Solmon, S. Strahan, M. Schultz, K. Sudo, S. Szopa, and O. Wild, 2006: Nitrogen and sulfur deposition on regional and global scales: A multimodel evaluation, *Global Biogeochem. Cycles*, 20, GB4003, doi:10.1029/2005GB002672, 2006.

Ervens, B., C. George, J. E. Williams, G. V. Buxton, G. A. Salmon, M. Bydder, F. Wilkinson, F. Dentener, P. Mirabel, R. Wolke and H. Herrmann, CAPRAM 2.4 (MODAC mechanism): An extended and condensed tropospheric aqueous phase mechanism and its application, *J. Geophys. Res.*, *108(D14)*, 4426, doi: 10.1029/2002JD002202, 2003.

Evans, M. J., and D. J. Jacob, Impact of new laboratory studies of N2O5 hydrolysis on global model budgets of tropospheric nitrogen oxides, ozone and OH, *Geophys. Res. Letts., 32*, doi: 10.1029/2005GL022469, 2005.

Ganzeveld, L., J. Lelieveld, and G.-J., Roelofs, A dry deposition parameterization for sulfur oxides in a chemistry and general circulation model, *J. Geophys. Res.*, *103(D5)*, doi: 10.1029/97JD03077, 5679-5694, 1998.

Gery, M., G. Z. Whitten, J. P. Killus and M. C. Dodge, A photochemical kinetics mechanism for urban and regional scale computer modelling, *J.Geophys.Res.*, *94*, 18925-18956, 1989.

Gloudemans, A.M.S., H. Schrijver, O. P. Hasekamp and I. Aben, Error analysis for CO and CH_4 total column retrievals from SCIAMACHY 2.3µm spectra, *Atms.Chem.Phys.Diss., 8,* 5183-5233, 2008.

Grossmann, D., G. K. Moortgat, M. Kibler, S. Schlomski, K. Bachmann, B. Alicke, A. Geyer, U. Platt, M.-U. Hammer, B. Vogel, D. Mihelcic, A. Hofzumahaus, F. Holland and A. Volz-Thomas, Hydrogen Peroxide, organic peroxides, carbonyl compounds and organic acids measured at Pabstthum during BERLINOZ, *J.Geophys.Res.*, *108*, doi:10.1029/2001JD001096, 2003.

Guelle, W., Y. J. Balkanski, M. Schulz, F. Dulac, and P. Monfray, Wet deposition in a global size-dependent aerosol transport model, (1) Comparison of a 1 year Pb simulation with ground measurements, *J. Geophys. Res.*, *103(D10)*, 11429-11446, doi: 10.1029/97JD03680, 1998.

Guenther, A., C. N. Hewitt, D. Erickson, R. Fall, C. Geron, T. Graedel, P. Harley, L. Klinger, M. Lerdau, W. A. McKay, T. Pierce, B. Scholes, R. Steinbrecher, R. Tallamraju, J. Taylor and P. Zimmerman, A global model of natural volatile organic compound emissions, *J. Geophys. Res.*, *100(D5)*, 8873-8892, doi: 10.1029/94JD02950, 1995.

Hanke, M., B. Umann, J. Uecker, F. Arnold, and H. Bunz, Atmopsheric measurements of gas phase HNO_3 and SO_2 using chemical ionization mass spectrometery during the MINOTROC field campaign 2000 on Monte Cimone, *Atmos.Chem.Phys.*, *3*, 417-536, 2003.

Hertel, O., R. Berkowicz, J. Christensen and O. Hov, Test of two numerical schemes for use in atmospheric transport-chemistry models, *Atms. Environ., Part A, 27*, 2591-2611, 1993.

Houweling, S., F. J. Dentener and J. Leileveld, The impact of non-methane hydrocarbon compounds on tropospheric photochemistry, *J. Geophys. Res.*, *103(D9)*, 10673-10696, doi: 10.1029/97JD03582, 1998.

Huang, H-C. and J. S. Chang, On the performance of numerical solvers for a chemistry submodel in three-dimensional air quality models, *J. Geophys. Res.*, *106(D17)*, 20175-20188, doi:10.1029/2000JD000121, 2001.

Huey, L.G., D. J. Tanner, D. L. Slusher, J. E. Dibb, R. Arimoto, G. Chen, D. Davis, M. P.Buhr, J.B. Nowak, R. L. Mauldin III, F. L. Eisele and E. Koscinch, CIMS measurements of HNO_3 and SO_2 at the South Pole during ISCAT 2000, *Atms. Environ., 32*, 5411-5421, 2004.

Jeffries, H.J., I. Voicu and K. Saxton, Experimental Tests of reactivity and re-evaluation of the Carbon Bond Four photochemical reaction mechanism, report to the U.S. Environmental protection agency, Process modelling research branch, Office of research and development, Research Triangle Park, NC, December, 2002.

Jeuken, A., J. P. Veefkind, F. Dentener, S. Metzger and C. R. Gonzalez, Simulation of the aerosol optical depth over Europe for August 1997 and a comparison with observations, *J. Geophys. Res.*, *106(D22)*, 28295-28312, doi:10.1029/2001JD900063, 2001.

Kames, J. and U. Schurath, Alkyl nitrates and bifunctional nitrates of atmospheric interest: Henry's law constants and their temperature dependencies, *J. Atmos. Chem.*, *15*, 79-95, 1992.

Krol, M.C. and M. van Weele - Implications of variations in photodissociation rates for global tropospheric chemistry, *Atmos. Environ., 31,* 1257-1273, 1997.

von Kuhlmann, R., Tropospheric Photochemistry of Ozone, its precursors and the Hydroxyl radical: A 3D-modeling study considering non-methane hydrocarbons, Thesis, Mainz, http://www.mpch-mainz.mpg.de/~kuhlmann/rvkdiss.pdf, 2001.

von Kuhlmann, R., M. G. Lawrence, U Poschl and P. J. Crutzen, Sensitivities in global scale modeling of isoprene, *Atmos. Chem. Phys.*, *4*, 1-17, 2004.

Koch, S. and G.K. Moortgat, Photochemistry of methylglyoxal, *J. Phys. Chem.,* 102, 9142-9153, 1998.

Koelemeijer, R.B.A., J. F. de Haan and P. Stammes, A database of spectral surface reflectivity in the range 335-722nm derived from 5.5 years of GOME observations, *J. Geophys. Res.*, *108(D2)*, doi:10.1029/2002JD002429, 2003.

Krol, M., S. Houweling, B. Bregman, M. van den Broek, A. Segers, P. van Velthoven, W. Peters, F. Dentener, and P. Bergamaschi, The two-way nested global chemistry-transport zoom model TM5: algorithm and applications, *Atmos. Chem. Phys.*, *5*, 417-432, 2005.

Landgraf, J., and P. J. Crutzen, An efficient method for online calculations of photolysis and heating rates, *J. Atmos. Sci.*, *55*, 863-878, 1998.

Liang, J and M. Z. Jacobson, Comparison of a 4000-reaction chemical mechanism with the carbon bond IV and an adjusted cabon bond IV-EX mechanism using SMVGEAR II, *Atmos. Environ.*, *34*, 3015-3026, 2000.

Lind, J. A. and G. L. Kok, Henry's law determinations for aqueous solutions of hydrogen peroxide, methylhydroperoxide, and peroxyacetic acid, *J. Geophys. Res.*, *91D*, 7889-7895, 1986.

Logan, J., An analysis of ozonesonde data for the troposphere: Recommendations for testing 3-D models and development of a gridded climatology for tropospheric ozone, *J. Geophys. Res.*,*104(D13)*, 16115-16149, 1999.

Madronich, S., Implications of recent total atmospheric ozone measurements for biologically active ultraviolet radiation reaching the Earth's surface, *Geophys. Res. Lett.*, *19*, 37-40, 1992.

Marenco, A., V. Thouret, P. Nédélec, H. Smit, M. Helten, D. Kley, F. Karcher, P. Simon, K. Law, J. Pyle, G. Poschmann, R von Wrede, C Hume and T. Cook, Measurement of ozone and water vapor by Airbus in-service aircraft: The MOZAIC airborne program, An Overview, *J. Geophys. Res.*,*103(D19)*, 25631-25642, 1998.

Matsumi, Y., F. J. Comes, G. Hancock, A. Hofzumahus, A. J. Hynes, M. Kawasaki and A. R. Ravishankara, Quantum yields for the production of $O(^1D)$ in the ultraviolet photolysis of ozone: recommendation based on evaluation of laboratory data, *J. Geophys. Res.*, *107(D3)*, 4024, doi:10.1029/2001JD000510, 2002.

Olivier, J.G., J. A. F. Bouwman, C. W. M. Van der Maas, J. J. M. Berdowski, C. Veldt, J. P. J. Bloss, J. H. Visschedijk, P. Y. J. Sandveld and J. L. Haverlag, Description of EDGAR 2.0, *RIVM Rep. 771060002*, Rijksinstituut voor Volksgezondheid en Milieu, Bilthoven, 1996.

O'Sullivan, D. W., M. Lee, B. C. Noone, and B. G. Heikes, Henry's law constant determinations for hydrogen peroxide, methyl hydroperoxide, hydroxymethyl hydroperoxide, ethyl hydroperoxide, and peroxyacetic acid, *J. Phys. Chem.,, 100*, 3241-3247, 1996.

Peng, Y. P., K. S. Chen, C. H. Lai, P. J. Lu and J. H. Kao, Concentration of H_2O_2 and HNO_3 and O3-VOC-NOx sensitivity in ambient air in Southern Taiwan, *Atmos. Environ.*, *35*, 6741-6751, 2006.

Pöschl, U., R. von Kuhlmann, N. Poisson and P. J. Crutzen, Development and Intercomparison of Condensed Isoprene Oxidation Mechanisms for Global Atmopsheric Modelling, *J. Atms. Chem.*, *37*, 29-52, 2000.

Prather, M.J. and D.Ehhalt, Atmospheric chemistry and greenhouse gases, in: *Climate Change 2001: The Scientific Basis, Contribution of Working Group I to the Third Assessment Report of the Intergovernmental Panel on Climate Change,* edited by J. T. Houghton et al., 239-288, Cambridge Univ. Press, New York, 2001.

Roberts. J.M. and R.W.Fayer, UV absorption cross section of organic nitrates of potential atmospheric importance and estimation of atmospheric lifetimes, *Environ. Sci. Technol.*, *23*, 945-951, 1989.

Sander, S. P., R. R. Friedl, W. B. DeMore, A. R. Ravishankara, D. M. Golden, C. E. Kolb, M. J. Kurylo, R. F. Hampson, R. E. Huie, M.J.Molina and G.K.Moortgart, Chemical Kinetics and Photochemical Data for Use in Atmospheric studies, Evaluation No.13, JPL Publication 00-3, 2000.

Sander, S. P., R. R. Friedl, A. R. Ravishankara, D. M. Golden, C. E. Kolb, M. J. Kurylo, R. E. Huie, V. L. Orkin, M. J. Molina, G. K. Moortgart and B. J. Finlayson-Pitts, Chemical Kinetics and Photochemical Data for Use in Atmospheric studies, Evaluation No.14, JPL Publication 02-25, 2002.

Sander, S. P., R. R. Friedl, A. R. Ravishankara, D. M. Golden, C. E. Kolb, M. J. Kurylo, M. J. Molina, G. K. Moortgart, H. Keller-Rudek, B. J. Finlayson-Pitts, P. H. Wine, R. E. Huie, and V. L. Orkin, Chemical Kinetics and Photochemical Data for Use in Atmospheric studies, Evaluation No.15, JPL Publication 06-2, 2006.

Sauvage, B., V. Thouret, J-P. Cammas, F. Gheusi, G. Athier and P. Nédélec, Tropospheric ozone over Equatorial Africa: regional aspects from the MOZAIC data, *Atms. Chem. Phys.*, 5, 311-335, 2005.

Schwartz, S. E. and W. H. White, Solubility equilibria of the nitrogen oxides and oxyacids in dilute aqueous solution, In J. R. Pfafflin and E. N. Ziegler, editors, Advances in Environmental Science and Engineering, volume 4, pages 1-45, Gordon and Breach Science Publishers, NY, 1981.

Shetter, R. E., C. A. Cantrell, K. O. Lantz, S. J. Flocke, J. J. Orlando, G. S. Tyndall, T. M. Gilpin, C. A. Fischer, S. Madronich, J. G. Calvert, W. Junkermann, Actinometric and radiometric measurement and modeling of the photolysis

rate coefficient of ozone to O(^{1}D) during Mauna Loa Observatory Photochemistry Experiment 2, *J. Geophys. Res.*, *101(D9)*, 14631-14642, doi: 10.1029/96JD00211, 1996.

Shettle, E. P. and R. W. Fenn, Models for the aerosols of the lower atmosphere and the effects of the humidity variations on their optical properties, Environ.Res.Paper, 676, AFGL-TR-79-0114, 91pp, 1979.

Shindell, D. T., G. Faluvegi, D. S. Stevenson, M. C. Krol, L. K. Emmons, J-F. Lamarque, G. Petron, F. J. Dentener, K. Ellingson, M. G. Schultz, O. Wild, M. Amman, C. S. Atherton, D. J. Bergmann, I. Bey, T. Butler, J. Cofala, W. J. Collins, R. G. Derwent, R. M. Doherty, J. Drevet, H. J. Eskes, A. M. Fiore, M. Gauss, D. A. Hauglustaine, L. W. Horowitz, I. S. A. Isaksen, M. G. Lawrence, V. Montanaro, J.-F. Muller, G. Pitari, M. J. Prather, J. A. Pyle, S. Rast, J. M. Rodriguez, M. G. Sanderson, N. H. Savage, S. E. Strahan, K. Sudo, S. Szopa, N. Unger, T. P. C. van Noije and G. Zeng, Multimodel simulations of carbon monoxide: Comparison with observations and projected near-future changes, *J.Geophys.Res.*, *111*, doi: 10.1029/2006JD007100, 2006.

Staudinger, J. and P. V. Roberts, A critical review of Henry's law constants for environmental applications, *Crit. Rev. Environ. Sci. Technol., 26*, 205-297, 1996

Stevenson, D.S., F. J. Dentener, M. G. Schultz, K. Ellingsen, T. P. C. van Noije, O. Wild, G. Zeng, M. Amann, C. S. Atherton, N. Bell, D. J. Bergmann, I. Bey, T. Butler, J. Cofala, W. J. Collins, R. G. Derwent, R. M. Doherty, J. Drevet, H. J. Eskes, A. M. Fiore, M. Gauss, D. A. Hauglustaine, L. W. Horowitz, I. S. A. Isaksen, M. C. Krol, J.-F. Lamarque, M. G. Lawrence, V. Montanaro, J.-F. Müller, G. Pitari, M. J. Prather, J. A. Pyle, S. Rast, J. M. Rodriguez, M. G. Sanderson, N. H. Savage, D. T. Shindell, S. E. Strahan, K. Sudo and S. Szopa, Multimodel ensemble simulations of present-day and near-future tropospheric ozone, *J.Geophys.Res.*, *111*, D08301, doi:10.1029/2005JD006338, 2006

Stockwell, W.R., F. Kircher, M. Kuhn and S. Seefeld, A new mechanism for regional atmospheric chemistry modelling, *J.Geophys.Res.*, *102(D22)*, doi: 10.1029/97JD00849, 25847-25880, 1997.

Tan, D., I. Faloona, J. B. Simpas, W. Brune, J. Olson, J. Crawford, M. Avery, G. Sachse, S. Vay, S. Sandholm, H-W Guan, T. Vaughn, J. Mastromarino, B. Heikes, J. Snow, J. Podolske and H. Singh, OH and HO2 in the tropical Pacific: Results from the PEM-Tropics B, *J.Geophys.Res., 106,* 32667-32681, 2001.

Tanaka, P.L., D. T. Allen, E. C. McDonald-Buller, S. Chang, Y. Kimura, C. B. Mullins, G. Yarwood and J. D. Neece, Development of a chlorine mechanism for use in the carbon bond IV chemistry model, *J.Geophys.Res.*, *108(D4)*, doi:10.1029/2002JD002432, 2003.

van der A., R. J., D. H. M. U. Peters, H. Eskes, K. F. Boersma, M. Van Roozendael, I. De Smedt and H. M. Kelder, Detection of the trend and seasonal variation in tropospheric NO_2 over China, *J.Geophys.Res.*, *111*, doi:10.1029/2005JD006594, 2006.

van der A., R. J., H. J. Eskes, K. F. Boersma, T. P. C. van Noije, M. van Roozendael, I de Smedt, D. H. M. U. Peters, and E. W. Meijer, Trends, Seasonal Variability and dominant NO_x source derived from a ten year record of NO_2 measured from space, *J.Geophys.Res.*, in press., 2008.

van Noije, T. P. C., H. J. Eskes, F. J. Dentener, D. S. Stevenson, K. Ellingsen, M. G. Schultz, O. Wild, M. Amann, C. S. Atherton, D. J. Bergmann, I. Bey, K. F. Boersma, T. Butler, J. Cofala, J. Drevet, A. M. Fiore, M. Gauss, D. A. Hauglustaine, L. W. Horowitz, I. S. A. Isaksen, M. C. Krol, J.-F. Lamarque, M. G. Lawrence, R. V. Martin, V. Montanaro, J.-F. Müller, G. Pitari, M. J. Prather, J. A. Pyle, A. Richter, J. M. Rodriguez, N. H. Savage, S. E. Strahan, K. Sudo, S. Szopa and M. van Roozendael, Multi-model ensemble simulations of tropospheric NO_2 compared with GOME retrievals for the year 2000, *Atmos. Chem. Phys.*, *6*, 2943-2979, 2006.

Van der Werf, G. R., J. T. Randerson, G. J. Collatz and L. Giglo, Carbon emissions from fires in tropical and subtropical eco-systems, *Global Change. Biol. 9*, 547-562, 2003.

Wild O, Modelling the global tropospheric ozone budget: exploring the variability in current models, *Atmos.Chem.Phys.*, *7*, 2643-2660, 2007.

Wille, U., E. Becker, R. N. Schindler, I. T. Lancer, G. Poulet and G. LeBras, A discharge flow mass-spectrometric study of the reaction between NO_3 radical and isoprene, *J. Atmos. Chem.*, *13*, 183-193, 1991.

Williams, J.E., J. Landgraf, A. Bregman and H. H. Walter, A modified band approach for the accurate calculation of online photolysis rates in stratospheric and tropospheric Chemistry Transport Models, *Atmos. Chem. Phys.*, *6*, 4137-4161, 2006.

Yarwood, G., G. Z. Whitten and S. Rao, Updates to the Carbon Bond 4 photochemical mechanism, Environ.Int.Corp., Final Report, www.ladco.org/reports/rpo/MWRPOprojects/Modeling/CAMx_CB4_Update_Final_3-05.pdf, 2005a.

Yarwood, G., S. Rao, M. Yocke and G.Z.Whitten, Updates to the Carbon Bond Mechanism: CB05, Yocke and company, Final Report, RT-04-00675, http://www.camx.com/publ/, 2005b.